LABORATOIRE NATIONAL DES CHAMPS MAGNETIQUES INTENSES

ANNUAL REPORT

2023

Laboratoire National des Champs Magnétiques Intenses

Grenoble–Toulouse

Centre National de la Recherche Scientifique

http://lncmi.cnrs.fr/

Annual Report

2023

LNCMI is formally associated with the "Université Grenoble Alpes", the "Université Paul Sabatier", Toulouse and the "Institut National des Sciences Appliquées", Toulouse.

Typeset using LaTeX Editor: Duncan K. Maude

Preface

Dear Reader,

Please find here the 2023 annual report of the Laboratoire National des Champs Magnétiques Intenses (LNCMI). This report provides a quite complete overview of the in-house and collaborative science as well as our technical activities. Magnetic fields for practical applications are usually provided by permanent magnets (up to 1 T) or superconducting coils (up to 28 T in 2023). To create magnetic fields greater than these values, very specific devices are needed, they are quite expensive (many M€) and the market for such devices is rather limited. For these reasons, high magnetic field laboratories are the only ones able to deliver such magnetic fields above 28 T. In addition, measurements under such magnetic fields have to be designed specifically, so that the instrumentation used in these laboratories has to be designed in-house (thermometry, electronics, every sensor has to be specifically designed to work under high magnetic fields). The regular increase in the size of the devices to create such magnetic fields makes that today, only few places in the world are operating such facilities (Europe, USA, China, Japan). The "Laboratoire National des Champs Magnétiques Intenses" is one of them.

Contrary to other techniques, in which you typically have gains of orders of magnitude over a few years, to increase the magnetic field is a very complex challenge, and the progress is rather slow. It is only very recently that superconductive magnets reached 28 T, after a long plateau at 20 T during many years. The required funding to increase resistive magnetic fields or pulsed fields are quite huge (typically $\simeq 50$ M€) so the life time of the power supply should be 20 to 30 years to have a reasonable return on investment. In addition, the resistive coils themselves are used very close to their limit, with a lifetime of a few hundreds of hours (or a few hundreds of pulses), so they have to be replaced regularly.

Despite these difficulties, the use of the highest magnetic fields available is of great interest for the societal impact of the related research. The main application of high magnetic fields ("high field science") is the development of a plethora of spectroscopic techniques to better understand new materials. The development of new materials is a fundamental need for new applications. This is true to improve the circular economy, to improve the energetic efficiency of any process, to find new drugs, to find new quantum materials for quantum computing. The discovery of new materials (or of new properties of existing materials) is the basis for any improvement of a material use. Many of these "spectroscopies" are based on application of a magnetic field to the material, and have a better resolution when you increase the magnetic field. This is the case of nuclear magnetic resonance (NMR), and also many other techniques such as "optical" spectroscopy (Raman, UV, IR, THz, EPR, *etc*), resistive or magnetic spectroscopy (quantum oscillations), thermal spectroscopy (specific heat, thermal conductivity), ultrasonic spectroscopy. The development of all these techniques in magnetic field is of prime interest for the development of new materials. High magnetic field science is basic research which should exist before any other new development. For this reason, it should not be forgotten in any research plan for the future developments of materials.

In addition to these "spectroscopies", the role of a high magnetic field laboratory is also to find new states of matter in high magnetic fields (one of the best examples of a new state is the quantum hall effect) or to find new fundamental physics (examples are vacuum birefringence or new particles in dark matter). It should also be kept in mind that high magnetic field is also large volumes (in these cases, the unit is Tm^3 , $2.5\,\mathrm{Tm}^3$ being an energy of 1 MJ). As examples, 40 T in $(50 \times 50 \times 50)\,\mathrm{mm}^3$ is $0.4\,\mathrm{Tm}^3$, and 10 T in $(300 \times 300 \times 300)\,\mathrm{mm}^3$ is $0.27\,\mathrm{Tm}^3$.

LNCMI generates high magnetic fields, above what is available in regular laboratories, for academic and industrial users from France, Europe and other countries around the world. In Grenoble, on a regular basis, we provide DC magnetic fields up to 36 T using resistive magnets. In Toulouse, we provide up to 90 T with pulsed fields of about 100 ms duration. LNCMI, as all the large infrastructures in Europe, is facing many challenges, and in particular the climatic crisis and the energy crisis. Our investments over the last years in new materials, and in new techniques, places us in a very good position to provide world class magnetic fields, as you will read in the present report. We are confident that LNCMI will continue to play an important role in science in the coming years.

Charles Simon
January 2024

CONTENTS

LIST OF FIGURES

The LNCMI user facility

INTRODUCTION

The Laboratoire National des Champs Magnétiques Intenses (LNCMI) is one of the large scale facilities of the CNRS. It works as a research facility available both to its own researchers, as well as to external users. The high field facility is open to users from all over the world.

The LNCMI is also a member of the European Magnetic Field Laboratory (EMFL). EMFL is a legal entity (Association Internationale Sans But Lucratif, AISBL) in Brussels, Belgium, that provides the highest possible fields (both continuous and pulsed) for researchers. EMFL was founded in order to unite, coordinate and reinforce the three existing medium scale European high magnetic field laboratories - the Dresden High Magnetic Field Laboratory (Germany), the Laboratoires National des Champs Magnétiques Intenses in Grenoble and Toulouse (France), and the High Magnetic Field Laboratory in Nijmegen (The Netherlands) - within a single body in order to provide such an infrastructure. The British and Polish high magnetic field communities have also joined EMFL, as well as Italy since November 2023. The EMFL organization is the single entry point for users to obtain access to all European pulsed and DC field facilities. The access to superconducting magnets is treated separately by each facility.

HIGH MAGNETIC FIELDS AND INSTRUMENTATION AVAILABLE TO THE USERS

The LNCMI has resistive magnets at the Grenoble site, pulsed magnets at the Toulouse site, as well as several superconducting magnets at both sites, achieving continuous magnetic fields up to 36 T and pulsed fields up to 90 T in which it is possible to install various experimental set-ups. The Toulouse site also operates a Megagauss facility producing pulsed fields up to 180 T in a semi-destructive magnet. Mobile generators and coils, designed for use in combination with other very large scale facilities, produce high fields for users of synchrotron, neutrons sources and intense lasers.

The technical and experimental environment also allows the user to combine very low temperatures and high pressures with very high fields. The laboratory offers a wide variety of instrumentation, allowing measurements in high magnetic fields in the following techniques:

- **Optical spectroscopy and magneto-optics-** optical microscope imaging, birefringence, dichronism and Faraday rotation, (micro-)photoluminescence spectroscopy, (micro-)Raman scattering, (far-)infrared spectroscopy.
- **Thermodynamic properties-** specific heat, thermopower and Nernst-Ettinghausen, DC/AC susceptibility, compensated-coil magnetometry, torque magnetometry, ultrasonic measurements (sound velocity and attenuation).
- **Magnetotransport-** magnetotransport with in-situ sample rotation, critical current of superconductors (wires, tapes and coils),contactless transport (TDO, PDO).
- **Magnetic resonance-** electron spin resonance, nuclear magnetic resonance.
- **Advanced sources-** X-Ray spectroscopies.
- **Environments-** ^{4}He cryostats (1.5-300 K,) ^{3}He cryostats (down to 300 mK), dilution refrigerators (down to 30-100 mK), thermostats up to 300 °C, high pressure.
- **Other-** Megagauss facility (semi-destructive fields $>$ 170 T), Mobile 1 MJ installation allowing X-rays, laser and neutron scattering under pulsed magnetic fields, levitation, thermometry.

ACCESS TO THE FACILITIES

Scientists who wish to obtain access to the resistive or pulsed magnets of the LNCMI must apply through the User Portal of the EMFL website (https://emfl.eu/SelCom/login.php). This application is drawn up according to a specific form and provides information demonstrating the relevance of the research work to be undertaken. The application is also used to ensure that the experimental conditions requested can be satisfied. Furthermore, scientists will find a large part dedicated to the user access on the EMFL website that includes relevant details about experimental possibilities with examples, instrumental set-ups and available magnets as well as practical information for users coming to the EMFL laboratories to perform their experiments.

For the use of the LNCMI mobile pulsed field facility, users must apply directly to the relevant very large scale facilities (ESRF, ILL, LULI, NIF).

Access to the superconducting magnets of the LNCMI as well as for technical projects using resistive magnets goes through an in-house procedure, which is open all year (http://lncmi.cnrs.fr/utilisateur/).

In the frame of the EMFL-ISABEL project, novel access procedures in order to satisfy the needs of all current and potential users are developed, implemented and evaluated. These procedures are based on feedback from the user community and on a study of ongoing practices at other research institutions (RIs). They are listed below:

- **Dual access-** introduced in 2021, this procedure allows users to apply, in a single proposal, for access to one of the regional partner facilities of EMFL for preliminary experiments in moderate fields, which if successful are followed by high-field experiments at one of the EMFL high-field facilities. These combined proposals have to be submitted during the regular calls, the EMFL selection committee will judge the pertinence of the low-field experiments and grant conditional access to the EMFL installations.
- **Fast-track access-** introduced in fall 2022, the fast-track access is permanently open for convincingly urgent scientific cases. The request will be evaluated and decided within typically 2 weeks by the EMFL board of directors who may optionally consult one or more EMFL selection committee members, and check the feasibility with the facility manager and the local contact.
- **Longterm access-** introduced in fall 2022, this mode aims to meet the demand for long-term access schemes such as complex high-level science cases which require a sequel of high-field experiments. Long-term access proposals must be submitted during the regular call periods and will be evaluated by the EMFL board of directors as a special category. If positively evaluated, the user will obtain an extended amount of access over a two to three-year period.
- **Technical development access-** introduced in fall 2022, this method is dedicated to the interest of scientists wishing to develop and improve technical installations and metrological procedures that could also be of great interest to other EMFL users. These developments aim at improving the quality of EMFL installations with clear benefit to the wide EMFL user community. Technical proposals must be submitted during the regular call periods and will be evaluated by the EMFL board of directors as a special category. In convincingly urgent cases they can also be submitted using the fast-track access mode.
- **First-time access-** introduced in spring 2022, this access mode aims to lower the barrier for researchers who want to use the EMFL facilities for the first time. EMFL will offer reinforced support in preparing a proposal as well as reinforced on-site support. The first-time access can be combined with regular access proposals or any other access mode listed above.
- **Industrial access-** To meet the needs of industry, EMFL makes its infrastructures available to industrial users. The request can be addressed anytime via a dedicated form on the industry section of the EMFL website.

SUBMITTED PROPOSALS

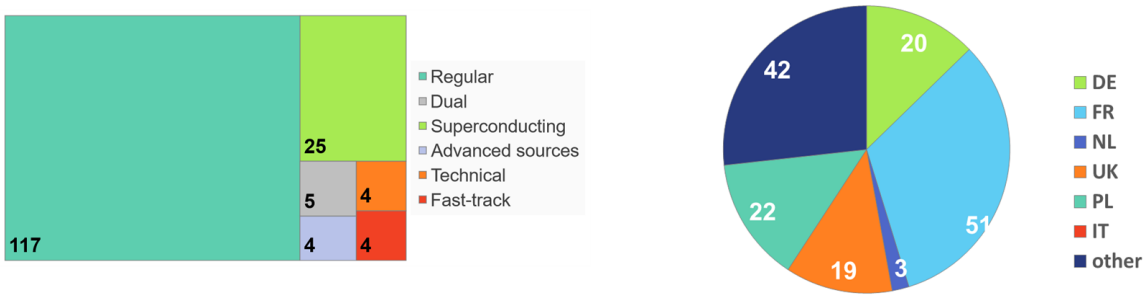

FIG. 1. *(left) Submitted proposals by proposal type and (right) by affiliation country of PI distinguishing EMFL member countries, EMFL partners and other.*

A total of 159 proposals have been submitted in 2023. Figure 1 shows on the left the distribution by proposal type (regular and novel access mode proposals submitted to EMFL, proposals using advanced sources submitted to the very large scale facilities, proposals for superconducting magnets going through the in-house procedure). The right part of figure 1 represents the affiliation country of the principal investigator (PI) by EMFL member countries, EMFL partners and other countries.

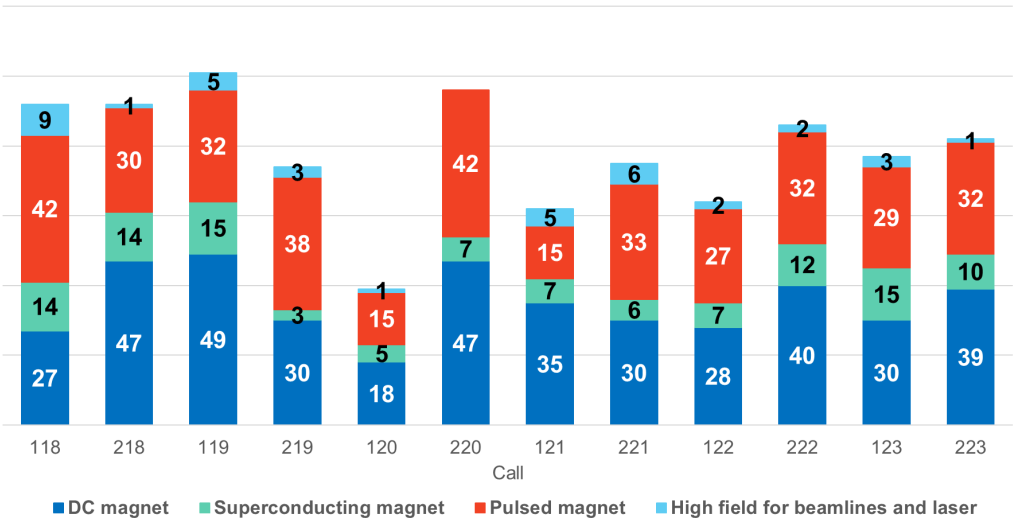

FIG. 2. *Number of projects submitted; the projects on DC magnets use the Grenoble facility, on pulsed magnets the Toulouse facility, the mobile capacitor bank is used in combination with beam-lines or lasers, those on superconducting magnets refer only to the external users at the Grenoble facility.*

In the period 2018 – 2023, 940 projects have been submitted to the LNCMI, of which 420 proposals were requests for the different configurations of DC resistive magnets at the Grenoble facility, 367 demands for pulsed magnets at the Toulouse facility, 38 for using the mobile capacitor bank in combination with beam-lines at other research institutions and 115 external projects submitted for superconducting magnets (see figure 2). The in-house projects performed on superconducting magnets are not considered here. The particular success of the possibility of working in different bore diameters of the 24 MW DC magnets with fields of 36 T in a 34 mm bore, 31 T in a 50 mm bore and 20 T in a 170 mm bore must be underlined.

Furthermore, some users are particularly interested in large bore diameters such as 130 mm or 376 mm that use 12 MW which is half of the actual power available. These configurations are needed for the development of applied superconductivity, magneto-electrochemistry and magneto-hydrodynamics. The 12 MW magnets can also be used with the standard bore diameters of 34 and 50 mm achieving fields up to 25 T which can be of considerable interest for the preparation of very high field experiments or the development and testing of new experimental set-ups. This allows the LNCMI to offer access for very different types of experiments.

As a consequence of the Covid-19 crisis, with the lockdown and the travel restrictions, the number of submitted proposals at the first call of 2020 in spring (call 120) was very low. It had also been decided to extend the validity of proposals of the previous calls beyond one year. Since autumn 2020 (call 220), the numbers returned to more usual levels. The laboratory does its best to offer magnet time to all users who had their proposals accepted by the selection committee. Nevertheless, the requested access is generally higher than the possibilities the laboratory can offer. Consequently, when submitting, the proposal quality is crucial.

PROPOSAL EVALUATION

The EMFL applications are examined and ranked by the EMFL selection committee, or EMFL board of directors as described above. The evaluation of the proposals is carried out twice a year, in the course of December and at the end of June; fast-track proposals are evaluated at any time. The applications are ranked A, B or C. Projects rated A will be executed, those classified B are performed if the magnet time is available, and applications rated C are rejected. The ranking is made on the same basis for all applications, including those submitted by local scientists. The proposals for using the mobile pulsed field capacitor bank are evaluated directly by the relevant very large scale facility, the projects are rated A (accepted) or C (rejected). Figure 3 shows the high quality of the submitted proposals for the LNCMI sites for 2023, with 33% of the proposals rated A or A-, 39% rated B+, 25% rated B or B- and only 3% rated C.

Accepted experiments are subsequently programmed during the two semesters following the ranking of the selection committee. If the experiment has not been performed in this period, the principle investigator is required to resubmit the proposal mentioning the reasons why it could not be performed (issue with sample preparation, high pressure on the magnet time schedule, *etc*). The acceptance of an application means that for non-industrial users the entire cost of the experiment (scientific and technical support, electricity, cryogenic fluids, *etc*) will be covered by the budget of the laboratory, for industrial users a financial basis for the performance of the proposal will be defined.

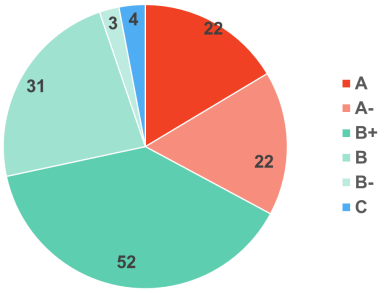

FIG. 3. *Evaluation of proposals submitted in 2023 (EMFL calls 123 and 223).*

The selection committee is divided into five groups, each with a different area of expertise (semiconductors, metals and superconductors, magnetism, applied superconductors, soft materials). In each area there are international experts from outside the EMFL consortium, as well as scientists from the different high magnetic field laboratories of the EMFL consortium, whose presence ensures that a project can technically be performed in the laboratory.

PERFORMING AN EXPERIMENT

Local contact

When the applicant is informed of the acceptance of his/her proposal, and of the number of pulses/shifts scheduled for the experiment, he/she is at the same time informed of the name of the local contact in charge of facilitating their work at the LNCMI. The local contact is a research scientist or an engineer of the laboratory. If an applicant has not identified a local contact, the laboratory management will appoint a scientist that the user can contact in order to define with him/her the conditions for the organization of the experimental work. The instrumentation groups of both sites of the LNCMI assure the technical support for the experiments.

Operation and magnet time

The periods of operation of the DC field facility, maintenance, work for upgrading and shut-down are fixed one year in advance. In general, the facility is stopped twice a year for maintenance with an additional short break of one week in spring. Further stops of the power installation can be decided for work, upgrading or commissioning a new magnet.

The pulsed field facility is accessible the whole year except for the annual shutdowns, generally the first two weeks in August and one week for Christmas. The 14 MJ, 3 MJ and 1 MJ generators are available to users for long pulse experiments. The 90 T multi-stage coils are fully available to users. The megagauss facility is open to users for optical spectroscopy and magnetization experiments up to 150 T at $T = 10$ K.

The magnet time schedule is drawn up for one semester and regularly updated. The demand for the facilities being high, visitors are strongly urged to get in touch with their local contact at the beginning of each semester, in January and in July, to discuss the scheduling of their experiment. LNCMI will do its maximum to satisfy the requests of its users and find the most suitable period for carrying out the experiments. The user support on the magnet sites is assured by the scientific local contacts and the instrumentation team.

The magnets operate on a schedule taking into account the availability of staff, magnets and instrumentation. For the DC field facility, the installation is operational up to 24 hours per day 7 days a week including weekends and bank holidays. In 2023, the experiments were mostly scheduled during daytime or evening with two standard shifts from 9 a.m. to 4 p.m. and 4 p.m. to 11 p.m., and a weekly maintenance on Wednesdays from 9 a.m. to 4 p.m. If needed, the daily shift time can be flexible and adapted to the experiment's needs. An LNCMI operator must be contacted during working hours for any operational request whereas outside normal working hours, a safety agent provides a presence in the laboratory.

At the DC field facility twice a month the technical teams (power facility group, magnet group, instrumentation group, operators etc.) and scientists of the currently scheduled projects come together in an interdisciplinary coordination meeting. This allows the exchange of information (planned experiments and special demands, observed incidents, technical improvements, organization issues etc.) and the coordination of technical interventions.

Regarding the superconducting magnets, the schedule is managed by the relevant scientific teams. The magnet time using the mobile capacitor bank in combination with beam-lines or lasers is directly attributed by the relevant very large scale facility.

ADMINISTRATION, FEEDBACK AND REPORTING

Users are invited to fill out and submit an online Admin form on the User Portal as soon as possible after scheduling of the experiment. The Admin form provides the facility with the information necessary to prepare the visit of the experimental team. The main proposer and all participants on the proposal are listed by default on the Admin form. The form can be modified and additional scientists added. Users will also indicate their travel and accommodation information for each participant. By submitting, the Admin form will be sent to the facility's user support who will take care of accomplishing various formalities (declaring a presence to the central administration, authorizations and access to the campus, IT charter and safety formalities, logistics).

After performing the experiment, the user committee would like to receive feedback in order to constantly improve user access at the EMFL facilities. The feedback form can be filled out online. The data is handled confidentially by the User Committee (https://emfl.eu/emfl-user-organisation/).

Within two months following the experiment, users are required to submit a progress report. It can be filled online via the EMFL User Portal (https://emfl.eu/SelCom/login.php). This report is essential and is requested by the Selection Committee. It also is used to justify the use of the facilities.

ELECTRICITY COSTS & ENERGY MANAGEMENT AT THE DC FIELD FACILITY

Electricity costs

Since more than 10 years the laboratory has to deal with steeply increasing electricity prices. From 2016 to 2019 the DC field facility bought its own electricity on the open market. Since 2020, the costs for electricity are negotiated at the national level to have a more stable price over one or two years but with the drawback that the high degree of flexibility in power consumption and consequently a more interesting contract could not be taken into account. With the recent energy crisis, the electricity prize in 2023 has rocketed as shown in figure 4.

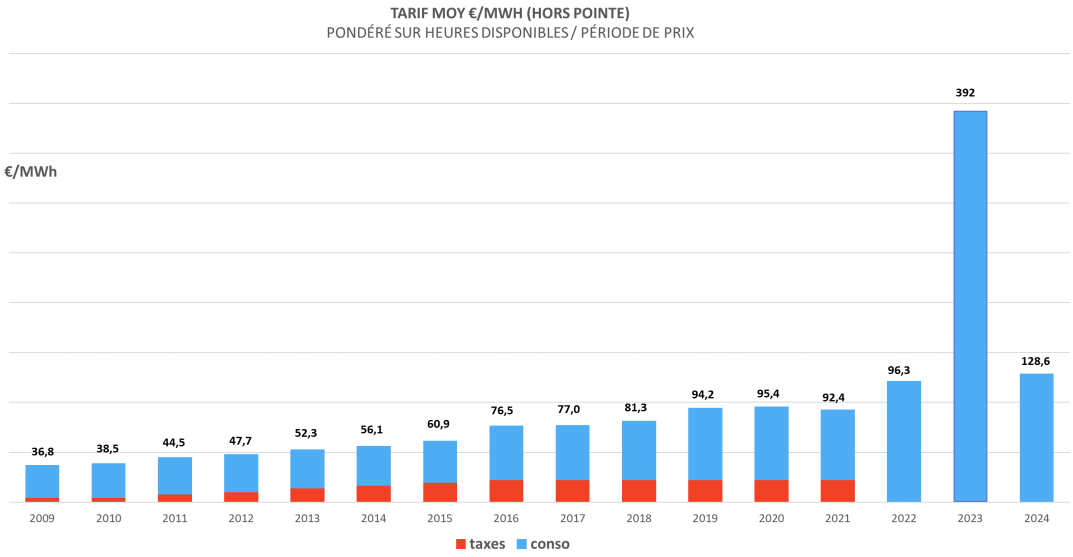

FIG. 4. *Evolution of average electricity price.*

Energy management

The DC field facility has set up different ways to optimize the relation of the number of scientific projects that can be performed with a more and more tight energy budget.

Firstly, users are invited to estimate the required field profile in advance with the help of the local contact and the user access manager. A special tool has been developed and can be made available to simulate the field profile and calculate the corresponding power consumption. An electricity consumption is then allocated to each project. Furthermore, a thorough and detailed preparation of each experiment is essential in order to use the available magnet time efficiently.

Secondly, a new magnet operation mode has been developed and is in use since September 2021. It allows to reduce the mean power consumption by 10 to 15%, taking advantages of the new materials available for magnets and of advanced piloting of the facility. The annual energy saved is $\simeq 1.3\,\mathrm{GWh}$. The gain for a given experiment depends of course strongly on its field profile.

PROJECTS CARRIED OUT IN 2023

The statistics presented here summarize the use of the LNCMI facilities in 2023.

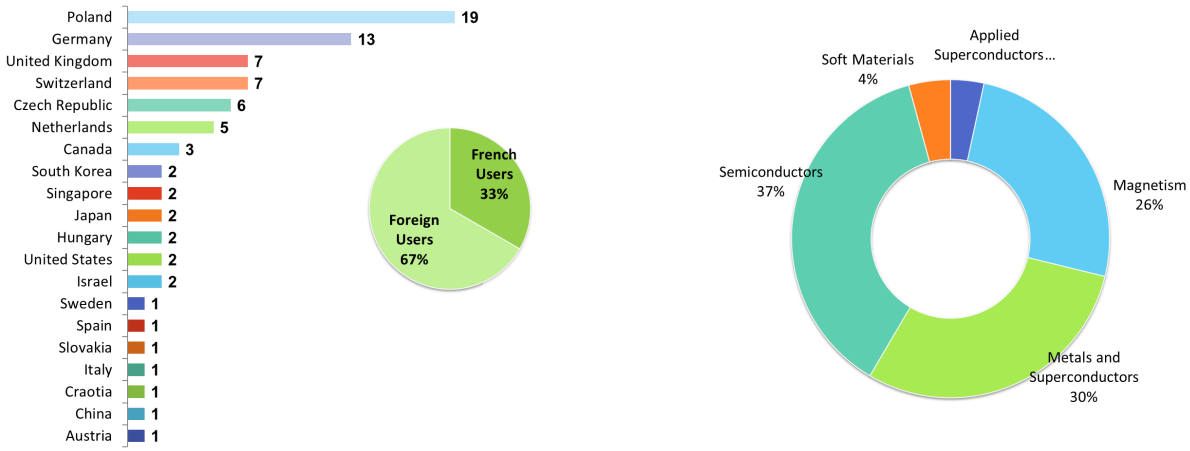

FIG. 5. *Performed proposals in* 2023 *by country of origin (left) and by research area (right).*

The left panel of figure 5 shows the country of origin of the projects that were performed on all magnets, the resistive, pulsed and superconducting magnets. Most of the projects were performed by scientists outside France. The users came mostly from Poland, Germany, and the United Kingdom who are members or partners of EMFL, but also from Switzerland and followed by users from the Czech Republic and the Netherlands.

Generally, most scientists who have already used our facilities come back regularly, introducing and progressively forming scientists who become themselves, in turn, new users. Nevertheless, every year the laboratory also welcomes completely new users. The projects realized at the LNCMI facilities are thematically distributed as shown in the right panel of figure 5 with focus on projects in the semiconductors, the metals and superconductors and the magnetism areas.

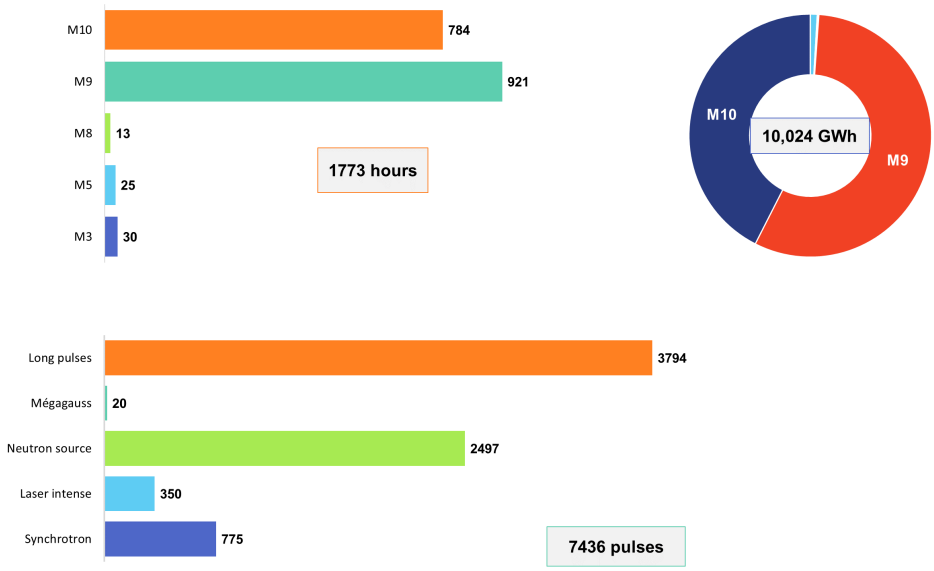

FIG. 6. *Distribution of the number of magnetic field shots at pulsed facility and magnet hours and power used at the DC field facility in* 2023.

The top panel of figure 6 shows the magnet time and power used at the DC field facility. In total, the facility has provided 1773 hours of magnet time, mostly used on the 24 MW magnet sites (left) with a total power consumption of 10.024 GWh (right). The facility was available for science from February to July, and mid-September to October. It was then disconnected from the power grid in order to install a new high-voltage electrical transformer.

The bottom panel of figure 6 shows the distribution of the number of shots, depending on the power supply used, performed at the Toulouse pulsed field facility or using the mobile capacitor bank in combination with

the neutron source at the ILL, intense laser sources at LULI and Rutherford-Appleton Laboratory or the X-ray source at ESRF. The long pulse field facility in Toulouse has provided 3814 shots at high field on a total of 7436 shots and 3622 shots using the mobile capacitor bank in combination with neutrons or intense laser sources.

CONCLUSION

The technical and scientific environment of LNCMI, adapted to research in high magnetic fields, is highly appreciated by the international scientific community. A large majority of users shows great interest in the laboratory and they come regularly in order to perform their experiments, thereby strengthening collaborations between research groups. The number of projects submitted and performed at the LNCMI demonstrates the international scope of the laboratory. As the schedule of the Grenoble 24 MW magnets is extremely tight and the electricity costs high, it is essential to optimize the use of these magnets. Experiments may also be transferred from one facility to the other, after discussion with the scientists, if the schedule is too tight, or in case the another facility has a better adapted set-up for an experiment.

C. Warth-Martin, N. Bruyant, M. Druart, A. Gasparini, S. Buisson, C. Grandclément

Outreach activities

LNCMI-Grenoble: One off interventions

We organized about 20 group visits during the year 2023. We focus on some of them:

- In March a group of Lycéens of the Reunion Island who organized a trip to selected scientific sites in France was welcomed. The exchanges with this very motivated group was highly stimulative.
- In June, visits were organized in the frame of 3 different workshops: Thematic School on Magnetometry, Magnetism and Chirality, General meeting of the European project on energy flexibility in buildings, reaching families of scientists not so familiar with the opportunities offered by high field facilities.
- From June to December, several visits were organized to more specialized attendees (conference EP2DS/MMSS, Heavy Fermion workshop and applied superconductivity school) permitting to disseminate the recent developments of the LNCMI in term of field production.
- 5th of December we received the participants to the Winter School organized by the Renaissance Fusion company recently installed nearby the LNCMI.

FIG. 7. *Visitors at the LNCMI-G during some of the group visits organized during 2023. Bottom left - souvenir photo of the CNRS guides for "la fete de la science" in October.*

LNCMI-Grenoble: Other events

In June 2023, an LNCMI PhD student participated in a science popularization show hosted by the AurorAlpes association on the topic of superconductivity. The program was live-streamed on the Twitch platform and later made available for replay on YouTube : https://www.youtube.com/watch?v=Z2jkQ2GZ7g8. In June, also, we welcomed a Lycéen's group winner of the "Olympiades de Physique" national annual event. The open day of the "fête de la science" in October was a success with about 700 visitors on the CNRS Campus in which the LNCMI is embedded. 60 visitors took a detailed tour on the DC high magnetic field facility on Saturday. The demand actually exceeded the number of trained guides, demonstrating the interest of the general public in understanding how science is made in large scale facilities.

LNCMI-Toulouse: One off interventions

- Internal seminar on new pedagogical methods to teach quantum mechanics from hands-on experiments.
- Two-day professional training course "music and sound" for secondary school teachers at Maison pour la science, Toulouse (20 people).
- One-day professional training course "light: waves and signals" for secondary school teachers at Maison pour la science, Toulouse (20 people).

- Conference with demos: “Expériences de Lumière”, Hôtel d’Assésat, Toulouse (60 people).
- Students training for the International Physics Olympiades (60 people).
- In collaboration with maths colleagues we have organized visits for middle school classes (“Jeunes Talents Mathématiques”).

We also act as supervisor and scientific referee for:

- Long term study group with high school teachers “physics with a smartphone” within the framework of IRES de Toulouse [33] and 4 published papers in French pedagogical journals and 1 in American Journal of physics.
- French national Olympiades de Physique.

Finally, we also contributed to books for the general public:

- “Étonnante physique” published by CNRS Éditions on the occasion of “année internationale de la physique”,
- “Le petit illustré” co-published by CNRS and La Dépêche du midi.

FIG. 8. *A large number of visitors at LNCMI-T on the occasion of “fête de la science”.*

LNCMI-Toulouse: recurrent and other events

For many years now, the optics, superconductivity and semiconductors-and-nanostructures teams and the whole technical staff feels involved and participate actively in the “fête de la science”. On Friday we hosted two classes from high school. The open day for the general public on Saturday was also a success since we had the visit of nearly 100 people curious about the installations of the laboratory and the 5 stands of demonstrations which we animated.

Special acknowledgement

We all wish a happy retirement to our colleagues Sylvie George and Jean-Pierre Nicolin who have animated demos for many years with great enthusiasm.

E. Beaugnon, F. Debray, A. Demuer, C. Faugeras, O. Jay, S. Krämer, R. Raison, J. Sarrade, G. Seyfarth, B. Vincent, R. Mathevet, D. Vignolles, M. Leroux, J. Béard, N. Bruyant, J. Billette, M. Pierre, M. Barragan, S. Tardieu, L.A. Veyrat De Lachenal.

Emerging Layered Materials

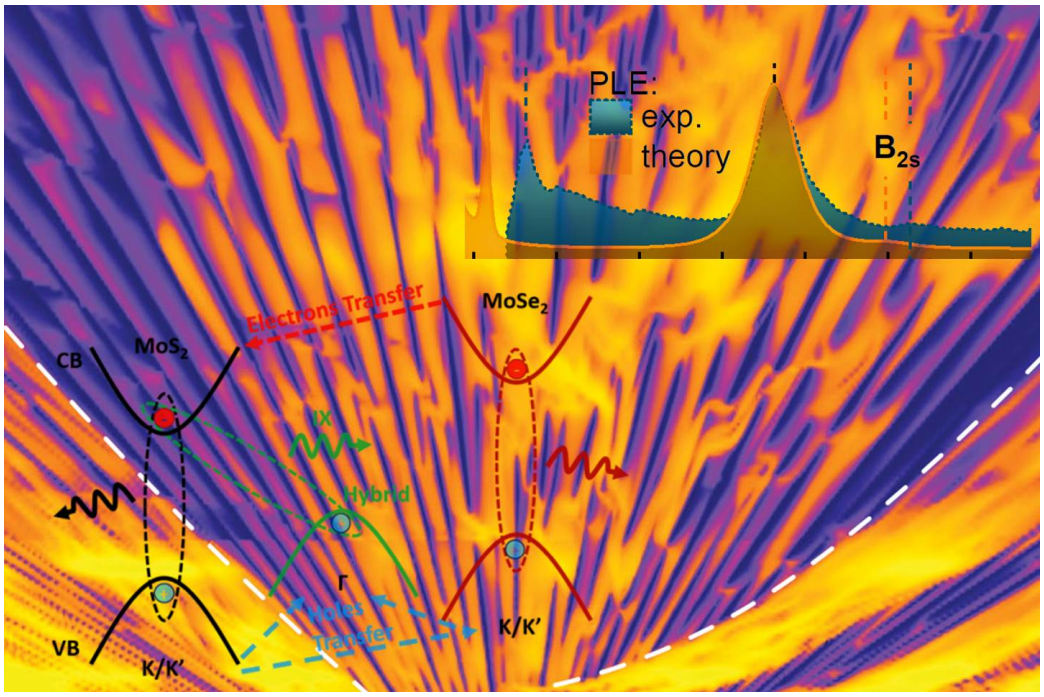

The graphite princess and the moiré pea

Graphite is made of a stacking of layers of carbon atoms arranged in a honeycomb lattice. This recurring pattern gets disrupted at the surfaces of the crystal which leads to the occurrence of "surface states" - fading waves as one delves deeper into the bulk, which have been the subject of several investigations. In this work "twistronic", where one manipulates the properties of -usually 2D- crystals through moiré patterns created by specific relative alignments between them, is taken one step further and applied to the surface of three-dimensional graphite.

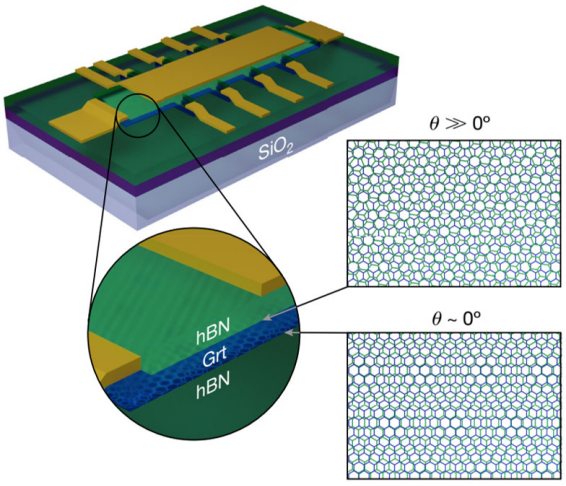

FIG. 9. *(a) Schematic of a heterostructure device with graphite (labelled Grt) encapsulated in hBN with one of the interfaces aligned. Here the lattice mismatch between graphite and hBN has been exaggerated for clarity.*

FIG. 10. *A princess sleeping deep in the bulk of graphite can still feel a pea underneath several layers of graphene. Illustration by Wareki, Leicester, England.*

A schematic of the studied devices, based on bulk Bernal-stacked graphite aligned with hexagonal boron nitride, is displayed in figure 9. Electrical transport was studied under high magnetic fields, enabling us to bring the magnetic length (giving the spatial extent of the electronic wave function) close to the moiré superlattice unit cell, as previously done to evidence the Hofstadter butterfly in graphene. Our findings revealed that the moiré pattern doesn't just alter graphite's surface states: it also has a significant impact on the electronic spectrum of the entire bulk of the graphite crystal. Drawing a parallel with the well-known fairy-tale "The princess and the pea", where the princess felt the pea right through the twenty mattresses and the twenty eider-down beds (see figure 10), the moiré influence extends from the surface all the way through graphite of over 40 atomic layers. As can be seen in figure 11, a unique 2.5-dimensional (2.5D) intertwining of surface and bulk states is observed, and described as a 2.5D Hofstadter butterfly, a fractal version of the 2.5D quantum Hall effect discovered earlier on thin graphite [Yin *et al.*, Nature Physics **15**, 437-442 (2019)].

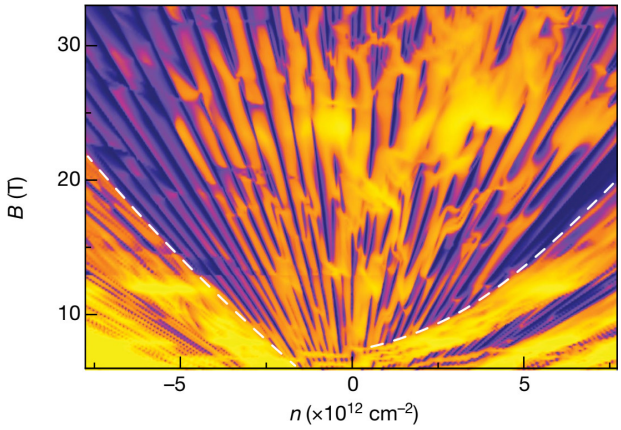

FIG. 11. *(a) 2.5-dimensional Hofstadter's butterfly. Colour map of graphite's conductance (giving an image of the fractal electronic density of states) as a function of the magnetic field and the carrier density. The white dashed curves indicate the transition from surface Landau levels to the bulk quantum regime.*

In the present case, the standing waves in graphite are orchestrated by twistronics, leading to the spiral dance of electrons trapped between the top and bottom surfaces to be directed both by the strong magnetic field and the moiré pattern. The extension of the surface moiré potential deep into graphite's bulk states opens a route to bring new non-trivial physics (spin-orbit coupling, ferromagnetism, and superconductivity) into graphite via proximity effects, and gives new prospects for controlling electronic properties in graphite or other semimetals.

For more details please see [Mullan *et al.*, Nature **620**, 756 (2023)].

B.A. Piot
C. Mullan, S. Slizovskiy, J. Yin, Z. Wang, Q. Yang, S. Xu, Y. Yang, S. Hu, K. S. Novoselov, A. K. Geim, V.I. Falko, A. Mishchenko (Department of Physics and Astronomy and National Graphene Institute, University of Manchester), K. Watanabe, T. Taniguchi (NIMS, Tsukuba)

Plasmon-plasmon interaction in epitaxial graphene microribbons

Plasmons in graphene, the collective excitations in the plasma of Dirac fermions, have attracted considerable interest in past years. The great interest is triggered by the strong enhancement of electromagnetic field, chemical and electrostatic tunability, and low losses, which bring potential applications in detectors, amplifiers, and emitters of terahertz radiation. Since there is a mismatch between photon and plasmon momentum, the light-matter interaction must be introduced by, *e.g.*, translation symmetry breaking. Epitaxial graphene on silicon carbide (SiC) offers a unique opportunity for intrinsic translational symmetry breaking without artificial patterning. However, the origin of such photon-plasmon coupling is not straightforward. Hence, we fabricated three samples with arrays of graphene micro-ribbons. The electron-beam lithography made ribbons provided us with a well-defined geometry. On the other hand, the magneto-plasmon fingerprint is a plasmonic blue shift with an increasing magnetic field. This blue shift is given in graphene only by the carrier density of Dirac fermions.

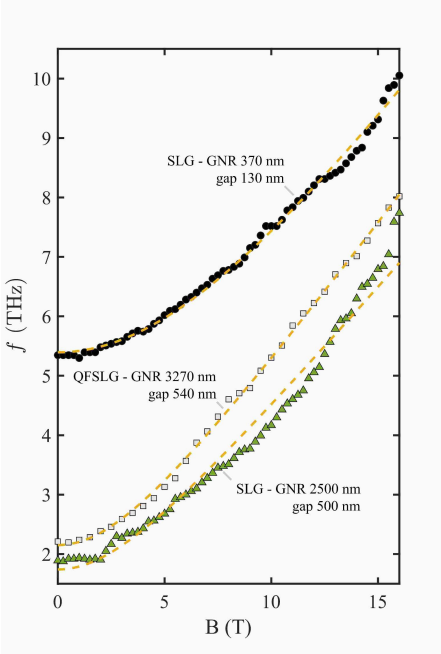

FIG. 12. *The plasmon resonance in the far-infrared spectral range shows the magneto-plasmon behavior in our three graphene samples containing arrays of graphene micro-ribbons. The field dependence is a fingerprint of the magneto-plasmon given by the spatial confinement and charge density in graphene.*

Therefore, measuring the magneto-plasmon in artificially made graphene micro-ribbons (figure 12) also allows us to fix the carrier density in addition to the geometry. These are the only two parameters determining the spectral position of the plasmon resonance.

Surprisingly, we have found that the basic model of the plasmon resonance fails to describe the plasmon resonance at the zero-magnetic field. For this reason, we extended our simulations to the core-shell and equivalent circuit models (figure 13).

Though both models have limitations, there was a significant improvement in describing the experimental data. However, the agreement with these models was not within an experimental error. Hence, we also performed numerical simulations by exactly solving Maxwell equations. The exact solution revealed that there are two more contributions to the spectral position of the plasmon resonance. First, the plasmon-plasmon interaction is the only contribution to the hydrogen intercalated graphene micro-ribbons. Despite the agreement with experimental data, the exact solution of Maxwell equations did not agree with the data in the case of argon-grown graphene micro-ribbons without intercalation. These non-intercalated samples contain the so-called buffer layer formed by the graphene-like crystal partially bound to the SiC substrate. The irregular bonding forms an elevated density of the interface states. These interface states become charged in the plasmon field, and their quantum capacitance further red-shifts the plasmon resonance, providing the second contribution to the red-shift in the non-intercalated graphene. Further details can be found in our recent publication [Shestopalov *et al.*, Phys. Rev. B **108**, 045308 (2023)].

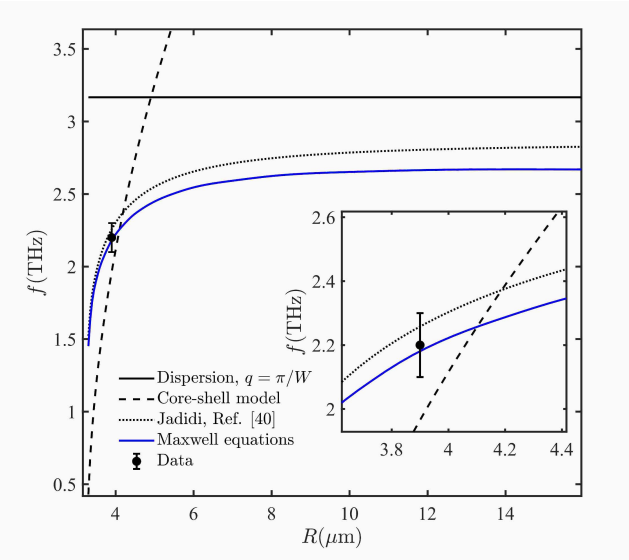

FIG. 13. *We compare four theoretical models, from the simple plasmon-dispersion-based model to the core-shell and equivalent circuit models. We also compare the data to the exact solution of Maxwell equations. The red shift of the plasmon resonance shows the effect of the plasmon-plasmon interaction.*

M. Orlita
J. Kunc, M. Shestopalov, B. Morzhuk (Charles University, Prague)

Magnetic and electric field dependent charge transfer in perovskite/graphene field effect transistors

Perovskite/graphene field effect transistors (FETs) have garnered substantial attention owing to their unique optical properties and potential for applications in electronics and optoelectronics, including ultra-sensitive photon detectors and FETs for metrology.

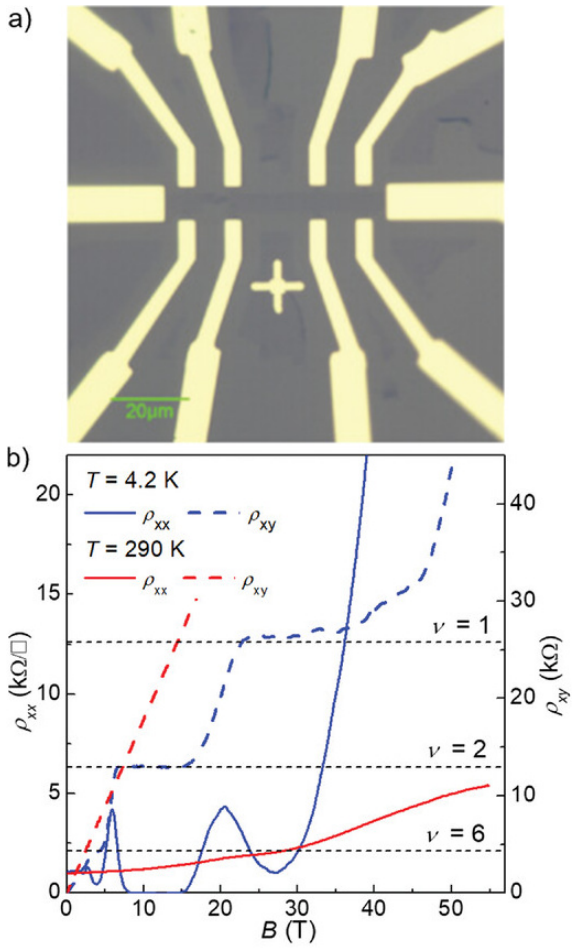

FIG. 14. *Magneto-transport of graphene/CsPb(Br/Cl)$_3$ Hall-bar devices demonstrating a magnetic-field dependent charge transfer. a) Optical image of the sample. b) Longitudinal (solid lines), ρ_{xx}, and transverse (dashed lines), ρ_{xy}, magnetoresistance at zero gate voltage, for $T = 4.2\,K$ (blue), and $290\,K$ (red). Dashed black lines show positions of the quantum Hall-effect plateau with Landau index $\nu = 1$, 2, and 6.*

The charge-transfer processes at the perovskite-graphene interface control the performance of these devices. However, a comprehensive understanding is still lacking especially in the presence of electric and magnetic fields.

In this work we explore the charge transfer in heterostructures of stable all-inorganic $CsPbX_3$ perovskite nanocrystals integrated with high-quality chemical vapor deposition (CVD)-grown graphene on SiO_2/Si substrates. Specifically, the performance of these devices is scrutinized under the influence of high electric fields (up to $3000\,kV.cm^{-1}$) and magnetic fields (up to 60 T) applied perpendicular to the graphene plane (figure 14).

We demonstrate the charge transfer to be markedly sensitive to the presence of electric and magnetic fields, and a slow ($> 100\,s$) charge dynamics. We also find a significant hysteresis in the charge transfer in magneto-transport experiments in constant ($\sim 0.005\,T.s^{-1}$) and pulsed ($\sim 1000\,T.s^{-1}$) magnetic fields. This aspect has not been widely explored in similar systems, and our work proposes a magnetic time constant (τ_{mag}) as a novel concept to explain and model the influence of magnetic fields on charge transfer in these heterostructures.

We also observe quantum Hall-effect plateaus in the transverse magnetoresistance at low temperatures, a testament to the unique quantum phenomena exhibited by graphene in the presence of high magnetic fields. This, along with other observations, signifies the multifunctional potential of perovskite/graphene devices. Moreover, our study yields a two-capacitor model as a valuable tool for describing and understanding the complex charge distribution between graphene and perovskite nanocrystals, further elucidating the hysteresis effects in device behavior.

By offering a deeper comprehension of the underlying physics, this work contributes to the integration of perovskite materials with graphene for applications in electronics and optoelectronics. High magnetic fields emerge as a crucial tool for probing the fundamental physics underpinning these systems.

For more details please see [Cottam *et al.*, Adv. Electron. Mater. **9**, 2200995 (2023)].

W. Escoffier, M. Goiran, M. Pierre
N. D. Cottam, J. S. Austin, A. Patané, L. Turyanska, O. Makarovsky (University of Nottingham), C. Zhang (Shanghai University), C. Coletti, V. Mišeikis (Istituto Italiano di Tecnologia, Pisa)

HF-EPR investigation of graphite anodes

Li-ion batteries are energy storage devices used in a large range of practical applications. Also, they are currently the focus of intense research activity, with the final goal of improving their properties on several aspects (performance, number of cycles, safety,*etc*). In these batteries, graphite is the material mostly used for anodes and its physical and electrochemical properties have been thoroughly characterised. However, questions remain regarding its electronic structure and whether the electrons occupy localised states on Li or delocalised ones on C, or an admixture of both. Here, multifrequency (9 to 441 GHz range) EPR spectroscopy has been used to characterise the electronic states generated during electrochemical cycling through the measurement of the properties of the unpaired electrons in lithiated graphite with different states of lithiation.

To describe Li intercalation in graphite (lithiation of graphite), the Daumas-Hérold mechanism defines four different stages, where the stage number indicates the number of graphite sheets between the Li layers. This simplified model has then been completed, especially with "liquid-like" stages (no Li ordering in the *a*-*b* plane) such as the 2L stage appearing between stages 3 and 2. HF-EPR spectra were recorded on charged graphite at four different states of lithiation (dense stages 1 and 2, dilute stages 2L and 4). HF-EPR spectra were recorded on graphite powders, covered with nonane in order to avoid torquing effects and packed in EPR quartz tubes. Charged graphite at four different states of lithiation (dense stages 1 and 2, dilute stages 2L and 4) were measured at two frequencies (331 and 442 GHz) and four temperatures (between 10 and 170 K). The spectrum obtained for stage 1 sample at 331 GHz and 50 K is displayed in figure 15, showing the increased resolution offered by EPR at high frequencies ($>$ 300 GHz) which enables up to three different electron environments of axial symmetry to be observed. For the other stages, two different electron environments of axial symmetry are identified. For all stages, the quality of the fit obtained at 442 GHz with the same parameters confirmed the model used.

For stage 1, the dominant environment ($\simeq$ 56% in weight) with a g_{iso} of 2.0041 is associated to isotropic hyperfine couplings of $A_{iso} = 4.8$ MHz to two Li nuclei (2 Li in figure 15), corresponding to electrons in the graphite layers with Li^+ above and below the layer. The second environment ($\sim$ 31% in weight) with a g_{iso} of 2.0042 corresponds to electrons with only one Li^+ nucleus (1 Li on figure 15) above or below ($A_{iso} =$ 4.6 MHz) , *i.e.* a stage 2-like environment. Finally, the third axial environment ($\sim$ 13% in weight) at a g_{iso} of 2.0044 shows no hyperfine coupling to Li (0 Li on figure 15), which should come from spins near defects (*e.g.* spins on or near the surface). The actual parameters used for the calculated spectra are: $g_{x,y} = 2.0043$, $g_z = 2.0036$, $A_{x,y} = 5.0$ MHz, $A_z = 4.4$ MHz for 2 Li; $g_{x,y} = 2.0044$, $g_z = 2.0037$, $A_{x,y} = 0.2$ MHz, $A_z = 13.5$ MHz for 1 Li; $g_{x,y} = 2.0045$, $g_z = 2.0042$ for 0 Li. As expected, for the other stages there is no indication of coupling to two Li nuclei. Furthermore, the weight ratio between 1 Li and 0 Li is decreasing with the dilution of the stages.

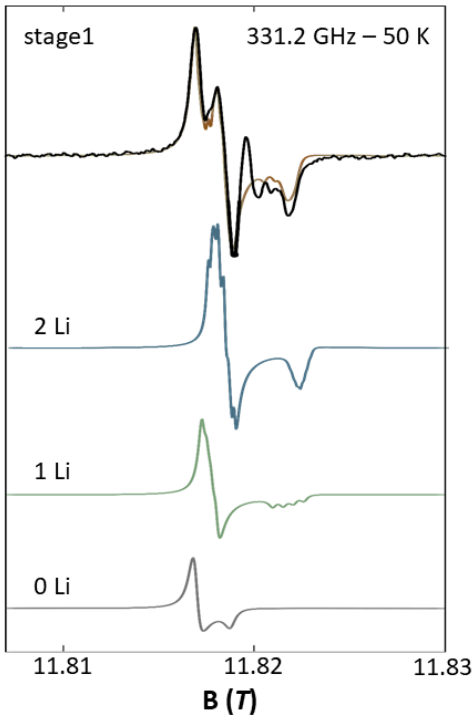

FIG. 15. *Top: Stage 1 EPR experimental spectrum (black) recorded at 331.2 GHz and 50 K and weighted sum of calculated spectra (brown). Below: calculated spectra for the different environments of the electron (0 Li, 1 Li, 2 Li).*

To summarize, HFEPR showed the presence of hyperfine coupling between the metallic electrons and ^{7}Li observed here for the first time. The values obtained point towards electrons occupying mostly carbon-based orbitals in lithiated graphite. For stage 1, the relative weight of the 2 Li and 1 Li components changed as a function of temperature due to changes in conductivity and thus skin-depth effects. It indicates the existence of a Li concentration gradient, with more stage 2-like environments present in the bulk of the particles, which illustrates the difficulty in fully lithiating graphite.

More details of this work can be found in [Insinna *et al.*, Chem. Mater. **35**, 5497-5511 (2023)].

A.L. Barra
T. Insinna, E.N. Bassey, K. Märker, C.P. Grey (Yusuf Hamied Department of Chemistry, University of Cambridge), A. Collauto (PEPR, Imerial College London)

Excitons and trions in WSSe monolayers

Semiconducting transition metal dichalcogenides (S-TMDs) MX_2, which crystallize in the 2H phase, include only five compounds, *i.e.* WS_2, WSe_2, MoS_2, $MoSe_2$ and $MoTe_2$. Monolayers (MLs) of MX_2 are direct-band-gap semiconductors and can emit light more efficiently than their bulk counterparts having indirect band gaps. The fundamental optical transition in S-TMD MLs, the so-called A exciton, spans the spectral range from 1.15 eV for the $MoTe_2$ ML up to $\simeq$ 2.1 eV for the WS_2 ML. One possibility of adjusting the A-exciton energy is to change the layer thickness, but this is accompanied with a change in the band gap character (from direct to indirect) with detrimental effects on the radiative efficiency.

In this work, we investigate the optical response of MLs of WSSe with a S/Se ratio of 57/43 encapsulated in hexagonal BN (hBN) flakes, by means of photoluminescence (PL) spectroscopy. The WSSe ML is ascribed to the family of MLs with a dark ground exciton state, like its "parent" WS_2 and WSe_2 MLs. Our optical spectroscopy investigations furthermore reveal additional emission lines at energies lower than that of the bright excitons. By applying magnetic fields perpendicular and parallel to the layer plane, we are able to determine that these lines arise from bright and dark (spin- and momentum-forbidden) negatively charged excitons and to identify a phonon replica of the dark spin-forbidden charged exciton complex. We finally demonstrate WSSe MLs as a potential platform for quantum communication as these MLs, similar to WSe_2 or WS_2 host centres emitting photons one-by-one, as shown by a clear anti-bunching at zero delay in our auto-correlation measurements of their emission statistics

Figure 16 demonstrates the helicity resolved PL spectra measured on the hBN-encapsulated WSSe ML in magnetic fields up to 30 T oriented perpendicularly to the ML plane. Due to both the large binding energies of free excitons and their huge reduced masses in S-TMD MLs, applying the out-of-plane magnetic field results mostly in the exciton Zeeman effect (the diamagnetic shift of the ground excitonic states can hardly be seen in magnetic fields as high as 70 T), which manifests itself as a splitting of the two counter-circularly-polarised components of a given transition ($\sigma\pm$). All the observed emission lines split into two $\sigma\pm$ components, but the magnitude of the Zeeman splittings differs, providing us with a tool to identify the different complexes.

Through the application of in-plane and out-of-plane magnetic fields, the four main emission lines apparent in the low-temperature PL spectra were ascribed to the neutral bright exciton, the bright and dark (spin- and momentum-forbidden) negatively charged excitons, and the phonon replica of the dark spin-forbidden trion.

Our results show that alloyed S-TMD MLs can represent a powerful material platform to widen the spectral range of operation of 2D crystals for optoelectronics and quantum technology applications.

More information about this work can be found in [Olkowska Pucko *et al.*, 2D Materials **10**, 015018 (2023)].

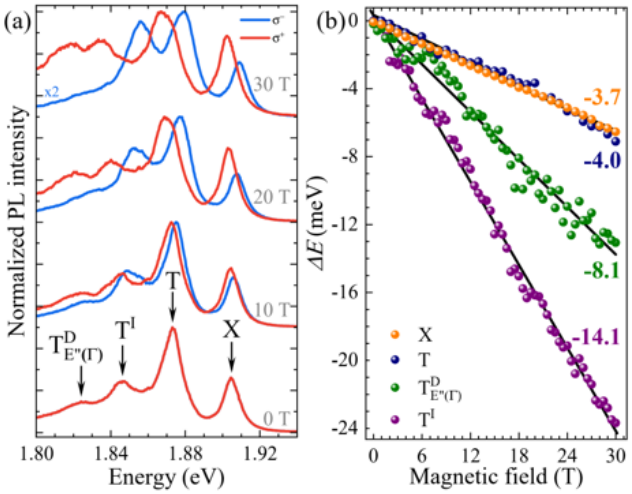

FIG. 16. *a) Helicity-resolved PL spectra of an hBN encapsulated WSSe monolayer at $T = 4.2$ K measured at selected values of the applied out-of-plane magnetic field. The red (blue) colour corresponds to the $\sigma+$ (σ-) polarized spectra. The spectra are vertically shifted for clarity. b) Energy difference between the two circularly polarized split components of the X, T, TI, and $T^D_{E''(\Gamma)}$ transitions as a function of out-of-plane magnetic field.*

D. Vaclavkova, P. Kapuscinski, D. Jana, C. Faugeras, M. Potemski
K. Olkowska Pucko, N. Zawadzka, K. Nogajewski, M. Bartos, A. Babinski, M.R. Molas (Faculty of Physics, University of Warsaw), E. Blundo, S. Cianci, G. Pettinari, M. Felici, M. Polimeni (Physics Department, Sapienza University, Rome), T. Tanigushi, K. Watanabe (NIMS, Tsukuba)

Spin-defect characteristics of single sulfur vacancies in monolayer MoS_2

Spin-defects in host crystals can be fundamental building blocks for quantum technologies, such as computing, sensing or communication. For instance, color centers in diamond have been investigated since the early 1980s, of which the nitrogen vacancy (NV) center is the most prominent example. In this defect, the crystal field splitting lifts the ground state spin degeneracy and provides the required unique quantum degree of freedom to form an addressable two-level system. In addition, NV centers are single photon sources and therefore constitute excellent building blocks for future quantum photonic circuits. However, a key prerequisite for such applications is the ability to position defects deterministically. This is a challenge for defects in 3D crystals, such as single NV centers, as they can be positioned either vertically or laterally with high precision, but not both simultaneously.

First approaches for the deterministic creation of quantum emitters in 2D materials made use of strain potentials, for instance induced by a textured substrate. This results in a local band structure modulation in the host crystal, limited by the bending radius of the material, yet the latter approach intrinsically lacks reproducibility. Furthermore, the confining potential often breaks crystal symmetries, leading to the loss of valley optical selection rules. A higher degree of spatial resolution and reproducibility can be achieved by using the accuracy of electron-beam or focused ion beam irradiation. Specifically, He-ions can be precisely focused and create optically active point defects in monolayer MoS_2 with a precision better than 10 nm. In photoluminescence (PL) spectroscopy, spectrally narrow emission lines appear about 200 meV red-shifted from the neutral exciton of He-ion irradiated MoS_2. Second order correlation measurements unambiguously showed single photon emission from single He-ion irradiation sites, which in turn could be related to the generated point defects. A specific advantage is that these defects can be implanted into more complex, electronic device heterostructures, allowing for the electrical control of quantum emission.

We identify the bands involved in the optical quantum emission and show that an energy-dependent degree of hybridization between atom-like defect states and the MoS_2 band structure leads to varying degree of valley selectivity for the distinct electron-hole transitions. Our results display that sulfur vacancies in monolayer MoS_2 are spin-defects that can be tailored to specific quantum applications.

To further investigate the details of the electronic states involved in the emission lines Q1 and Q2, we turn to magneto-spectroscopy in the Voigt configuration for which the magnetic field is applied parallel to the sample plane and perpendicular to the optical beam path. This experimental configuration together with the main results of our study are presented in figure 17. The fact that the emission line Q1 is energetically higher than Q2, while the diamagnetic shift, and therefore the binding energy of Q1 and Q2 are essentially the same, requires the defect band vD to be located below the valence band edge of MoS_2, as sketched in figure 17.

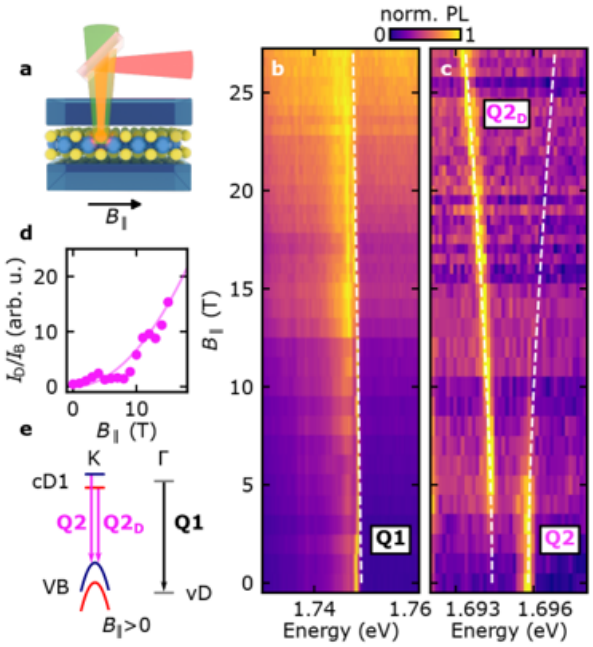

FIG. 17. *In-plane magnetic field B measurements on the photoluminescence of defect luminescence Q1 and Q2. a) Sketch of the in-plane magnetic field in-plane B configuration (Voigt geometry). No polarization optics were used in the detection path. b) Emission of Q1 remains bright for all fields. c) The in-plane field reveals a second state Q2D energetically below Q2. The white dashed lines are guides to the eye for the expected in-plane Zeeman shift of Q1 and the dark-bright-splitting of Q2. The dark-bright splitting $\Delta_{DB} = 1.4\,meV$ for Q2. d) The quadratic dependence of the emission ratio between Q2D and Q2 indicates the brightening of a dark ground state. e) Sketch of the defect levels with the possible optical transitions for Q1 and Q2 at finite in-plane B.*

More information can be found in [Hotger *et al.*, npj 2D Materials and App. **7**, 30 (2023)].

T. Pelini, A. Delhomme, M. Potemski, C. Faugeras A. Hotger, K. Barthelmi, C. Kastl, J.J. Finley, A.W. Holleitner, A.V. Stier (Walter Schottky Institute, Munich), J. Klein (Massachusetts Institute of Technology, Cambridge), T. Amit, G. Cohen, D. Hernangomez-Perez, S. Refaely-Abramson (Weizmann Institute of Science, Rehovot), S. Rey (Technical University of Denmark, Lyngby), T. Tanigushi, K. Watanabe (NIMS, Tsukuba)

Control of the valley polarization by Dexter-like coupling

Transition metal dichalcogenides (TMDs) are a well known 2D semiconductor class of materials due to their exceptional optoelectronic properties. They are especially known for the spin-valley locking effect that endows them with a binary degree of freedom referred to as valley pseudospin. It can be addressed via the use of circularly polarized light which allows for selective excitation (or read-out) of one of the two K and K' valleys. The imbalance of the exciton population between the valleys is known as the valley polarization (VP).

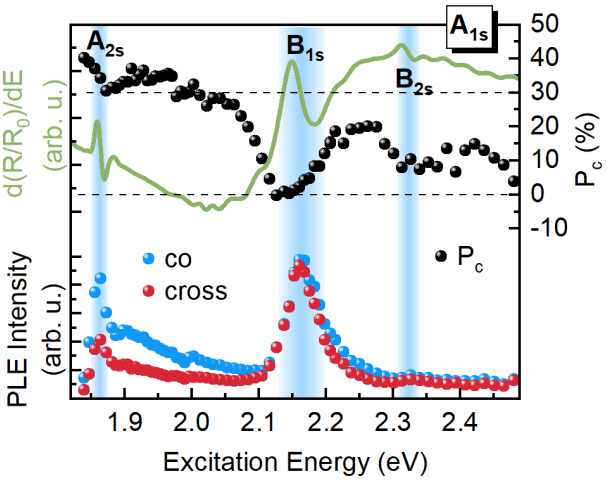

FIG. 18. *Circular polarization resolved PLE of the A_1s exciton (green and red spheres corresponding to the PLE intensity of the co-polarized and cross-polarized emission, respectively) with calculated degree of circular polarization P_c (black spheres) as well as a reflectivity (green line).*

We have investigated the valley polarization properties of an encapsulated monolayer of WSe_2. In TMDs the VP is strongly affected by various intervalley scattering mechanisms. One of the most prominent roles is played by the Dexter-like coupling [Berghäuser *et al.*, Nat. Comm. **9(1)**, 971 (20218)], which, under resonant excitation conditions, couples the same-spin states of the A and B excitons between the valleys facilitating an efficient intervalley transfer of coherent bright excitons.

To investigate the possibility of controlling the value and sign of the valley polarization we have performed circular-polarization resolved PLE measurements from which we calculate the energy-dependent value of $P_c = (I_{co} - I_{cr})/(I_{co} + I_{cr})$, where $I_{co/cr}$ denotes the intensity of the co-polarized/cross-polarized emission, respectively. Due to spin-valley locking, this quantity directly corresponds to the VP. Tuning the excitation energy, we observe a generally positive VP of the A_{1s} exciton which however strongly decreases when the excitation energy crosses either the B_{1s} or B_{2s} resonance, especially pronounced at the B_{1s} resonance, where the VP vanishes (figure 18). This is a direct consequence of the Dexter-like coupling mechanism. Furthermore, if we focus on other excitonic complexes such as biexciton (XX) and charged biexciton (XX^-) we observe that they are more strongly affected by the Dexter-like coupling, as their polarization becomes clearly inverted (reaching $\sim -7\%$) when the excitation is near the B_{1s} resonance (figure 19). This is related to the fact that more complex excitonic particles are less prone for the subsequent depolarizing processes.

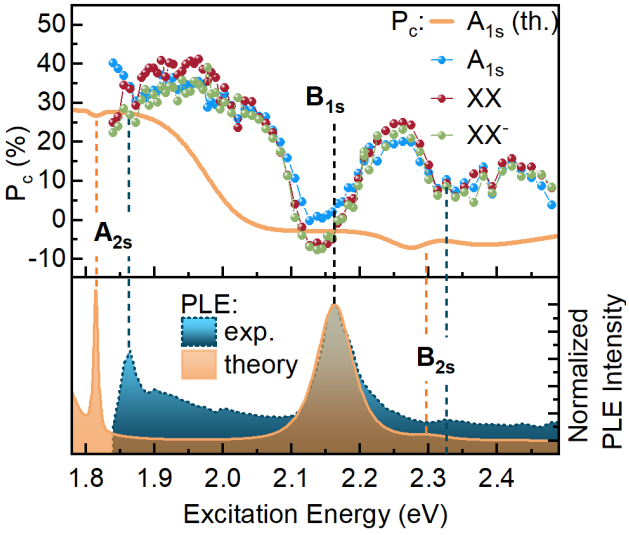

FIG. 19. *Comparison of simulated (for the A_{1s} exciton) and experimental (for A_{1s}, XX and XX^- excitons) P_c curves as a function of excitation energy (top) and corresponding normalized PLE intensity (bottom).*

Finally, we compare the experimental results with a fully microscopic theoretical simulation (figure 19), which reproduces the energy dependent VP effects with a good qualitative agreement. The simulated VP curve shows a flatter dependence in the region of B states due to the overlapping resonance broadenings of the B states, while the experimental curve shows a clear rise of the VP in between the B_{1s} and B_{2s} states. This can be related to discrepancies between the structure parameters in the simulation and of the real structure or to additional intervalley scattering effects not taken into account in the calculations.

In conclusion, we have shown that utilizing the effects of the Dexter-like coupling by tuning the excitation energy, becomes an additional handle to control the valley polarization in TMDs, which is especially promising for applications in valleytronics and spintronics.

J. Jasiński, S. Palai, D.K. Maude, P. Plochocka
M. Baranowski, M. Dyksik (Wroclaw University of Science and Technology), J.J.P. Thompson, E. Malic (University of Marburg)

Transition metal dichalcogenide moiré structure after AFM ironing

The assembly of highly aligned transition metal dichalcogenides reveals unique electronic and optical properties driven by the emergence of moiré patterns. However, challenges arise due to the atomic thickness and high surface-to-volume ratio, which necessitates achieving optimal interface quality. To address this, we introduce an innovative post-stacking technique using an atomic force microscope (AFM) tip to iron the layers, significantly improving interface homogeneity.

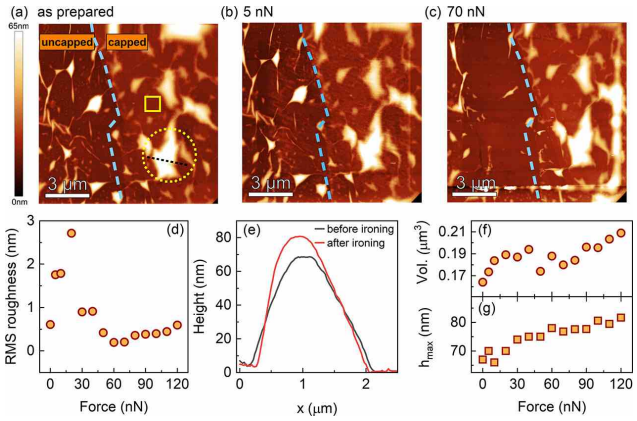

FIG. 20. *(a-c) Topographic AFM images for as-prepared samples and after ironing. (d) Root-mean-square (RMS) values plotted against ironing forces. (e) Height profile of the bubble of interest before and after ironing with 120nN. (f) Volume (V) and (g) height (H) of the bubble of interest versus applied force.*

This process enhances layer coupling, leading to a more pronounced moiré effect and reduced disorder, notably impacting the optical response of interlayer excitons. This breakthrough in TMD heterostructure physics promises researchers a precise and consistent avenue to unravel the intricate properties of TMD stacks.

We investigated a MoS_2 monolayer on a hBN substrate, partially capped by another hBN flake. The as-fabricated sample, examined in dynamic AFM mode, showed bubbles and wrinkles from exfoliation. Contact mode scans (5 nN to 120 nN) (figure 20) on a $10 \times 10\,\mu m^2$ area revealed that at low forces (< 20 nN), debris and adsorbates clustered, creating ripples and increasing roughness. Beyond 30 nN, extensive areas, especially in the uncapped MoS_2 region, were cleared of bubbles and wrinkles, demonstrating the ironing process's efficacy.

To understand the effect of ironing on interlayer coupling we perform a comprehensive statistical analysis of the photoluminescence (PL) spectra throughout the heterostructure (figure 21). Ironing induced a redshift in the intermayer exciton (IX) transition proportional to the applied force. The emission line broadening increased on average with a coefficient of $0.26 \pm 0.07\,\mu$eV/nN. Additionally, ironed regions showed a 15% average increase in PL intensity, attributed to enhanced layer contact post-AFM treatment. Ironing the heterostructure narrows distributions for all three parameters, reducing standard deviations by 50% (σ/σ_0) when compared with as-prepared sample parameters. The improved interface quality, resulting in decreased RMS roughness and fewer bubbles and wrinkles, is key to achieving spatially uniform optical spectra. For more information please see [Palai *et al.*, Nano Lett. **23**, 4749 (2023)].

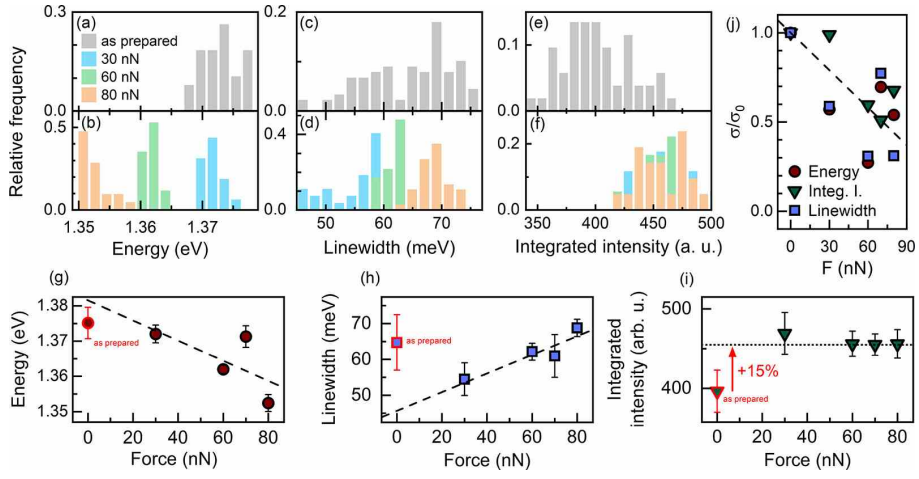

FIG. 21. *PL energy, line width, and intensity distributions for non-ironed and ironed heterostructure areas. Average IX transition energy, line width, and PL intensity with linear fits as a function of ironing force. (j): Standard deviation σ normalized to $\sigma 0$ for IX parameters versus ironing force.*

S. K. Palai, N. Sokołowski, D. K. Maude, P. Plochocka.
M. Dyksik, A. Surrente, M. Baranowski (Wroclaw University of Science and Technology, Wroclaw), A. Castellanos-Gomez, C. Munuera (ICMM-CSIC, Madrid)

Twist-angle dependent dehybridization of momentum-indirect excitons in $MoSe_2/MoS_2$ heterostructures

Van der Waals crystals enabled novel 2D heterostructure engineering. Vertically stacked transitions metal dichalcogenides MoS_2 and $MoSe_2$ monolayers have intriguing band alignment, where the minimum of the conduction band remains at the K point, indicating the spatial localization of electrons within MoS_2 monolayer, while hybridization determines the valence band's maximum point at the Γ point, indicating the hole delocalization between the two monolayers. Consequently, the ground state with the lowest energy is a hybrid interlayer exciton, which has an indirect nature in both real space and k-space, as illustrated in figure 22.

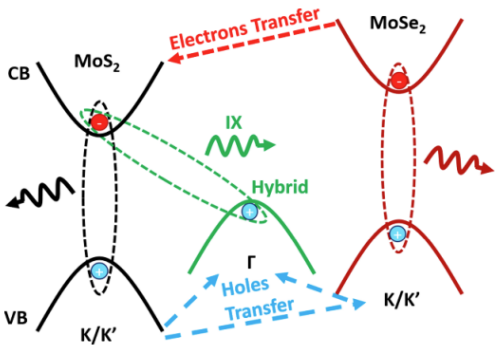

FIG. 22. *Schematic of electron and holes transfer between different valleys in a $MoSe_2/MoS_2$ heterostructure. The two intralayer excitons and the hybridized interlayer exciton are indicated by red/black and green ovals, respectively*

Hybridization arises from the overlap of the atomic wave functions of the two adjacent layers. Therefore, it mostly affects states derived from the chalcogen atomic orbitals, such as the states around the Γ point in the Brillouin zone. The energy of the hybridized states is anticipated to exhibit a significant dependence on the interlayer twist angle. The spatial separation between the layer depends on the twist angle, thus tuning this parameter can lead to the dehybridization of the interlayer exciton. On the other hand, states in the proximity of the K points are expected to experience only a minimal impact from interlayer hopping (coupling). This is due to the fact that the associated orbital functions primarily localize around the transition metal atoms positioned within the central layer of the chalcogen-metal-chalcogen sandwich.

Figure 23(a) demonstrates the photoluminescence (PL) spectrum at various twist angles. The PL peak's energy blue shifts when the twist angle moves away from 0° or 60°. Extracted energies of the lower energetic interlayer exciton (IX1) are plotted in Figure 23(b) (depicted as open circles). This large blue shift can reach up to 100 meV when going from 0° to $6-7°$, which confirms the hybrid nature of the interlayer exciton. This suggests that the interlayer twist angle can act as a strong tuning knob of the hybrid interlayer exciton energy.

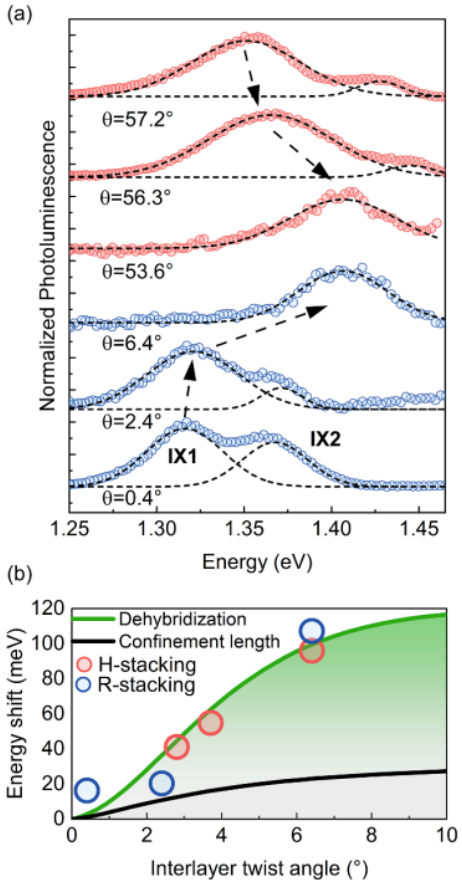

FIG. 23. *(a) Photoluminescence spectra of samples with different twist angles. (b) Calculated energy shift of moiré excitons in R-type stacking taking into account only confinement length (black) and total blue shift including the dehybridization effect (green), which agrees with the shift of the dominating IX1 transition (open circles).*

For more details please see [Sokołowski,, et al. 2D Mater. 10 034003 (2023).].

N. Sokołowski, S. Palai, D.K. Maude, P. Plochocka
M. Dyksik, K. Posmyk, A. Surrente, M. Baranowski (Wroclaw University of Science and Technology) O. Çakiroğlu, F. Carrascoso, E. Sanchez, Y. Xie, A. Schubert, A. Castellanos-Gomez, C. Munuera (ICMM-CSIC, Madrid) T. Taniguchi, K. Watanabe (NIMS, Tsukuba) Joakim Hagel (Chalmers University of Technology, Gothenburg), Samuel Brem, Ermin Malic (Philipps University, Marburg)

In-plane anisotropy in the van der Waals antiferromagnet $FePSe_3$ probed by magneto-Raman scattering

van der Waals (vdW) magnets, layered materials including magnetic ions, are today at the heart of an intense effort to investigate and characterize their magnetic properties. This family of materials includes a broad variety of magnetic ground states such as ferromagnetism in CrI_3 or $Cr_2Ge_2Te_6$ and antiferromagnetism in the MPX_3 family, where M=Fe, Cr, Co, Mn, Ni and X=S or Se, together with a rich physics of interlayer ferro- or antiferromagnetic interaction across the vdW gap. Magnons are among the possible elementary excitations of magnetic systems and investigating their properties provides a unique knowledge of the magnetic ground state.

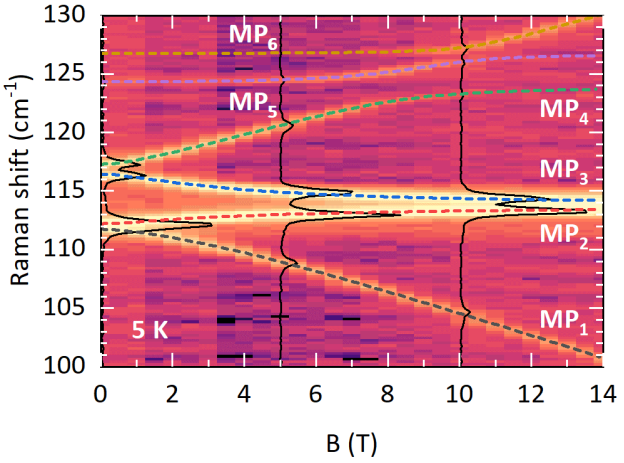

FIG. 24. *False color map of low-temperature Raman scattering of $FePSe_3$ as a function of the magnetic field applied along the crystal c-axis. A few representative scattering spectra, measured at magnetic field strengths of 0 T, 5 T, and 10 T are also plotted. The coupled magnon-phonon modes are labelled as MP_i.*

The magnon-phonon interaction in magnetic materials has recently attracted significant interest due to its influence on magnon dynamics, a critical aspect in the field of magnontronics. In the case of iron-based antiferromagnets, the strong single-ion anisotropy of Fe-ion boosts the magnon energy in the range of meV (with respect to μeV for other compounds). This allows one to investigate the physics of magnon excitations using Raman scattering techniques with a typical low energy cut-off around 1 meV and with a spatial resolution of $\sim 1\mu$m. Such high magnon energy coincides with energies of optical phonons in covalent solids, indicating a possible influence of the magnon-phonon interaction on the observed magnon or phonon energies.

Understanding the source of magnon nondegeneracy is vital for gaining detailed knowledge about the magnetic system and its interacting state. A recent report [Cui *et al.* Nature Communications **14**, 3396 (2023)] indicates that the magnon gap in bulk $FePSe_3$ is nearly degenerate with a pair of optical phonon modes with chiral character. The magnon-phonon interaction in bulk $FePSe_3$ is hence chirality selective, very distinct from the one observed in the analogous compound $FePS_3$ where both magnons couple independently to the same phonon mode.

In this study, we employ Raman scattering techniques under varying environments, including temperatures ranging from $T = 5\,\mathrm{K}$ to $T = 140\,\mathrm{K}$ and magnetic fields up to $B = 30\,\mathrm{T}$, to disentangle coupled magnon-phonon excitations in bulk $FePSe_3$ and identify the origin of zero-field splitting of the coupled modes in the case of selective magnon-phonon interaction. We have used a magnon-phonon coupling matrix formalism to reproduce our experimental data and extract the bare modes energies, type of coupling, the magnon-phonon coupling constants, and the coupled mode composition in terms of bare modes. Our findings reveal two non-degenerate magnon gap excitations (of $1.2\,\mathrm{cm}^{-1}$ energy difference at low temperature) selectively coupled with two degenerate phonons, leading to the apparent splitting in the phonon modes. Our experiments indicate an intrinsic lifting of the magnon degeneracy, most probably representative of a weak in-plane anisotropy.

More details about this work can be found in [Jana *et al.*, Physical Review B **108**, 144415 (2023)].

D. Jana, P. Kapuscinski, A. Pawbake, I. Breslavetz, M. Orlita, M. Potemski, C. Faugeras A. Papavasileiou, Z. Sofer (Department of Inorganic Chemistry, University of Chemistry and Technology, Prague)

Magnon gap excitations and spin-entangled optical transition in van der Waals antiferromagnet $NiPS_3$

Scientific curiosity and the possible design of novel devices continue to drive pertinent research efforts focused on two-dimensional materials. Among systems of intense current interest are the antiferromagnets from a large family of transition metal phosphorus trichalcogenides (MPX_3), where M represents transition metal ions and X represents chalcogen ions.

The magnetic ordering in these antiferromagnets is governed by the spin-spin exchange interactions among the neighbouring spins while the direction of the spin is governed by the magnetic anisotropies. Distinct exchange and anisotropy parameters give rise to specific magnon gaps, crucial components in understanding various physical properties of magnetic systems with potential applications in spintronics.

In this work, we have employed Raman scattering and far-infrared transmission measurements, carried as a function of temperature and of the magnetic field, to clarify the properties of $NiPS_3$ van der Waals antiferromagnet. Our study reveals $NiPS_3$ as a biaxial antiferromagnet with two fundamental magnon-gap excitations (at 1.25 meV and 5.33 meV) at the $k = 0$ point. Several relevant parameters, including the spin-flop field ($\simeq$ 10 T), Landé g-factor ($\simeq$ 2.15), and ratio of the anisotropy fields ($\simeq$ 18), were determined through the magnetic field dependence of the magnon gaps.

In the antiferromagnetic phase of $NiPS_3$, we also found an optical excitation in the near-infrared spectral region that is entangled with the magnetic ordering. Appealingly enough, this transition has been identified as a collective excitation, the spin-entangled excitonic transition between Zhang-Rice triplet and singlet states. Our observations, of the magnetic field-induced splitting of this transition in particular, raise pertinent questions about its attribution as a many-body coherent excitonic transition.

Although the origin of this optical transition remains unclear, we speculate that the sub-bandgap "excitonic" transition is associated with the internal transition of the metal ion, manifesting in the antiferromagnetic phase of $NiPS_3$ due to symmetry breaking.

More details about this work can be found in [Jana *et al.*, Physical Review B **108**, 115149 (2023)].

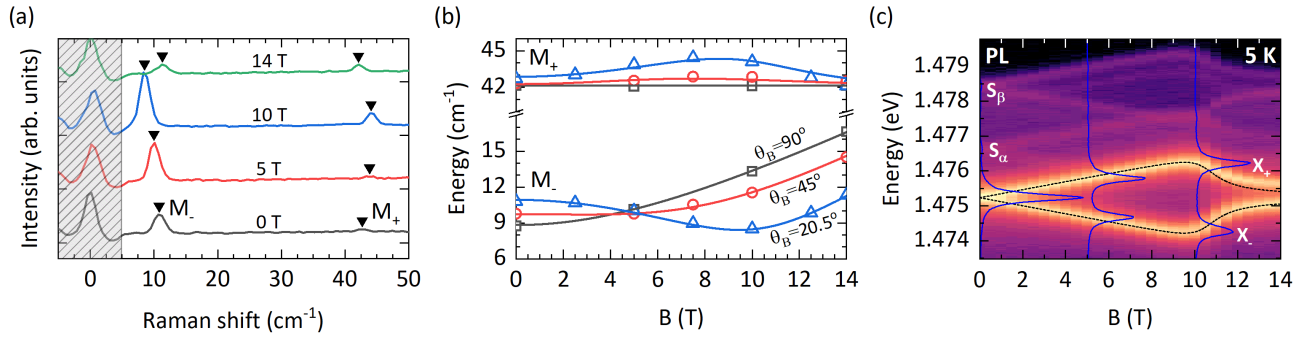

FIG. 25. *(a) Low temperature(5 K) Raman scattering spectra of exfoliated $NiPS_3$ flake at the magnetic field strength of 0 T, 5 T, 10 T, and 14 T. (b) The evaluation of magnon gap excitations (M_+ and M_-) as a function of the magnetic field applied at different angles in the crystal a-b plane with respect to the crystal a-axis. (c) False color map of low temperature (5 K) PL of $NiPS_3$ exfoliated flake as a function of the in-plane magnetic field. A few representative PL spectra, measured at a magnetic field strength of 0 T, 5 T, and 10 T are also plotted to show the magnetic field-dependent evaluation of spin-entangled optical transition (X).*

D. Jana, P. Kapuscinski, I. Mohelsky, D. Vaclavkova, I. Breslavetz, M. Orlita, C. Faugeras, M. Potemski

Raman scattering signature of strong spin-phonon coupling in the bulk magnetic van der Waals material CrSBr

Two-dimensional (2D) magnetic semiconductors give the opportunity to take advantage of the electron charge and the electron spin at the same time, which gives the possibility of broadening modern semiconductor technology and spintronic devices and can greatly expand the applications of ferromagnets (FM) in other devices such as transformers, electromagnets, high-density storage, and magnetic random access memory.

CrSBr belongs to ternary chromium chalcogenide halide compounds (CrXh, where X = S/Se and h = Cl/Br/I) that have recently been widely investigated. Bulk CrSBr, first synthesised 50 years ago, has attracted attention because it was thought to be an antiferromagnetic (AFM) semiconductor with the bulk Néel temperature of $T_N = 132\,\mathrm{K}$. Under ambient conditions, CrSBr has an orthorhombic structure with a Pmmn space group. The crystal structure of CrSBr is formed by the two Cr layers bounded by S atoms and passivated by Br layers along the c-axis. CrSBr is a van der Waals crystal, therefore, it can be easily exfoliated down to the monolayer thickness using conventional mechanical exfoliation techniques. CrSBr has been identified as an extremely interesting and unique van der Waals type magnetic semiconductor, having the band gap in the near-infrared region between 1.25 eV and 1.5 eV, The electronic properties of CrSBr are strongly anisotropic and this is reflected in its optical and transport properties.

In this work, We use Raman scattering spectroscopy to detect the magnetic phase transitions in bulk CrSBr when lowering temperature. By tilting the sample with respect to the excitation light propagation direction, we activate Raman scattering from phonons at the Z-point of the Brillouin zone which are particulary sensitive to the AFM ordering along the c-axis. The strong spin-lattice coupling is evidenced through the appearance of new phonon modes when the additional magnetic periodicity develops below T_N and by pronounced variations of the scattered intensity. These changes in the Raman scattering spectrum allow identification of the intermediate magnetic phase when $T_C \geq T \geq T_N$, the AFM order, and also the hidden order phase below T*.

We show that the evolution of phonon modes when lowering temperature from room temperature down to liquid helium temperature cannot be described by usual lattice dynamics and strongly reflects the magnetic ordering and the different magnetic phases in this bulk compound (figure 26(a)). we have simultaneously measured the photoluminescence from excitons in bulk CrSBr, which have been shown to be a probe of the saturation field, above which all the spins are aligned along the direction of the external magnetic field. These results are shown in figure 26(b-d) for the unpolarized magneto-photoluminescence and magneto-Raman scattering, respectively. When measuring the magneto-Raman scattering response, we observe that the 57 cm^{-1} mode observed in the AF phase gradually disappears when the saturation field is reached, in our tilted configuration for $B \geq 0.8\,\mathrm{T}$, and the 71 cm^{-1} phonon mode is recovered. Simultaneously, the B_{2g}^2 phonon observed at 305 cm^{-1} strongly gains in intensity for $B \geq 0.8\,\mathrm{T}$. This magnetic field corresponds to the saturation magnetic field extracted from magneto-photoluminescence, confirming that observing the B_{3g} from the Z point at 57 cm^{-1} is a characteristic signature of the AFM phase.

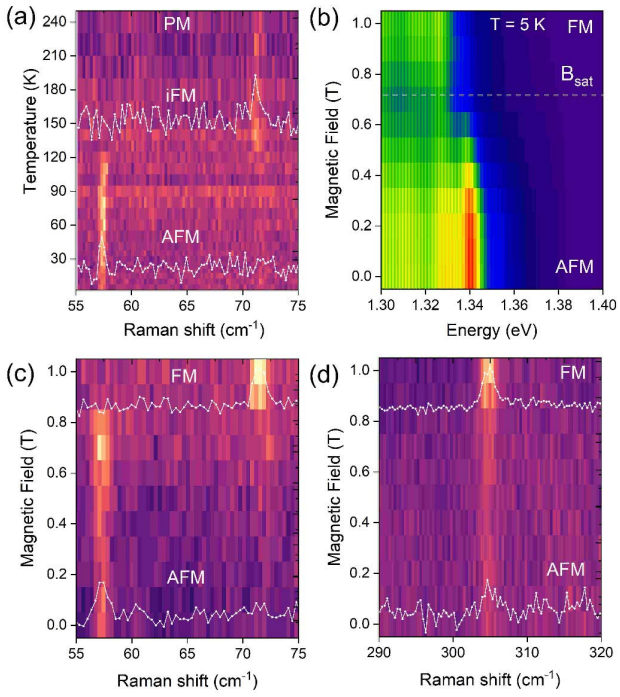

FIG. 26. *(a) Evolution of the unpolarized Raman scattering response measured at various temperatures between $T = 5\,K$ up to $T = 250\,K$, (b) magnetophotoluminescence of bulk CrSBr up to $B = 1\,T$ with the B field applied 30° from the c-axis and showing a saturation field of $B_{sat} = 0.75\,T$, and (c-d) magneto-Raman scattering response at $T = 5\,K$ with the B field applied in the same configuration as in panel (b) for two different energy windows centered on the B_{3g} phonon mode (c) and on the B_{2g} phonon modes (d).*

This clearly relate the evolution of the Raman scattering response to the magnetic ordering in bulk CrSBr. More details about this work can be found in [Pawbake *et al.*, Phy. Rev. B. **107**, 075421 (2023)].

A. Pawbake, T. Pelini, C. Faugeras
N. Wilson (Technical University of Munich), K. Mosina, Z. Sofer (Department of Inorganic Chemistry, University of Chemistry and Technology, Prague), R. Heid (Karlsruhe Institute of Technology)

Probing the pressure driven magnetic ground states in bulk CrSBr

The generation of new magnetic phases by an external manipulation of the magnetic state is a requirement for the implementation of new spintronic and magnontronic functionalities. Successful manipulations of magnetic states have been achieved by using spin-polarized electrical currents, electrostatic gating, or ultrafast laser excitations. An alternative approach relies on the direct modification of the magnetic interactions by changing the lattice parameters and/or the super exchange paths by applying strain or hydrostatic pressure.Such profound modifications affect both direct exchange magnetic interaction and spin-orbit interactionrelated effects, such as magneto-crystalline anisotropy, which determines the preferential directions of spins in a magnetically ordered solid and the spin wave energy. Due to weak van der Waals (vdW) gap, interlayer spacing can be tuned efficiently through the application of hydrostatic pressure.

Such changes strongly affect the short-range interlayer interactions and the competition between magnetic exchange interactions and magnetic anisotropies. New magnetic phases can be engineered in a magnetic system by changing the competition between the anisotropies and exchange interactions.

In work, we apply hydrostatic pressure to bulk CrSBr to tune the interlayer magnetic exchange interaction and the magnetocrystalline anisotropies (D and E). We sense the induced changes by magneto-photoluminescence measurements with an external magnetic field applied along one of the three crystallographic axis. The interlayer exchange parameter ($J_\perp$) responsible for the antiferromagnetic (AFM) ordering is small in bulk CrSBr because of its lamellar structure. When the vdW gap is decreased, we observe an increase of $J_\perp$ by 1700% at P $>$ 6 GPa.

This large increase with respect to magnetocrystalline anisotropies stabilizes CrSBr into a particular magnetic ground state characterized by an intermediate spin-flop phase appearing between the AFM ground state at $B = 0$ and the ferromagnetic (FM) ground state when an external magnetic field, exceeding the saturation field, is applied (figure 27). This spin-flip transition (AFM to FM) observed along easy axis when $(D - E) > 2J_\perp$ (strong anisotropy regime). On the basis of low-temperature magneto-photoluminescence measurements under such extreme experimental conditions, we have identified a spin-flop phase stabilized when the interlayer exchange interaction strongly exceeds the magnetic anisotropy.

These results are understood in the frame of a spin Hamiltonian including magneto-crystalline anisotropies, which describes the appearance of the spin-flop magnetic phase when $(D - E) < 2J_\perp$ (weak anisotropy regime). Compared with the experimental results, this model provides values for the microscopic parameters entering the spin Hamiltonian, and their evolution can be traced up to $P = 6$ GPa. This work demonstrates the possibility of tailoring the competition between magnetic crystalline anisotropy and interlayer exchange interaction of vdW magnets by external means and enlarges the technical possibilities for the design of two dimensional magnets.

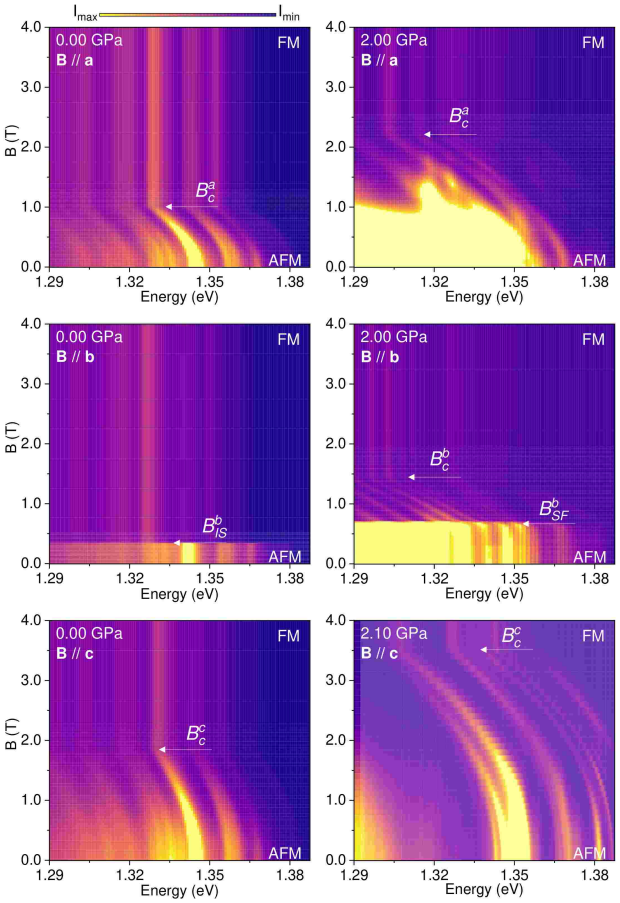

FIG. 27. *False color maps of the low-temperature magneto-photoluminescence response of bulk CrSBr for the different values of hydrostatic pressure when the magnetic field is applied along the a-axis (top), the b-axis (middle), and the c-axis (bottom). The white arrows indicate the critical magnetic fields.*

More details about this work can be found in [Pawbake *et al.*, Nano Letters **23**, 958(2023)].

A. Pawbake, T. Pelini, I Mohelsky, D. Jana, I. Breslavetz, C. Cho, M. Orlita, M. Potemski, B. Piot, C. Faugeras
N. Wilson (Technical University of Munich), M. Measson (Institut Néel-CNRS, Grenoble), K. Mosina, A. Soll, Z. Sofer (Department of Inorganic Chemistry, University of Chemistry and Technology, Prague), M. Zhitomirsky (CEA, Grenoble)

Microwave absorption spectroscopy of the van der Waals antiferromagnet CrSBr

The observation of ferromagnetism in two dimensions and the discovery of magnetically and electrically tunable van der Waals bond few-layer compounds have boosted interest in the so-called van der Waals (vdW) magnets new class of materials. This has stimulated the search for new layered magnetic systems, as well as expanding the exploration of partially studied ones, even in their bulk forms.

Among vdW magnets, layered antiferromagnets such as CrI_3, $CrCl_3$, and CrSBr have the particularity of hosting a low-temperature antiferromagnetic order associated with an alternating magnetic moment orientation between adjacent layers. At variance with typical (covalently bond) antiferromagnets, the weak interlayer exchange coupling in these vdW systems allows for the use of moderate magnetic fields to manipulate the Néel vector. In CrSBr, there exists a significant additional biaxial anisotropy that further defines a preferred in-plane magnetic moment direction (along the so-called easy axis).

CrSBr has the additional advantage of being an air-stable semiconductor, the thickness of which can be adjusted down to the monolayer with a demonstrated coupling between magnetic order and charge transport. This makes it a promising system for integration in spin-based electronic devices, which motivates the need for an accurate description of its internal microscopic parameters.

In this work, we present a microwave absorption study of the low-energy magnon excitations in bulk CrSBr, which employs a phase-sensitive external resistive detection technique. Strong resonant signals are observed in a large frequency/magnetic field phase space, for frequencies continuously tuned up to 60 GHz and magnetic fields up to 10 T, which is well-above the saturation fields of local moments. The magnetic-field dependence of two antiferromagnetic magnon modes is measured along the three principal crystallographic directions, the (hard) c-axis, the (intermediate) a-axis, and the (easy) b-axis (see figure 28).

Our observations reveal anisotropies, magnetic transitions, and a strong magnon-magnon coupling in this material. To account for the observed results, we formulate a microscopic spin model with a bi-axial single-ion anisotropy and interplane exchange. Theoretical calculations give an excellent description of full magnon spectra, enabling us to precisely determine microscopic interaction parameters for CrSBr. The extracted parameters are consistent with the weak interlayer coupling and easy axis nature of CrSBr, and can be used as a foundation to compute and engineer magnetic phases transitions and devices in this promising material.

For more details please see [Cho *et al.*, Phys.Rev.B **107**, 094403 (2023)].

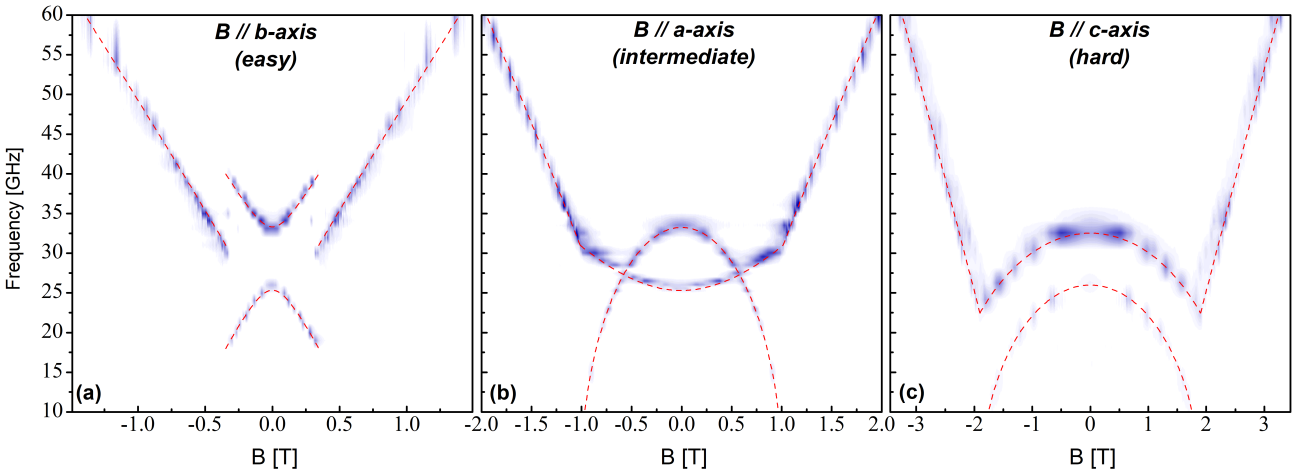

FIG. 28. *Absorption spectra for a magnetic field B along the b, a, and c axes as indicated in each panel. Color plots of the phase variation of the thermometer photo-resistance as a function of microwave frequency and magnetic field B. The phase difference with respect to its median ("off-resonance") value is color-coded from 0 (white) to −8% (dark blue). Fits (red dashed-lines) obtained with our microscopic model.*

C. W. Cho, A. Pawbake , N. Aubergier, A. L. Barra, C. Faugeras, B. A. Piot
M. E. Zhitomirsky (CEA, IRIG, Pheliqs, Grenoble), K. Mosina, Z. Sofer (Department of Inorganic Chemistry, University of Chemistry and Technology, Prague)

Semiconductors and Nanostructures

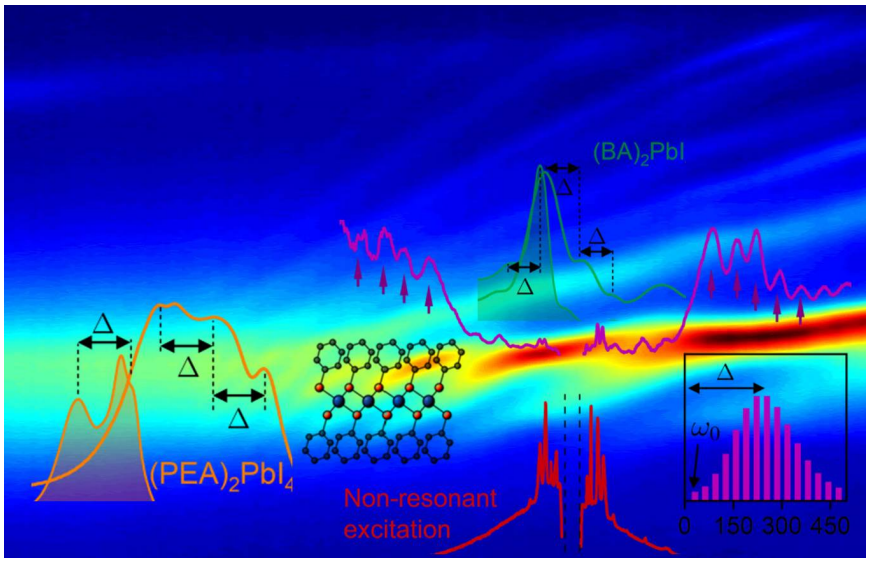

Exciton fine structure in 2D perovskites: The out-of-plane excitonic state

Two-dimensional (2D) lead halide perovskites are a very interesting group of novel semiconducting materials, considered an alternative for applications in photovoltaics and optoelectronics. As a consequence of the quantum and dielectric confinement, the exciton binding energy can reach several hundreds of meV, which results in significant splitting of states of the exciton fine structure. This makes them attractive objects for the investigation of exciton physics, since all excitonic effects are greatly enhanced in this system.

Excitons in 2D lead halide perovskites are composed of electron and a hole with the total angular momentum equal 1/2. This leads to four possible excitonic states, one dark and three bright. Exchange interaction between charges splits off bright states from the dark state. In the case of $(PEA)_2PbI_4$, which is a compound with triclinic crystal structure, due to the low symmetry the degeneracy between the states gets fully lifted, which results in three separated in energy bright states, linearly polarized along the direction of the dipole orientation (see the inset in figure 29).

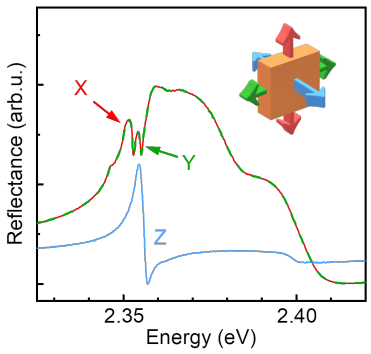

FIG. 29. *Red and green curve representing the reflectance of spectra measured from the plane of the crystal. The blue curve is the reflectance spectrum measured from the edge of the crystal with the polarization along the out-of-plane direction. The inset scheme indicates the orientation of the particular exciton dipole moments with respect to the sample.*

Despite the fact that $(PEA)_2PbI_4$ is one of the most intensely studied representative of 2D lead-halide perovskites, there was no agreement in the scientific community regarding the full fine structure of the exciton, especially when it comes to the states' energetical order. Previous experimental efforts of our group placed the dark, optically inactive state as the lowest energetically, below two bright linearly polarized states X and Y with the dipole moments oriented in the plane of the crystal. However, there was no conclusion about the energy of the remaining bright out of plane oriented Z state with respect to the other states of the fine structure. Different theoretical approaches placed the Z state below or above the X and Y states.

In order to resolve the matter, we have conducted the polarization-resolved micro-reflectance experiments at $T = 4.2\,\mathrm{K}$. We performed the measurements reflecting the linearly polarized light both from the surface and the edge of the sample, probing all three bright states of the exciton fine structure. In the reflectance spectrum measured from the edge of the crystal we observed a strong resonance (blue curve in the figure 29), which we assigned to originate from the out of plane excitonic state. It is located energetically above the features originating from the in plane states and linearly polarized (figure 30) in the direction perpendicular to the crystal plane. By obtaining the information about the final remaining excitonic state, we completed the full fine structure picture, experimentally determining the energies of all states and the values of energy separation between them.

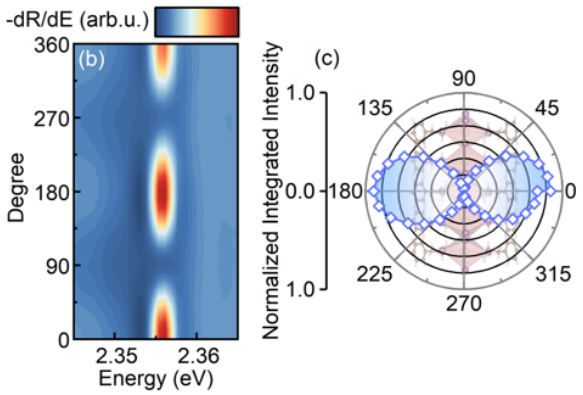

FIG. 30. *Left: Dependence of the negative derivative of the reflectance spectrum from the edge of the sample versus polarization angle. Right: Polar plot of the intensity of the Z state extracted from the negative derivative of the reflectance spectrum. $(PEA)_2PbI_4$ crystal structure is shown to provide a reference for the dipole moment orientation.*

Moreover, our understanding of the detailed bright exciton fine structure, alongside our previous work, allowed us to determine the previously unknown values of the dark and Z exciton g-factors along the c-axis, and therefore the individual g-factors of the electrons and holes. For more details please see [Posmyk *et al.*, Advanced Optical Materials (2023): 2300877].

K. Posmyk, P. Plochocka
M. Baranowski (Wroclaw University of Science and Technology), M. Molas, A. Babinski (Faculty of Physics, University of Warsaw)

Polaronic enhancement of the effective mass in 3D lead halide perovskites

Three-dimensional lead halide perovskites have emerged as one of the most promising and fast-developing classes of materials with a vast array of application possibilities across diverse scientific and technological domains. The success of these materials originates from their semiconducting properties and considerable sunlight-to-energy conversion. This superior characteristic is often attributed to a soft, ionic lattice of the lead halide perovskites that allow numerous physical processes to occur. Among them, one should enumerate rich lattice vibrations and dynamical fluctuation of cage ions, which create complex potential energy surface, very different dielectric constants between the high- and low-frequency regimes which facilitates polaron formation. All these effects strongly depend on temperature and may exert a dramatic impact on the effective mass of carriers. Unfortunately, our understanding of this matter is still limited.

In our work, we used optical spectroscopy combined with magnetic field to dissect the polaronic and temperature effects on the effective mass of carriers in caesium lead bromide ($CsPbBr_3$), methylammonium lead bromide ($MAPbBr_3$) and methylammonium lead iodide ($MAPbI_3$). The measurements were conducted between 2 and 90 K, in the magnetic fields up to 90 T. For all these materials, we could observe the 1s and 2s excitonic states, with additionally well-resolved Landau levels in the reflectivity spectra (figure 31). The Landau levels were observed only in the high-field limit, where lattice deformation cannot follow the cyclotron motion of carriers and, thus, their analysis delivers information on the effective mass of bare carriers (μ_b). This physical quantity was extracted from the field evolution of Landau level transition energies,

$$E_{LL}(n) = E_g + \frac{(n+\frac{1}{2})eB}{\mu_b},$$

where E_g is the band gap energy, and $n = 0, 1, 2, \cdots$ is the orbital quantum number. We find $\mu_b = 0.117\,m_0$, $0.106\,m_0$ and $0.096\,m_0$ for $CsPbBr_3$, $MAPbBr_3$, and $MAPbI_3$, respectively, where m_0 is the free electron mass (figure 31). Crucially, it is not possible to fit the field dependence of the 1s and 2s excitonic transitions employing Makado and McGill's model of the hydrogen atom in a magnetic field with this effective mass value. Application of this simple model results in higher effective mass values, which are equal to $\mu_p = 0.163\,m_0$, $0.151\,m_0$ and $0.102\,m_0$ for $CsPbBr_3$, $MAPbBr_3$, and $MAPbI_3$, respectively. We found that this enhancement originates from polaronic effects in $CsPbBr_3$, $MAPbBr_3$, and $MAPbI_3$, which is consistent with the Bajaj model and the considerable Fröhlich coupling constant value. In addition, we also observed that both the bare and polaronic effective mass increases with increasing temperature in these materials (figure 32). This temperature-induced enhancement is seen in reflectivity spectra as a diminishing blue shift of excitonic resonances in magnetic fields. Notably, the effective mass of carriers increases faster with temperature than the band gap, contradicting the 2-band **k.p** model commonly applied to explain the electronic properties of three-dimensional lead halide perovskites.

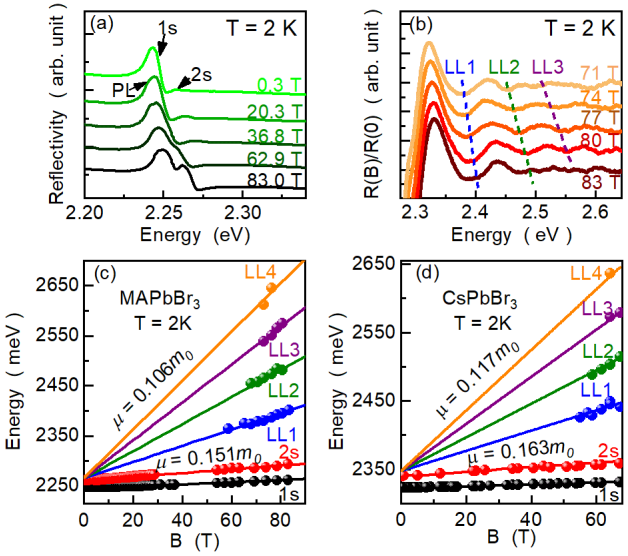

FIG. 31. *(a) Evolution of reflectance spectrum in magnetic field for MaPbBr₃. (b) Landau levels in MAPbBr₃. (c)-(d) Fan charts summarizing 1s, 2s excitonic and interband Landau levels transition energies as a function of the magnetic field for MAPbBr₃ and CsPbBr₃.*

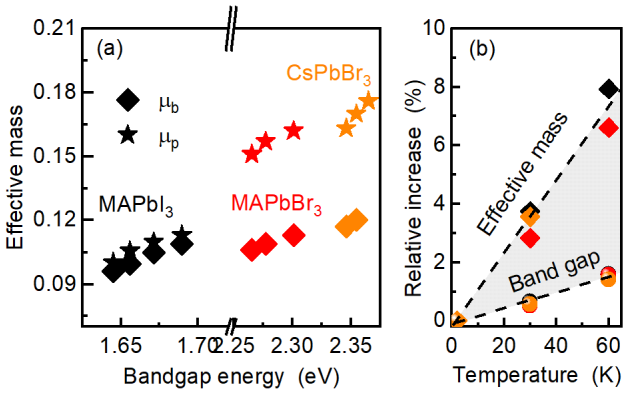

FIG. 32. *(a) The bare (μ_b) and polaronic (μ_p) reduced effective mass for $MAPbI_3$, $MAPbBr_3$ and $CsPbBr_3$ at various temperatures. (b) Temperature-induced relative increase of the band gap and effective mass.*

A. Nowok, P. Plochocka
M. Baranowski, M. Dyksik, A. Surrente (Wroclaw University of Science and Technology)

Magneto-optical properties of functionalized low-dimensional perovskites

Two-dimensional (2D) halide perovskites have recently attracted significant interest due to their unique optical and electronic properties. These materials consist of inorganic layers sandwiched between organic cations, and their structure can be tuned by changing the size and shape of the cations. This gives rise to various interesting phenomena, including quantum confinement, high photoluminescence quantum yields, and exciton binding energy tuning. For these reasons, 2D halide perovskites have shown enormous promise for various optoelectronic applications, including white-light-emitting diodes, and photovoltaics. However, the use of these materials for real device applications requires a thorough understanding of their optical and photophysical properties.

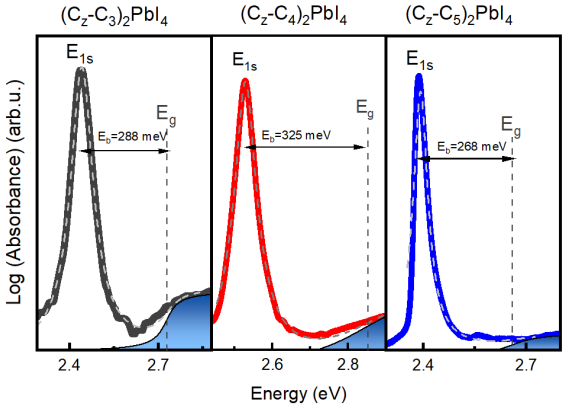

FIG. 33. *Absorption spectra of 2D functionalized perovskites (continuous lines) fitted by 2D Elliott's formula (dashed gray lines).*

Usually in low-dimensional perovskites an electronically inert organic spacer is used, which only has an indirect effect on the electronic structure. Unfortunately, most of the reported 2D perovskites exhibit a high exciton binding energy that limits their potential application in photovoltaics. To overcome this limitation, a viable strategy consists of the incorporation of an electroactive organic cation. This cation is thought to contribute to the electronic properties by introducing frontier orbitals close to the band edge states of the inorganic layer, which significantly improves the absorption efficiency. The optoelectronic properties of these materials are not yet fully investigated.

Here, we compare the diamagnetic shift, exciton binding energy, and band gap of carbazole-alkylammonium (C$_z$-C$_i$, where i is the number of carbon units in the alkyl chain, varying from 3 to 5) to investigate the role of the electroactive C_z molecule on the excitonic properties of the functionalized 2D perovskites. Introducing this electroactive organic cation should have a pronounced effect on the exciton wave-function and therefore on the exciton binding energy. We employ magnetic fields up to 65 T to investigate the excitonic properties of these functionalized 2D perovskites.

The zero-field absorption spectrum of all the investigated compounds measured at 5 K is displayed in figure 33. The spectra display a single excitonic resonance, which we model with a generalized Elliott's formula to extract the 1s exciton transition energy and the onset of the continuum *i.e.* the band gap. The exciton binding energy corresponds to the difference between the energies of the bandgap and the 1s exciton. In these compounds, the exciton binding energy is higher than that of the well-known (PEA)$_2$PbI$_4$.

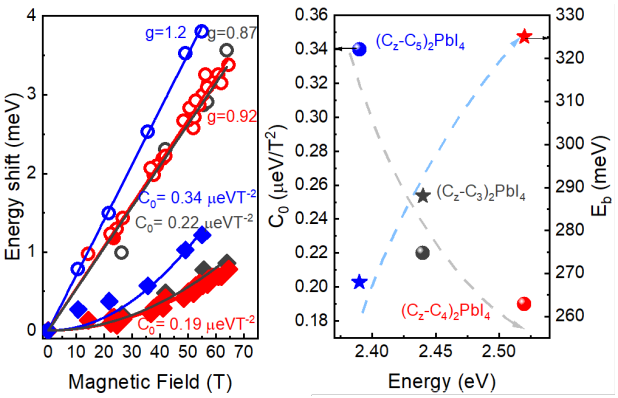

FIG. 34. *Comparison of Zeeman splitting (open circles) and diamagnetic shift (squares) for all compounds at 2 K (left side). Measured diamagnetic coefficients (spheres) and exciton binding energies (stars) as a function of 1s exciton state energy. Symbols correspond to different numbers of carbon atoms in the organic spacer (right side).*

The diamagnetic shift and g-factor were determined for three compounds with different spacers (figure 34). Notably, for samples with electroactive spacer molecules, the diamagnetic shift decreases when the exciton energy increases, while the opposite trend is observed for the binding energy. On the other hand, there seems to be no direct correlation between the length of alkyl chains and the diamagnetic shift. Overall, our results shed light on the fundamental exciton physics of functionalized 2D perovskites and their potential applications in emerging technologies.

P. Peksa, P. Plochocka
M. Dyksik, M. Baranowski, A. Surrente (Wroclaw University of Science and Technology), Y. Boeije, S. Stranks (Cavendish Laboratory, University of Cambridge), W. van Gompel (Hasselt University, Diepenbeek)

Excitons in non-distorted 2D perovskites

Two-dimensional (2D) perovskites are currently under intensive investigation in the semiconductor physics community due to their unique optical and electrical properties. These properties can be easily tuned by rational synthetic design. Importantly, the choice of the organic spacer should not influence the band structure but has a considerable impact on the optical properties of the 2D perovskites by changing the coupling between charge carriers and lattice vibrations. Organic spacers provide control over dielectric confinement, and crystal structure. An interesting case is $(PEA)_2PbI_4$ and $(BA)_2PbI_4$, because presented the same inorganic component but due to the organic cation their distortion of frameworks is different. [Dyksik *et al.*, ACS Energy Lett. **5**, 11 (2020)]. The effective mass of the carriers correlate with octahedral distortions in the perovskite layer since they influence the hybridization between the I p-states and Pb s-states. Therefore, the excitonic properties of these compounds are distinctly different (see figure 35). It has been suggested that the effective mass can be significantly smaller if the octahedral layer is not distorted.

A novel class of benzotriazole-based lead (II) iodide perovskite materials have recently been synthesized. They are characterized by an exceptionally low degree of octahedral tilting [Caiazzo *et al.*, ACS Appl. Energy Mater. **6**, 10 (2023)].

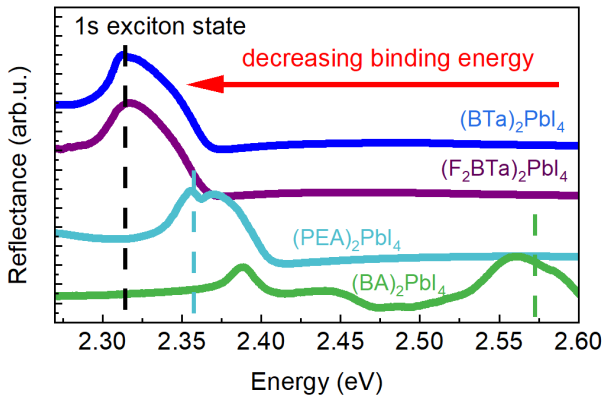

FIG. 35. *Reflection spectra for all compounds. The dashed line indicates the energies corresponding to the 1s excitonic state.*

We compared the excitonic properties of these relatively new compounds with the well-known $(PEA)_2PbI_4$ and $(BA)_2PbI_4$, as shown in figure 35. The dashed line indicates the 1s exciton state for each compound. With the decreasing distortion angle, the red shift of energy can be observed, directly associated with a reduction in exciton binding energy and a reduction in effective mass. To test this hypothesis the BTa (benzotriazole) and F_2BTa (difluorinated benzotriazole) derivative have been measured under high magnetic field up to 85 T. We focus on monitoring the evolution of the 1s excitonic transition (figure 36(a)) in the magnetic field as it provides an alternative route to estimate the effective mass. The total shift of the 1s excitonic transition as a function of the applied magnetic field is given by the diamagnetic shift of the exciton $\delta E \simeq c_0 B^2$.

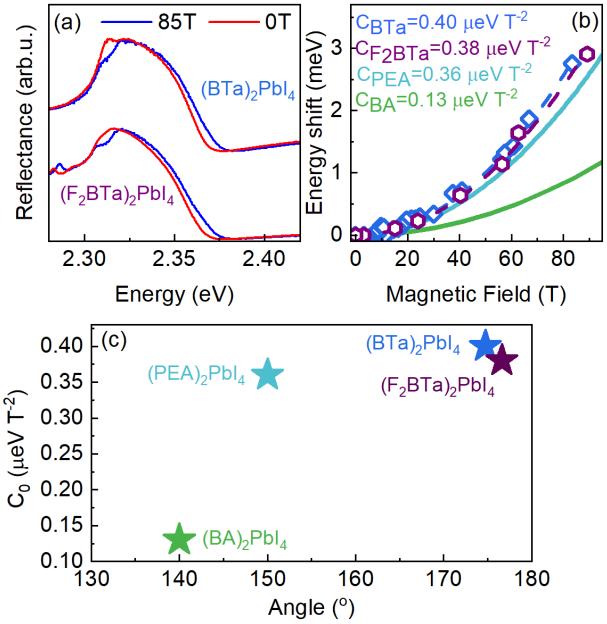

FIG. 36. *(a) Reflectance spectrum at 2K measured at 0 T and 85 T. (b) Energy shift as a function of the magnetic field and the determined diamagnetic shift for both samples. (c) Measured diamagnetic shift as distortions angle.*

From the data shown in figure 36 we determine the diamagnetic coefficient for both samples ($c_0 = 0.40\,\mu eV/T^2$ for $(BTa)_2PbI_4$; $c_0 = 0.38\,\mu eV/T^2$ for $(F_2BTa)_2PbI_4$). The determined diamagnetic shift is higher than for the 2D analogs - $(PEA)_2PbI_4$ and $(BA)_2PbI_4$, as shown in figure 36(c). Since the diamagnetic shift is related to the reduced effective mass, $c_0 \propto 1/\mu^3$ our results suggest that the effective mass for the investigated samples will be smaller than for the compound with a large distortion angle.

Our results demonstrated that the amount of octahedral distortion in the inorganic lattice has a crucial impact on the diamagnetic shift and the carrier effective mass, which is a key parameter defining the performance of any optoelectronic device. Our work provides therefore a different perspective on the utility of the 2D perovskites.

P. Peksa, P. Plochocka
M. Dyksik, M. Baranowski (Wroclaw University of Science and Technology, Wroclaw), A. Maufort, W. van Gompel (Hasselt University, Diepenbeek)

Magneto-optical investigation of the van der Waals semiconductor 2D silver phenylchalcogenolates

2D metal-organic chalcogenides refer to a class of materials that are composed of metal cations, organic ligands, and chalcogenide anions (such as sulfur, selenium, or tellurium) arranged in a two-dimensional structure. However, these materials stand apart from 2D perovskites due to the covalent bonding between organic and inorganic components, providing chemical stability in air and solvents and facilitating electronic bandgap tuning through modification of organic ligands. Out of the reports on 2D metal-organic chalcogenides, particular focus has been directed towards silver phenylselenolate (AgSePh), commonly referred to as "mithrene". AgSePh crystallizes in the form of a 2D semiconductor consisting of stacks of 2D sheets bound together by interlayer van der Waals interactions (inset of figure 37). Each 2D sheet consists of a layer of Ag^+ ions arranged in a distorted hexagonal pattern and sandwiched between two layers of phenylselenolate anions $PhSe^-$, with mostly covalent character to the Ag-Se bond [Lee *et al.*, ACS Nano **16**, 12 (2022)].

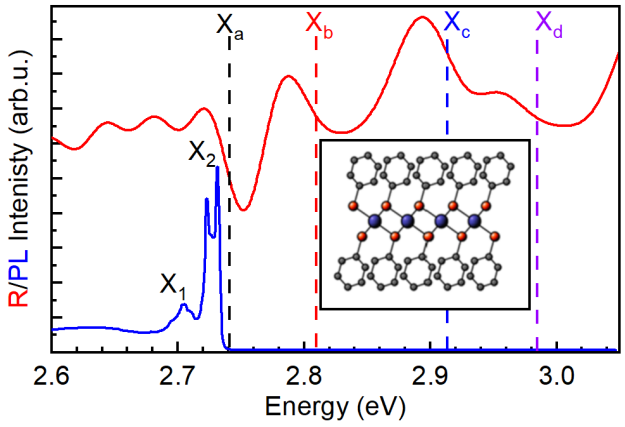

FIG. 37. *Reflectance and μPL of AgSePh at 4 K. Inset - layered 2D structure of silver phenylselenolate (AgSePh).*

In this report, we investigate the AgSePh crystal, which exhibits an interesting optical response, as shown in figure 37. In reflectivity we observe absorption of four states (X_a, X_b, X_c and X_d). In photoluminescence (PL) spectra, two main peaks can be resolved (X_1 and X_2). The X_a state likely corresponds to the states visible in emission with Stokes shift of ~ 10 meV ($E_{X_a} - E_{X_2}$).

We have investigated the polarization properties of the observed absorption resonances. Notably, as shown in figure 38(a) the X_a, X_d states show an orthogonal polarization behaviour to the X_b, X_c states. The separation between all of the four features is similar and approximately 100 meV.

The application of an external magnetic field significantly affects the PL spectra of AgSePh as can be seen in figure 38(b). At high magnetic field (65 T), we can see a splitting of the X_2 state into $X_2^{'}$ and $X_2^{''}$. This behavior indicates a Zeeman splitting (reaching 7 meV). The g-factor of 1.82 was calculated based on the energy difference between $X_2^{'}$ and $X_2^{''}$ as a function of magnetic field (figure 38(c)).

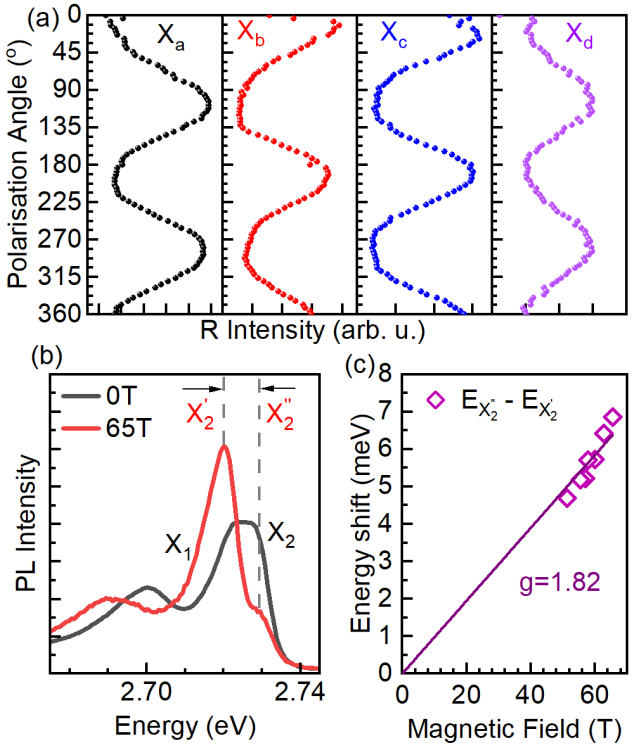

FIG. 38. *[(a) Linear-polarization resolved reflectance intensity for the X_a, X_b, X_c and X_d states. (b) PL spectra at 0 T and 65 T. (c) Calculated g-factor from measured Zeeman splitting.*

The calculated g-factor of 1.82 (figure 38(d)) is significantly larger than that of the well-known 2D perovskites such as $(PEA)_2PbI_4$ for which, the value of g-factor is around 1.2. This signifies a crucial difference in the electronic properties between the two types of 2D materials. 2D silver phenylchalcogenolates require further investigation, including theoretical calculations, in order to determine the effects of their unique structure on the optoelectronic properties of this emerging class of these hybrid 2D semiconductors.

P.Peksa, K. Posmyk, P. Plochocka
M. Dyksik, M. Baranowski (Wroclaw University of Science and Technology), W. S. Lee, W. A. Tisdale (Massachusetts Institute of Technology, Cambridge)

Polaron vibronic progression in 2D Perovskites

2D layered perovskites constitute a rather unique semiconducting material system very different from the well-known family of epitaxial structures. The coexistence of organic and inorganic sublattices within the crystal structure bridges the worlds of *classic* and organic semiconductors. The resulting hybrid material is characterized by a soft and ionic lattice significantly enhancing the coupling of charge carriers to the ions in the lattice. Such a coupling has a pronounced impact on their opto-electronic properties, giving rise to complex absorption and emission spectra.

Typical optical responses of prototypical 2D perovskites, namely $(PEA)_2PbI_4$ and $(BA)_2PbI_4$, are presented in figure 39(a-b), The absorption spectra (solid line) consist of equally-spaced distinct transitions indicated with dashed vertical lines and separated by an energy Δ (black arrows). Associated spectral features, separated by Δ, are also present in photoluminescence (PL) response (shaded curves). A multitude of explanations have been offered in an attempt to rationalize the complex optical spectra, however, none of the proposed interpretations are able to explain the magnitude of the Δ spacing quantitatively.

In this work we show that the formation of polaronic states with their characteristic vibronic progression are responsible for complex line shapes observed in 2D perovskites. Crucially, we explain the magnitude of the Δ spacing by correlating the absorption/PL with the resonant Raman scattering response. The resonant-excitation spectrum, presented in figure 39(c), is unlike any reported to date for 2D layered perovskites – instead of being dominated by low-frequency modes as typically observed for non-resonant excitation (presented in red in figure 39(c)), the maximum intensity is shifted far away from the Rayleigh line to $\simeq 200\,\mathrm{cm}^{-1}$. This new contribution forms an asymmetric comb-like pattern with a tail on the high energy side. The peaks within the comb are equidistant with a period of $\simeq 32\,\mathrm{cm}^{-1}$ determined from a FFT analysis. These properties are simply the well known fingerprint of polarons in organic materials.

The observed high-frequency Raman response (figure 39(c)) shows similarities with the analytical spectral function in the strong coupling regime $\simeq \sum_{p=0}^{\infty} \frac{e^{-S}S^p}{p!}\delta(\omega - p\Delta\omega)]$ which consists of a series of exactly $\Delta\omega$ spaced delta functions at $\omega_0, \omega_1, ...$ The distribution of peak intensities follows a Poisson function with a coupling constant S. The peak intensity reaches a maximum value when the level-index $p \simeq S$. Such a Poisson distribution is depicted in the inset to figure 39(c) by the horizontal purple bars, representing the expected intensity distribution within the Raman response, assuming a large coupling constant $S \simeq 6$. The maximum intensity is shifted by $\simeq \Delta$ from $0\,\mathrm{cm}^{-1}$ and thus the energy Δ is both the spacing between features in absorption/PL, and the maximum of the resonant Raman response for $(PEA)_2PbI_4$. We emphasize that the successive features in the comb-like pattern of the resonant Raman describe the polaron ground state and cannot be attributed to the excited states – they are an inherit part of the polaronic response and form a vibronic-like progression.

For more details please see [Dyksik *et al.*, Adv. Sci. **2**, 2305182, (2023)].

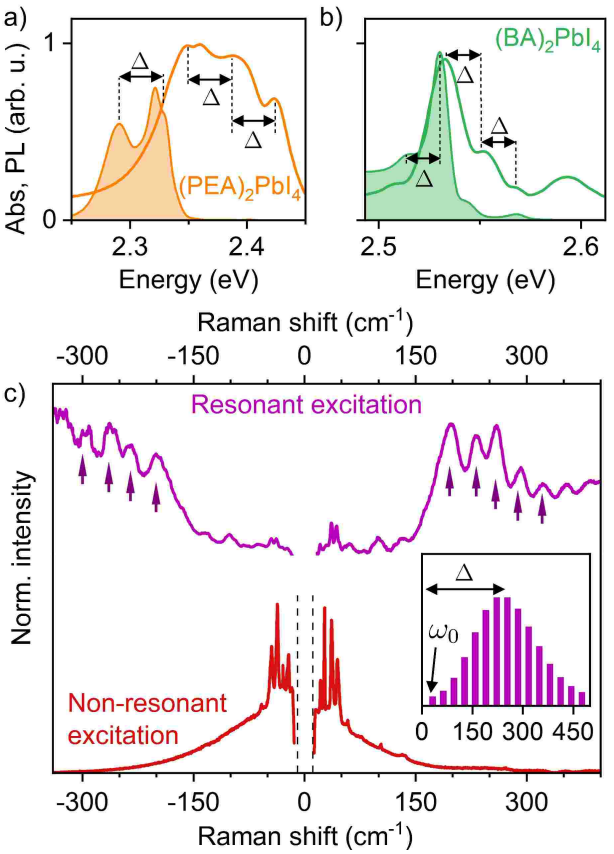

FIG. 39. *Comparison of absorption and PL spectra of (a) $(PEA)_2PbI_4$ and (b) $(BA)_2PbI_4$. Dashed vertical lines indicate the energy of individual optical transitions. The black arrows indicate the Δ energy spacing between the optical transitions. (c) $(PEA)_2PbI_4$ Stokes and anti-Stokes Raman scattering results for resonant (2.6 eV) and non-resonant (2.18 eV) excitation condition. Purple arrows indicate the equidistant signals building up the polaron vibronic progression. The inset shows the polaron's energy diagram. ω_0 is the first component in the polaron vibronic progression. Δ denotes the approximate position of the maximum of the Raman response.*

K. Posmyk, D. K. Maude, P. Plochocka
M. Dyksik, M. Baranowski (Wroclaw University of Science and Technology), H. Duim, S. Adjokatse, M. A. Loi (University of Groningen), D. Beret, S. Moyano, P. Puech (CEMES-CNRS, Toulouse), A. Mlayah (LAAS-CNRS, Toulouse)

Temperature dependence of the band gap in $ZrTe_5$ - implications for the topological phase

Zirconium pentatelluride ($ZrTe_5$) is a narrow-gap system widely explored in the past, often in the context of so-called resistivity anomaly. More recently, theoretical studies of $ZrTe_5$ that were primarily focused on topological properties induced a renewed interest in this system. In particular, the $ZrTe_5$ monolayer was proposed to be a large-gap quantum spin Hall insulator. Over the past few years, a number of experiments has been performed on bulk and thin layers of $ZrTe_5$ and expanded our knowledge about this material considerably. The experimentally observed phenomena in $ZrTe_5$ comprise the magneto-chiral effect, the giant planar Hall effect , the quasi-quantized quantum Hall effect, pressure-induced superconductivity, or optical conductivity that is linear in photon energy.

This series of important experimental observations contrasts with our current understanding of low-energy excitations in $ZrTe_5$. In fact, no consensus has been so far established whether the electronic bands in bulk $ZrTe_5$ have normal or inverted ordering, *i.e.*, whether this material is a strong or weak topological insulator (STI or WTI). Ab initio calculations favor the STI phase, but their prediction force may be limited in a system close to the topological phase transition. Experimentally, both STI and WTI phases have been reported, based on transport, ARPES and optical data.

Theoretical studies suggest that bulk $ZrTe_5$ is a system close to a topological phase transition, which may be the reason why no consensus about the topological nature of $ZrTe_5$ has so far been achieved [Fan *et al.*, Sci. Rep. **7**, 45667 (2017)]. Theoretically, only a relatively small increase in the unit-cell volume is sufficient to bring $ZrTe_5$ from the STI to WTI regime, *i.e.*, from the inverted to the normal ordering of bands at the center of the Brillouin zone. Importantly, the band gap always closes and re-opens during such a topological phase transition.

Experimentally, it was shown that the unit-cell volume in $ZrTe_5$ increases monotonously with temperature [Fjellvag *et al.*, Solid State Commun. **60**, 91 (1986)]. Thanks to this, the temperature dependence of the band gap was proposed to be an unambiguous signature of the topological phase in $ZrTe_5$. In the STI regime, the band gap is first supposed to shrink with increasing T, then close completely, and finally, re-open in the WTI regime. In contrast, a monotonous increase of the band gap with temperature is expected in the WTI regime. Only the latter scenario is consistent with our data, thus implying the WTI phase in $ZrTe_5$. Let us note that the volume of the unit cell changes considerably in the explored range of temperatures, approximately by 0.5%.

We have performed a series of Landau level spectroscopy measurements on $ZrTe_5$ at various temperatures to precisely determine the width of its band gap as a function of temperature, and therefore to test the topological phase of this material. Figure 40, shows the values of the band gap, deduced from the THz/infrared magneto-reflectivity measurements. We find that the gap is non-zero at low temperatures, $E_g = (5 \pm 1)$ meV at $T = 5$ K, and it increases with T monotonously, up to almost 20 meV at $T = 150$ K. Comparing these results with the theoretical calculations, such behaviour is consistent with $ZrTe_5$ being a weak topological insulator.

Further, performing *in situ* resistivity measurements, we have shown that the resistive anomaly of $ZrTe_5$ is not directly connected to the change in the band gap, as suggested in several previous studies. As shown in figure 40, there is no significant change in the width of the band gap at temperature $T = 75$ K, corresponding to the maximum of the resistivity.

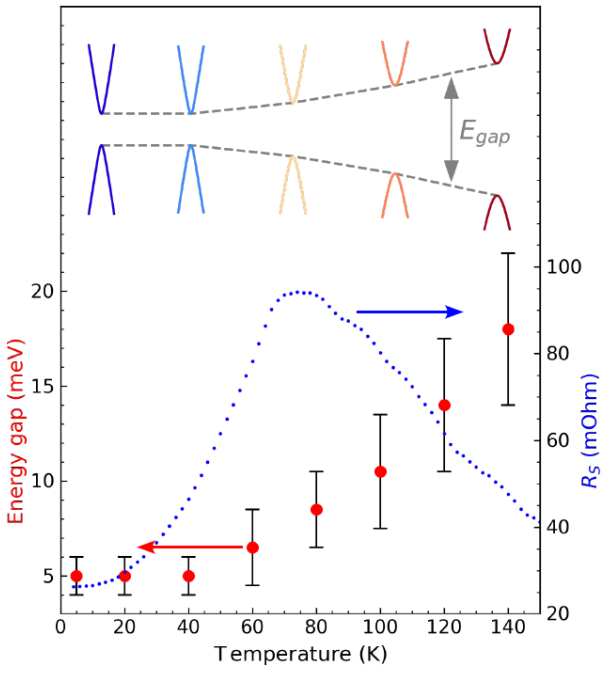

FIG. 40. *The experimentally determined band gap of $ZrTe_5$ at various temperatures. The resistance versus temperature shows an anomaly with a maximum at $T = 75$ K measured on the first cooling down. Insert - schematic visualization of the band gap opening with increasing temperature.*

I. Mohelsky, J. Wyzula, B. A. Piot, M. Orlita
A. Akrap (University of Fribourg), G. D. Gu, Q. Li (Brookhaven National Laboratory, New York)

Magneto-photoluminescence of CdTe quantum wells

We compare a low-temperature photoluminescence (PL) from two samples with CdTe quantum wells (QWs) and $Cd_{0.7}Mg_{0.3}Te$ barriers. We have inevstigated a single quantum well sample (SQW) and a multiple quantum well sample (MQW) with ten QWs. All QWs are 20 nm wide and modulation-doped with iodine donors. The samples were cooled to 4.2 K and results were obtained in magnetic field up to 9 T. PL maps for both samples in σ^- polarization are shown in figure 41.

We analyzed the position and intensity of the oscillations in the PL as a function of magnetic field. For the SQW, the PL originates from the recombination of free electrons with free holes while in the case of the MQW, the holes are localized. A crucial factor allowing us to find out this difference was determination of the cyclotron free electron mass in these samples which was achieved by carrying out Fourier spectroscopy. We have found $(0.1112 \pm 0.0003)m_0$ and $(0.1094 \pm 0.0003)m_0$ for SQW and MQW samples, respectively.

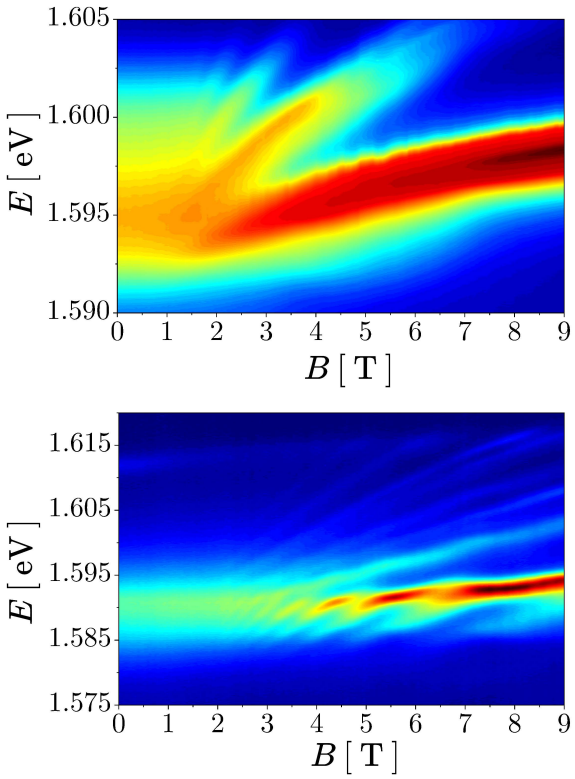

FIG. 41. *A false-color photoluminescence map for SQW (upper panel) and MQW (lower panel) samples measured in σ^- polarization. PL intensity is presented on a logarithmic scale.*

Photoluminescence spectra of SQW and MQW samples are quite different. In the first case, we observe the main peak split into Landau levels and PL spectra cover approximately the range from 1.592 to 1.605 eV. In the case of MQW, the spectral range of PL is broader - from about 1.58 eV to 1.615 eV. A difference in the lower bound is caused by Landau-like maxima which are visible in the low-energy part of the MQW PL and which are interpreted as phonon replicas. Raman spectroscopy carried out at room temperature on the MQW sample shows phonons with an energy which support the interpretation of phonon replicas, however, a softening of phonon modes with respect to bulk CdTe was observed and attributed to disorder.

A substantial difference between the two samples is the width of the spacer (20 nm in SQW versus 10 nm in MQW) with the same doping level. A resulting higher concentration n_c in MQW sample leads to a broader PL spectrum and clearly visible luminescence from the second electrical subband. This means that the Fermi level is close to the second electrical subband in the MQW sample. A rough estimate of $E_F \simeq 26$ meV, based on the spectrum at $B = 0$, gives the electron concentration $n_c = m_e E_F/\pi\hbar^2 = 1.2 \times 10^{12}$ cm^{-2} which is comparable to 1.0×10^{12} cm^{-2} determined from transport measurements. On the other hand, signatures of the second electrical subband is barely visible in PL for the SQW sample.

In conclusion, we carried out photoluminescence measurements on modulation-doped CdTe quantum wells with $Cd_{0.7}Mg_{0.3}Te$ barriers. Two samples were studied, one with ten QWs and the other with a single QW. An analysis of the intensity of PL as a function of B shows a qualitative agreement of data with a model based on Landau quantization of hole and electron levels in the case of the single QW. In the case of the MQW sample, the hole is localized and the evolution of its quantum levels does not follow Landau quantization. Essential differences in PL spectra were observed between the two samples. Interpretation of data should take into account mixing of heavy and light holes in the valence band of quantum wells, the influence of a built-in electric field, and also the possible influence of fluctuations of the electrostatic potential resulting from random distribution of impurities. In particular, these fluctuations could lead to a softening of LO phonon mode necessary to explain phonon replicas in the photoluminescence of the multiple quantum well sample.

For more details please see [Solarska *et al.*, ACS Omega, **8**, 40801 (2023)].

F. Le Mardele, I. Mohelsky, M. Orlita
W. Solarska, K. Karpierz, M. Zaremba, A. Siemaszko, M. Grymuza, L. Kipczak, N. Zawadzka, M. Molas, E. Imos, A. Babinski, J. Lusakowski (Faculty of Physics, University of Warsaw), Z. Adamus, T. Slupinski, T. Wojtowicz (Institute of Physics, Warsaw)

Three-layer InAs/GaInSb quantum-well spin-Hall insulator

The quantum spin Hall insulator is a state of matter characterized by an insulating bulk and spin-polarized gapless helical states at the sample edges. The presence of these edge states is of great interest for potential applications in spintronics, metrology and quantum information.

So far, the quantum spin Hall insulator state was experimentally established in a few semiconducting systems, for example in HgTe quantum wells (QW) and InAs/GaSb QW bilayers. It was also observed in 1T-WTe_2 monolayers. The latter show a 45 meV inverted band gap demonstrating a stable quantum spin Hall insulator state up to 100 K. Nevertheless, the observation of quantum spin Hall insulator in monolayer systems remains extremely challenging due to structural or chemical instabilities. Our work is driven by the search of high-temperature quantum spin Hall insulators with large inverted band gaps among QW heterostructures.

The maximum inverted band gap achieved in classical tensile-strained HgTe QWs grown on CdTe does not exceed 16 meV, but can reach 55 meV in compressively-strained HgTe QWs. Quantum spin Hall insulators based on InAs/GaSb QW bilayers have a considerable advantage over HgTe QWs because of their ease of fabrication. The subband inversion in InAs/GaSb bilayer QWs is caused by the specific band-edge alignment of InAs and GaSb arising at their interface. For thin enough InAs and GaSb layers, the energy of the first electronic subband minimum E_1 lies above the hole-like H_1 level, and the QW has a trivial band ordering.

With increasing layer thickness, a band inversion may arise, in which the E_1 subband becomes lower than the H_1 subband. However, their small inverted band gap of about 3-4 meV induces a large residual bulk conductance. Removing the structure inversion asymmetry inherent to InAs/GaSb QW bilayers by adding a second InAs layer significantly enhances the inverted bandgap energy, resulting in a quantum spin Hall insulator with the bulk gap comparable with that of inverted HgTe QW.

A typical signature of the inverted-band ordering under quantizing magnetic field is the crossing above a critical magnetic field B_c of a particular pair of Landau levels, called zero-mode Landau levels. These modes originate from the lowest conduction and upper valence subbands. The former has a heavy-hole-like character while the latter has an electron-like character. When the magnetic field increases, the band structure remains inverted up to B_c above which the system is driven into a trivial band ordering.

Figure 42 shows our preliminary magneto-transport investigations of a 3-layer ($InAs/Ga_{0.65}In_{0.35}Sb/InAs$) QW for which the inverted gap is estimated to be around 30 meV. When the Fermi energy lies in the gap, a pronounced minimum of ρ_{xx} is observed at $B_c \simeq 30$ T, corresponding to the crossing of the zero-mode Landau levels.

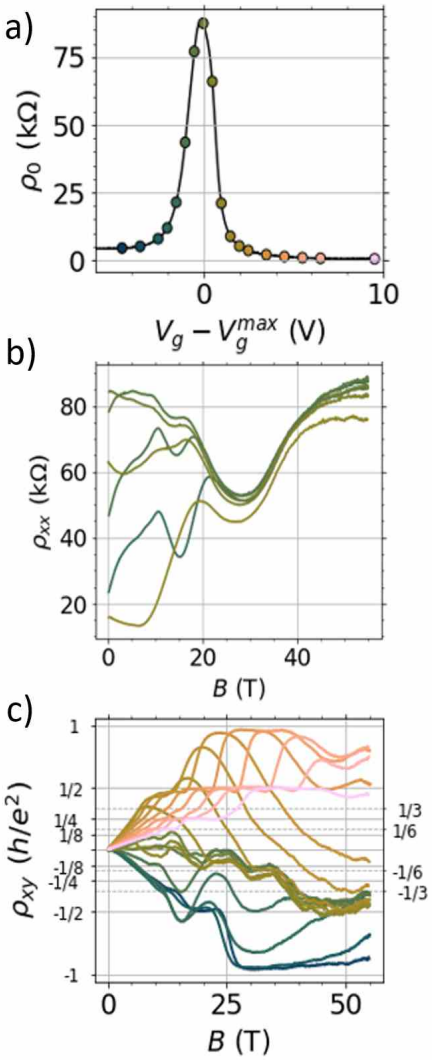

FIG. 42. *Gate voltage (a) and magnetic field dependencies of the longitudinal (b) and transverse (c) resistivities for a 3-layer ($InAs/10ML\text{-}Ga_{0.65}In_{0.35}Sb/InAs$) QW at $T = 4.2$ K. (a) The resistance at zero magnetic field increases when the Fermi energy lies in the inverted gap. When the Fermi level is in the valence or the conduction band, Shubnikov de Haas oscillations of ρ_{xx} are observed (b), as well as clear quantized Hall plateaus in ρ_{xy} (c). (b) At $B \simeq 30$ T, a pronounced resistivity dip is observed, whatever the gate voltage, indicating the closure of the gap.*

M. Pierre, M. Leroux, W. Escoffier, M. Goiran
C. Avogadri, S. Benlemqwanssa, B. Jouault (L2C-CNRS, University of Montpellier)

Metals, Superconductors and Strongly Correlated Systems

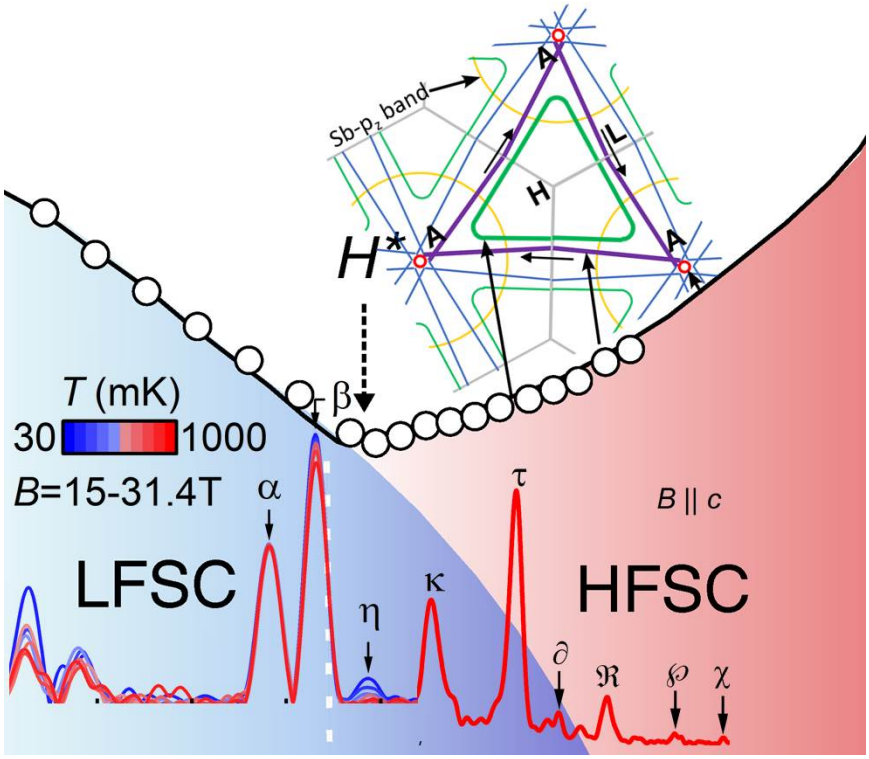

Double-peak structure of quantum oscillations in the specific heat of semi-metallic graphite

Quantum oscillation phenomenon are widely used to understand the electronic structure of quantum matter. Here we investigate quantum oscillations in the electronic specific heat $C_{\rm el}$ in natural graphite. At higher temperatures, the crossing of a single spin Landau level and the Fermi energy give rise to a double-peak structure (figure 43).

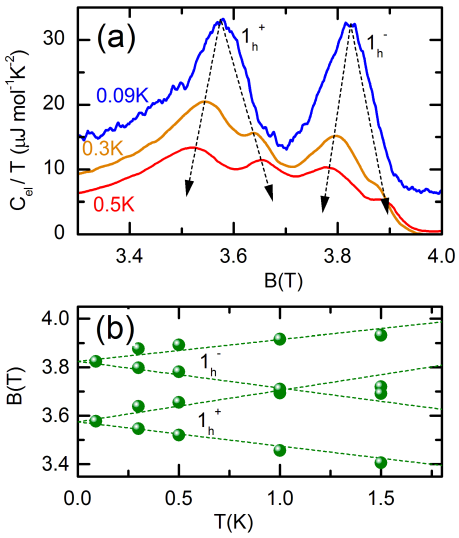

FIG. 43. *(a) Electronic specific heat divided by temperature C_{el}/T in graphite as a function of B where the $1_h^{\pm}$ Landau levels cross the Fermi energy. (b) Magnetic field position of the double-peak structure as a function of temperature.*

Crucially, such a double peak is not observed in other thermodynamic probes, *e.g.* magneto-transport or the magneto-calorific effect. The hole and electron spin Landau levels involved are identified by numerically diagonalizing the SWM Hamiltonian which describes the band-structure of graphite in a magnetic field. At lower temperatures, the splitting decreases, and the double-peak structure eventually merges into a single peak at $T \simeq 90\,\mathrm{mK}$ (figure 43).

Intriguingly, the double-peak structure is predicted by text book theory,

$$C_{\rm el}/T = k_B^2 \int_{-\infty}^{\infty} D(E) \left(-x^2 \frac{dF(x)}{dx}\right) dx,$$

where $F(x) = 1/(1+e^x)$, $x = E/k_BT$ and k_B is the Boltzmann constant. The specific heat depends on the convolution of the Landau level DOS $D(E)$ and a kernel term $-x^2 dF(x)/dx$ which involves the first derivative of the Fermi-Dirac distribution function. The usual approximation, removing $D(E)$ from the integral to obtain the well know formula $C_{\rm el} = \frac{1}{3}\pi D(E_F) k_B^2 T$, actually suppresses the double-peak structure in $C_{\rm el}/T$, which originates from the temperature dependent splitting of the double maxima in the kernel term $-x^2 dF(x)/dx$ (when plotted versus $E = xk_BT$ as in figure 44). The calculated and predicted $C_{\rm el}/T$ in figure 44 are in excellent agreement, notably they reveal the highly asymmetric DOS of 3D Landau levels due to the van Hove singularity.

Therefore, the kernel term represents a spectroscopic tuning fork of width $4.8k_BT$ which can be tuned at will to resonance. Using a coincidence method, the double-peak structure in specific heat can be used to accurately determine the Landé g-factors of quantum materials. More generally, the tuning fork can be used to reveal any peak in the fermionic density of states which crosses the Fermi energy, such as for example Lifshitz transitions in heavy-fermion compounds.

For more details please see [Yang et al., Nature Communications **14**, 7006 (2023)].

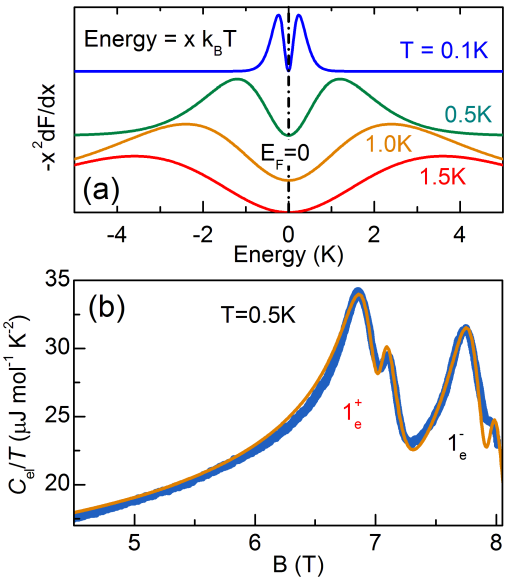

FIG. 44. *(a) The kernel term $-x^2 dF(x)/dx$ plotted versus $E = xk_BT$. Maxima occur at $x = \pm 2.4$ (b) Measured (blue) and calculated (orange) electronic specific heat C_{el}/T in graphite close to where the $1_e^{\pm}$ electron Landau levels cross the Fermi energy at $T = 0.5\,K$.*

D.K. Maude
Z. Yang, Y. Kohama, T. Nomura, T. Shitaokoshi (ISSP, University of Tokyo), B. Fauqué (Collège de France-CNRS, Paris), S. Kim, D. Chowdhury (Cornell University, Ithaca), Z. Pribulová, J. Kačmarčík (Slovak Academy of Sciences, Košice), D. Aoki (Tohoku University, Ibaraki), A. Pourret, T. Klein, C. Marcenat (CEA, IRIG, Pheliqs, Grenoble)

Influence of the anion substitution on electronic correlations in κ-(BEDT-TTF)$_2$X near the Mott metal-insulator transition

The layered organic conductors κ-(BEDT-TTF)$_2$X have been extensively employed for studying the bandwidth-controlled Mott metal-insulator transition (MIT) and multiple related fascinating phenomena. In these materials one can easily tune the ground state by applying a moderate pressure or tiny chemical modifications. For example, the salt with anion X = Cu[N(CN)$_2$]Cl (hereafter κ-Cl) is an archetypal quasi-2D antiferromagnetic Mott insulator at low temperatures but becomes metallic under a pressure of just 0.4 kbar. At the same time, the κ-Br salt, which differs from κ-Cl by a single atom Br replacing Cl in the complex anion, is metallic already at ambient pressure. The anion replacement is widely believed to act similarly to pressure, predominantly changing the ratio U/t (U is the onsite Coulomb repulsion and t the effective transfer integral) and therefore called "chemical pressure". This interpretation was supported by optical conductivity studies of "mixed" salts κ-Br$_x$Cl$_{1-x}$ [Merino *et al.*, Phys. Rev. Lett. **100**, 086404 (2008)] reporting a strong, 3-fold increase of the quasiparticle effective mass, caused by increasing U/t, upon a small reduction of Br content. On the other hand, our comparative studies of Shubnikov-de Haas (SdH) oscillations in pressurized κ-Cl and another κ salt, with X = Cu(NCS)$_2$ [Oberbauer *et al.*, Phys. Rev. B **107**, 075139 (2023)] showed nearly identical effective masses. Since κ-NCS is even more metallic than κ-Br, this result casts doubt on the chemical pressure scenario. To clarify the situation, we have carried out simultaneous measurements of the SdH oscillations in two selected κ-Cl and κ-Br crystals under pressure.

Examples of the SdH oscillations in both samples are shown in figure 45(a). The P-dependent effective cyclotron masses evaluated from the T-dependence of the SdH amplitude are plotted versus pressure in figure 45(b). One immediately sees that at all pressures the masses in κ-Br and κ-Cl are quite similar to each other, in stark contrast to what was found in the optical studies. We note that optical properties can be sensitive to spurious surface effects, whereas SdH oscillations probe the bulk properties and hence are more relevant.

At lowest pressures, $P < 0.4$ kbar, where κ-Cl is in the metal/insulator phase-coexistence state, its effective mass $m_c^{\rm Cl}$ is notably, $10-20\%$, higher than for the fully metallic κ-Br salt. This difference is likely a manifestation of recently proposed heavy "resilient" quasiparticles in thick domain walls emerging in the phase-coexistence region. Right outside this range the difference between the masses rapidly drops, however remains positive, $\Delta m_c \equiv m_c^{\rm Cl} - m_c^{\rm Br} \approx 0.1 m_0$. We attribute it to a weak "chemical pressure" equivalent to $P \simeq 100$ bar.

At $P \sim 3$ kbar, Δm_c virtually vanishes. One might explain this by vanishing electronic correlations in both compounds and saturation of the m_c at the level of the one-electron band mass. However, the $m_c(P)$ dependence does not saturate, showing a significant negative slope at $P > 3$ kbar. Moreover, at 6 kbar $m_c^{\rm Cl}$ becomes smaller than $m_c^{\rm Br}$. The difference, $|\Delta m_c| \approx 0.2 m_0$, though small, exceeds the error bar of our evaluation. If it originates from the difference in the band masses of the two salts, it increases our estimation of "chemical pressure" at the border of the MIT, to an equivalent of 0.7 kbar. One should, however, not disregard a possibility that the two salts have slightly different compressibilities, which would influence $m_c(P)$. Further studies are needed for clarifying this question.

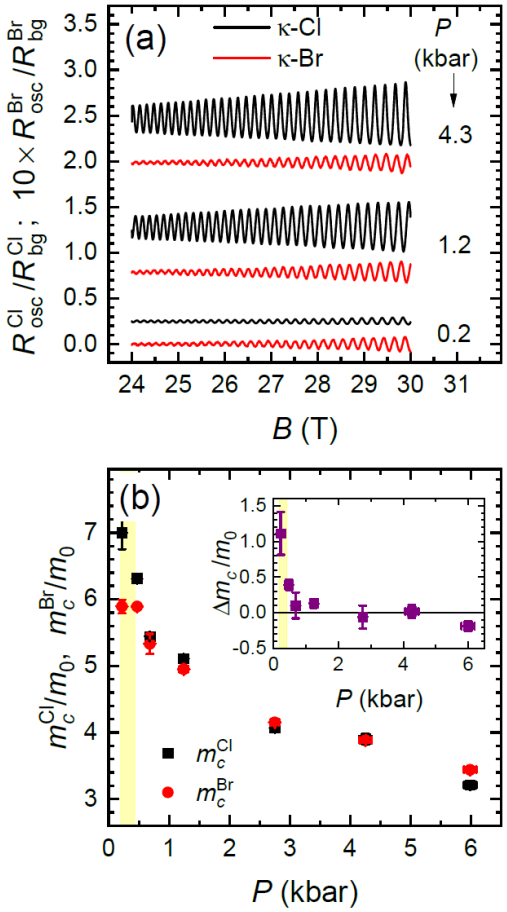

FIG. 45. *(a) Examples of SdH oscillations (normalized to the background resistance) in κ-Cl and κ-Br at different pressures, $T = 0.5$ K. The curves are vertically shifted for clarity. (b) P-dependent effective masses of κ-Cl and κ-Br (main panel) and their difference, $\Delta m_c \equiv m_c^{Cl} - m_c^{Br}$, (inset) in units of the free electron mass. Yellow rectangle: the phase coexistence range for κ-Cl at the 1st-order MIT.*

I. Sheikin
S. Erkenov, W. Biberacher, M. Kartsovnik (Walther-Meissner-Institute, Garching)

Exchange gap in GdPtBi probed by magneto-optics

Half-Heusler compounds are a family of ternary cubic crystals that provide a large variability in their band structures and hence in their material properties. These materials can host inverted band gaps, leading to topologically non-trivial electronic states. In our study we focused on GdPtBi – a magnetic half-Heusler material with a semimetallic electronic structure and an antiferromagnetic phase below the Néel temperature, $T_N = 9\,K$. In this and related compounds, the band inversion gives rise to a peculiar type of band intersections called the triple points near the Γ point. When GdPtBi is subjected to a magnetic field, the Γ_8 bands are believed to substantially split in a Zeeman-like fashion, with large effective g factors mediated by the exchange interaction. The splitting of the triple points in fields gives rise to Weyl points, which positions depend on the field strength.

This magnetically tunable Weyl state in GdPtBi has attracted quite a lot of attention. Due to the inaccessibility of ARPES in magnetic fields, other experimental means are required to investigate the exchange-split band structure of GdPtBi. Currently, electrical and thermal magnetotransport measurements are available. Magneto-optical studies offer another route for such investigations, but were at that stage still missing. In our study, we amended this shortage. Our findings provide strong and independent experimental evidence for the large effective Zeeman splitting in GdPtBi.

The experimental results are presented in figure 46(a) as a stacked plot of the relative reflectivity, R_B/R_0, in 1 T steps. The spectra are dominated by two broad peaks, emerging with magnetic field: a low-frequency peak below 10 meV and a broad, less intense maximum, which shifts to higher frequencies as B increases. This feature is marked by the transparent orange overlay in the figure. Other smaller visible features include two phonons at around 14.5 and 18 meV and an artifact at 45 meV, which appears due to the merger of two spectral ranges in our measurements. By looking at the raw spectra, one can immediately note that they are uncharacteristic for inter-Landau-level transitions, which typically manifest themselves as a rich series of rather narrow absorption lines in R_B/R_0 ("Landau fans"). The inter-Landau-level transitions in GdPtBi are likely weak and not resolved in our measurements.

Upon application of a magnetic field, the band structure of GdPtBi strongly changes. The spin-nondegenerate bands near the Γ point start to diverge in energy in a Zeeman-like fashion due to the exchange interaction. In our study, we demonstrated that the two broad features in the experimental R_B/R_0 spectra can be reproduced well by a parabolic model Hamiltonian containing Zeeman terms.

The relative reflectivity spectra calculated from the model are shown in figure 46(b). The calculations are made in a common way, using the Kubo formula and the standard optical formulas for reflectivity. The

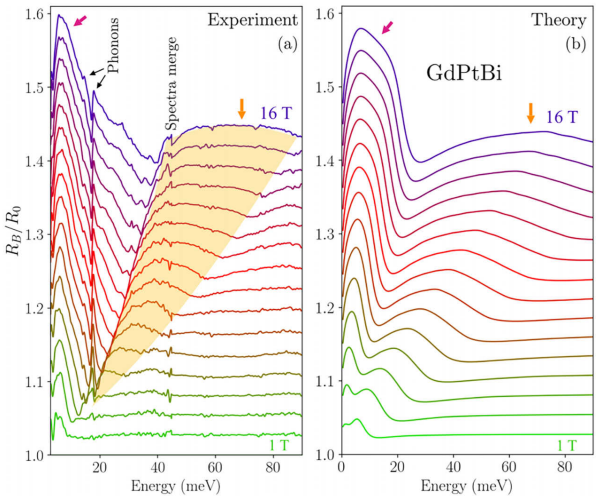

FIG. 46. *(a) Relative magneto-reflectivity spectra of GdPtBi measured from the (111) plane at $T = 4.2\,K$ and various magnetic fields from 1 to 16 T. (b) Spectra of the same type, calculated from the four-band model Hamiltonian. The colored arrows indicate the major spectral features, showing a good match between theory and experiment.*

cyclotron-resonance contribution is also included in figure 46(b). As one can see from the figure, our model can qualitatively reproduce the two major features of the experimental R_B/R_0 spectra and their B-field evolution: the low-frequency peak grows in intensity with increasing B and remains roughly at a fixed frequency; the second peak shifts to higher frequency and broadens with field, centered around 70 meV at 16 T. Furthermore, the heights of both peaks in the calculated spectra are well comparable to the experiment.

Our model yields a large effective g factor, $g^* = 95$. Such large values of g^* have been anticipated for GdPtBi but not detected experimentally until now. Note that g^* expresses, in simple terms, the energy shift of the exchange-split bands as B increases. From the DFT calculations, one can also extract an estimate for the g factor, which is $g^* \approx 92$, in good agreement with our model.

For more details please see [Polatkan *et al.*, Phys. Rev. B **108**, L201201 (2023)].

I. Mohelsky, J. Wyzula, M. Orlita
S. Polatkan, E. Uykur, M. Dressel, A. V. Pronin (Universität Stuttgart), C. Shekhar, C. Felser (MPI CPfS Dresden)

Magneto-optical response of the Weyl semimetal NbAs - experimental results and hyperbolic-band computations

At present, the family of transition metal monopnictides (TaAs, TaP, NbAs, and NbP) is likely the best-known and experimentally most explored class of Weyl semimetals (WSMs). In these nonmagnetic materials, which lack space inversion, a type-I WSM state is realized. According to band-structure calculations, the Brillouin zone of these compounds possesses 24 Weyl nodes, which can be divided in two groups, commonly dubbed as W1 (8 nodes) and W2 (16 nodes). *Ab initio* calculations predict that the Weyl nodes are situated either slightly below or slightly above the Fermi level, giving rise to conical Weyl bands. This rather complex low-energy band structure often obscures observation of the effects, related to the chiral carriers.

In our recent study [Polatkan *et al.*, Phys. Rev. B **108**, L241201 (2023)], we concentrate on one compound from the TaAs family – NbAs – and study its Landau-level spectrum in the applied external magnetic field in the Faraday geometry. Magneto-optical Landau-level spectroscopy in the far-infrared region is a well-established tool for experimental studies of topological materials. We motivate our study by attempting to consistently describe the major features of the magneto-optical response within a single effective Hamiltonian, which grasps the essence of the band structure.

To describe the experimentally observed spectrum of the inter-Landau-level transitions in NbAs, we have constructed a model Hamiltonian. Effectively, it is a two-dimensional Dirac Hamiltonian with hyperbolic non-degenerate bands. Importantly, the intensity of the inter-Landau-level transitions in three-dimensional bands heavily depends on the out-of-plane velocity v_z. This parameter differs by an order of magnitude for the bands near the W1 and W2 nodes in NaAs: $v_z(\mathrm{W1}) \simeq 10^4$ m/s and $v_z(\mathrm{W2}) \simeq 10^5$ m/s. With the difference in the density of states, different line intensities are to be expected. Transitions near the W1 cones should dominate over the contributions of the W2 bands.

In figure 47, we plot the calculated relative reflectivity, R_B/R_0, obtained from the quantized version of our Hamiltonian together with the experimentally observed transitions shown as dotted lines. The interband optical conductivity was calculated using the Kubo formula. From the conductivity, the relative reflectivity was calculated utilizing the standard optical formulas. As one can see from the figure, the model description of the observed transition lines is very good. Only one experimentally observed line (the high-frequency blurred violet line) does not fit within the model, but it is obvious that this line cannot belong to the same fan of inter-Landau-level transitions as all other lines. This violet line is likely related to gapped bands, as was discussed in the previous studies. The additional line appearing in the calculations in-between the two experimentally detected sets (*i.e.*, the red and magenta lines) is likely invisible in the experiment because of the large noise at the relevant frequencies.

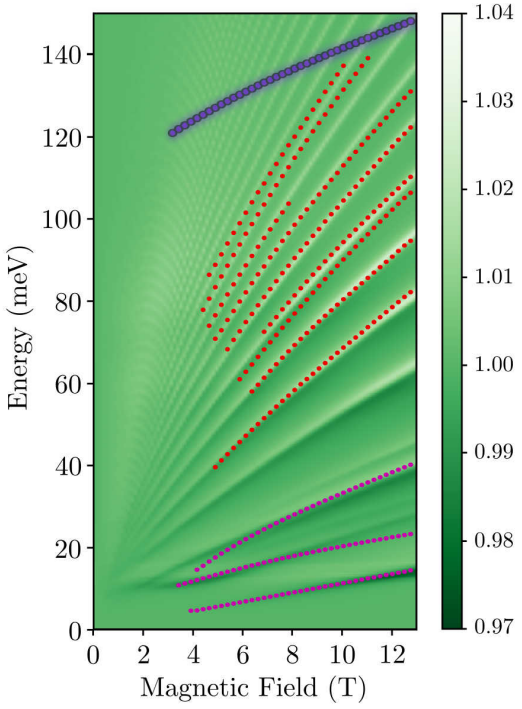

FIG. 47. *False-color plot of the relative magneto-reflectivity, R_B/R_0, obtained from the model Hamiltonian and experimentally observed transitions extracted from the experimental data and shown as dotted lines.*

Summarizing, our results on Landau-level optical spectroscopy demonstrate that the magneto-optical spectra of the Weyl semimetal NbAs at low energies (5 – 150 meV) cannot be reduced to such simple approximations, as a linear or parabolic-band response (or a sum of such responses). Instead, the spectra are dominated by the transitions within the crossing hyperbolic bands, which form the W1 Weyl cones. The chiral Weyl bands themselves are not visible, as they have a very small energy scale. Still, taking into account the accurate band structure near the W1 nodes is essential for the proper description of the observed magneto-optical features. The chiral W2 bands, in turn, do not provide detectable contributions due to the low density of states in these bands.

J. Wyzula, M. Orlita
S. Polatkan, E. Uykur, M. Dressel, A. V. Pronin (Universität Stuttgart), C. Shekhar, C. Felser (MPI CPfS Dresden)

Evidence of 3D Dirac conical bands in TlBiSSe by optical and magneto-optical spectroscopy

A three-dimensional Dirac semimetal is characterized by a doubly degenerate cone in which the nodal point crosses only at the time-reversal invariant momenta (Kramers degeneracy). The linear dispersion of those bands has allowed a bridge between particle physics and condensed matter physics, in which the quasi-particle will be described by the Dirac equations and carry relativistic-like properties. To access those effects in the matter, the chemical potential has to sit at the nodal point, or rather close to probe interband transitions in the cone. The theoretical descriptions have drawn two main hallmarks which will be a linear dispersion of the optical conductivity and a square root dependency in the quantification of the Landau level energy. The realization of a material that exhibits both responses is missing in the literature. The principal reasons are often a conical dispersion sitting around other bands, a Fermi level far away from the nodal point, or a conical dispersion only in two dimensions.

We report an optical and magneto-optical spectroscopy study on the material TlBiSSe which is a rare case of a 3D Dirac semimetal realisation. TlBiSSe possesses a linear dispersion at the Γ point, arising from the topological phase transition. From density functional theory, the cone disperses over $\sim 2\,\mathrm{eV}$ but it is isolated from other electronic contributions on a range of about 500 meV. A refined growth was made to ensure the chemical potential to sit close to the nodal point.

We have found a series of resonant excitations corresponding to inter- and intra-Landau level transitions in the magneto-transmission and magneto-reflection figure 48(a-b). They were modelized by a massive Dirac model, extrapolating at low field to a finite energy corresponding to twice the gap energy $2\Delta = 32\,\mathrm{meV}$. We have also extracted, from the same model, the in-plane asymptotic velocity of the Dirac cone $\sqrt{v_x v_y} = 4 \times 10^5\,\mathrm{m/s}$.

In addition, we performed the near-normal incidence reflectivity in the full range of energy possible. We have extracted, through Kramers-Kronig relations, the real part of the optical conductivity. In figure 48(c) a magnifying view of the low-energy excitation of σ_1 is plotted. We identify a clear linear dispersion of σ_1 up to 300 meV, that can be modelized by a 3D massive Dirac model.

However, this model implies a velocity of $v = 1.8 \times 10^5\,\mathrm{m/s}$. The reason for such a difference between the two measurements, is that optical conductivity probes the joint density of states in 3D while magneto-optic only probes the planes perpendicular to the magnetic field. Thus, we argue in favor of an anisotropic cone in the three dimensions of the Brillouin zone to explain this disagreement between the measurements.

It is also interesting to notice that the transparent window, in which the magneto-optical measurements were performed, corresponds to a region where the joint density of states becomes lower than the absorption coefficient. It allows multiple reflections in the in-plane parallel layers of the sample, directly visible in the optical conductivity curve by the presence of Fabry-Perot interferences.

In conclusion, TlBiSSe can be regarded as a "textbook" example of a 3D Dirac semimetal, and the simplest theoretical description is sufficient enough to describe the electrodynamics at low energy. More details about this work can be found in Le Mardelé *et al.*, Phys. Rev. B **107**, L241101 (2023).

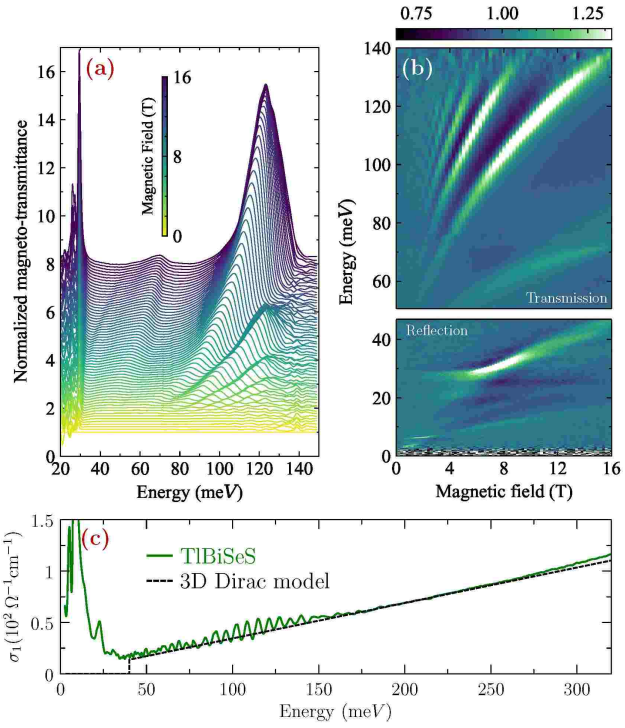

FIG. 48. *Panel (a) normalized magneto-transmittance of TlBiSSe up to 16 T. Panel (b) Color map of the transmission and reflection normalized by an average of all the curves in a range of 1 T around each magnetic field. Panel (c) real part of the optical conductivity at 0 T up to 320 meV*

F. Le Mardelé, J. Wyzula, I. Mohelský, M. Orlita
S. Nasrallah, M. Loh, S. Ben David, O. Toledano, A. Akrap, D. Santos-Cottin (Fribourg University), D. Tolj (EPFL, Lausanne), M. Novak, N. Barišsić, Z. Rukelj (University of Zagreb), G. Eguchi, S. Pashen (Technische Universität Wien), J. Chen, A. Kimura (Hiroshima University)

Fermi surface of the chiral topological semimetal CoSi

Topologically non-trivial band structures give rise to a variety of interesting physical phenomena like Fermi arc surface states, unusual transport properties and non-linear optical responses. Chiral B20 compounds crystallizing in space group 198 have been intensively studied in recent years due to symmetry-protected topological degeneracies including multifold crossing points, Weyl points and nodal planes. The semimetal CoSi is a prime example of this material class.

Angle-resolved photoemission spectroscopy (ARPES) and quasiparticle interference experiments confirmed main features of the band structure predicted by density functional theory and its topological character, but could not resolve important features like a spin-orbit coupling induced splitting of the bands. Previous quantum oscillation (QO) studies detected oscillation frequencies that can be traced back to Fermi surface (FS) pockets centered around the R-point [Huber *et al.*, Phys. Rev. Lett. **129**, 026401 (2022)]. However, further FS sheets are expected around the Γ-point which have not been observed experimentally. A precise knowledge of the FS is key in enabling calculations of topological response functions and interpreting experimental results.

Here, we report on a high-field study of the de Haas-van Alphen (dHvA) effect in CoSi revealing previously undetected QO frequencies that arise from FS pockets located around the Γ-point. To probe the magnetization we used cantilever-based torque magnetometry with a capacitive readout. The experiments were performed in a dilution refrigerator with a setup allowing for in-situ sample rotation.

Figure 49(a-b) show a representative measurement recorded at 30 mK and a specific orientation of the applied magnetic field. The Fourier transform shown in figure 49(c) reveals the existence of a quantum oscillation frequency, labeled η, that has not been detected in previous studies. We analyze the temperature dependence of the oscillations in the range between 30 mK and 1 K and find that the novel η frequency displays a much stronger temperature-dependent damping as compared to the well-known frequencies α and β. Figure 49(d) shows a fit of the FFT amplitudes with the Lifshitz-Kosevich temperature reduction factor R_T yielding an effective mass of $m_\eta = 7.5\, m_e$.

Upon rotation of the sample the frequency η can be traced over a limited angular range around the orientation shown here and displays a mild angular dispersion. Further previously unobserved oscillation frequencies are detected at other angles.

A systematic comparison of the oscillation frequencies, their angular dispersion and effective masses with predictions from first-principles calculations lets us trace the origin of these novel QO frequencies to quasiparticle orbits on FS sheets located around the Γ-point of CoSi. In combination with additional measurements of the Shubnikov-de Haas effect in magnetic fields up to 18 T we were able to map out the missing FS pockets providing experimental data for the full FS.

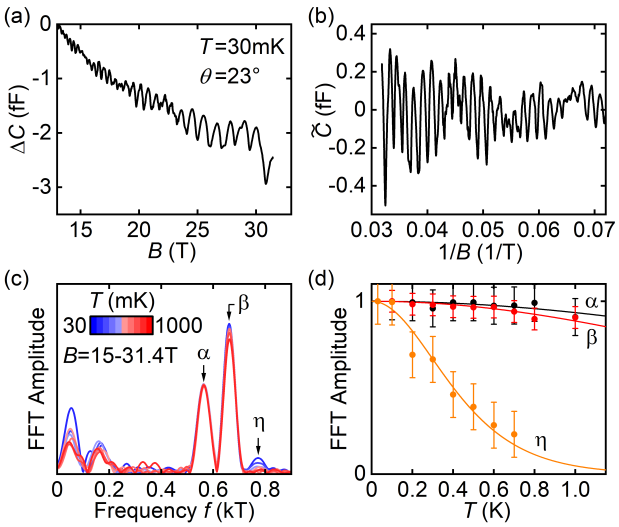

FIG. 49. *de Haas-van Alphen oscillations in CoSi. (a) Capacitance change ΔC as a function of the applied magnetic field B. (b) Oscillatory part of the capacitance $\tilde{C}$ as a function of inverse field exhibiting characteristic dHvA oscillations. (c) FFT spectra of the oscillations recorded at different fixed temperatures. Three peaks can be clearly identified. (d) FFT amplitudes of the detected frequencies as a function of temperature T. Lines indicate fits with the Lifshitz-Kosevich temperature reduction factor R_T. The η-peak shows a strong damping indicating an effective mass of $m_\eta = 7.5 m_e$.*

Our findings complete the experimental determination of the FS of CoSi and lay the foundation for precise calculations of topological response functions in this material.

N. Huber, S. Mishra, I. Sheikin
K. Alpin, A. P. Schnyder (MPI-FKF, Stuttgart), G. Benka, A. Bauer, C. Pfleiderer, M. A. Wilde (Technical University of Munich)

Magnetic breakdown and topology in the Kagome superconductor CsV_3Sb_5

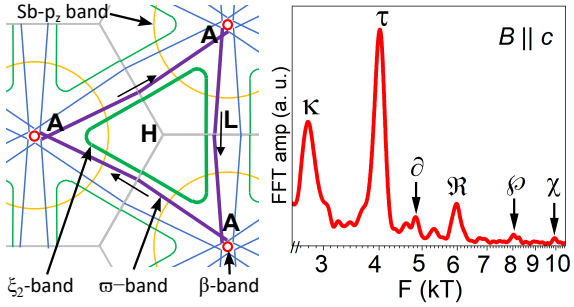

FIG. 50. ***(left)*** *2 × 2 reconstructed Fermi surface of CsV_3Sb_5 for $k_z = \pi/c$ in repeated zones. Capital letters refer to Brillouin zone points.* ***(right)*** *High-frequency section of the oscillation spectrum at 1.5 K on a log field scale. The κ orbit corresponds to the sum of the ξ_2 and ϖ orbits, while the τ orbit represents two basic triangular ϖ units. Correspondingly, $\Re$, $\wp$, χ contain 3, 4 and 5 triangular building blocks, respectively. ∂ is the sum of the ξ_2 and τ orbits.*

The recently discovered Kagome lattice compounds AV_3Sb_5 (A = K, Rb, Cs) display a fascinating interplay of superconductivity, charge density wave (CDW) order and non-trivial topology of the electronic band structure. The CDW order is itself unconventional due to the presence of chiral charge order and time-reversal symmetry breaking inducing a large anomalous Hall effect and non-reciprocal transport. The transition into the CDW state is accompanied by an extensive reconstruction of the Fermi surface. While angle resolved photoemission spectroscopy (ARPES) has been invaluable in exploring the electronic structure, effects due to matrix-elements have largely precluded the visualization of the reconstructed band-structure. In contrast, quantum oscillations are a direct manifestation of the Fermi surface and can reveal information on the quasi-particle effective masses, their lifetimes, and their topological state.

We have performed quantum oscillation measurements on high quality single crystals of CsV_3Sb_5 using the tunnel diode oscillator technique in magnetic fields up to 86 T. The sensitivity of the tunnel diode oscillator setup developed at the LNCMI coupled with the highest magnetic fields available enabled to detect a rich spectrum of quantum oscillations ranging in frequencies from 50 T to to 60 000 T. The high-field data reveal a sequence of magnetic breakdown orbits that allow us to construct a model for the folded Fermi surface of CsV_3Sb_5, shown in figure 50 (left). The dominant features are large triangular Fermi surface sheets that cover almost half the folded Brillouin zone highlighted in figure 50 in violet (ϖ band with a frequency of 1943 T) and green (ξ_2 band at 804 T). These orbits form the building blocks that combine one-by-one to form a series of approximately equally spaced frequencies that dominate the high-field oscillation spectrum as shown in figure 50 (right) and in more detail in figure 51.

Notably, these Fermi surface sheets had not yet been detected in ARPES. In addition to mapping this folded Fermi surface, we have extracted the Berry phases of the electron orbits from Landau level fan diagrams near the quantum limit without the need for extrapolations, thereby unambiguously establishing the non-trivial topological character of several electron bands in this Kagome lattice superconductor.

For more details please see [Chapai, *et al.* Phys. Rev. Lett. **130**, 126401 (2023)].

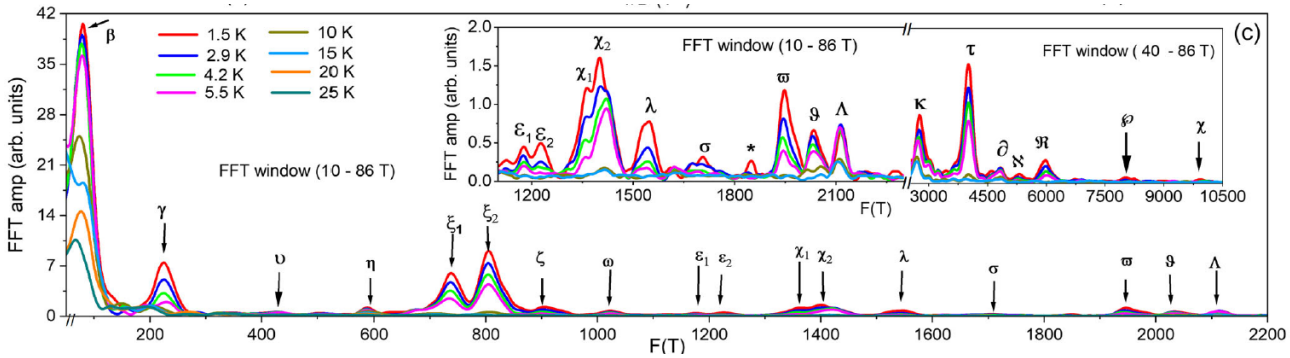

FIG. 51. *Fast Fourier transform of the quantum oscillations in CsV_3Sb_5 observed in the TDO frequency versus field (Δf_{TDO} versus $1/B$) at various temperatures. Inset shows expanded view of the high frequency region.*

M. Leroux, V. Oliviero, D. Vignolles, N. Bruyant
R. Chapai, M. P. Smylie, D. Y. Chung, M. G. Kanatzidis, W.-K. Kwok, J. F. Mitchell, U. Welp (Argonne National Laboratory, Chicago), M. P. Smylie (Hofstra University, New York), M. G. Kanatzidis (Northwestern University, Chicago)

Pauli-limit violation in square-planar nickelate superconductors

The origin of high-temperature superconductivity (high-T_c) in cuprates is still one of the great unsolved mysteries in condensed matter physics. In the past three decades, intense efforts were devoted to the search of cuprate-like compounds that could reproduce their structure and properties. For instance, this motivated the studies in layered materials such as ruthenates, cobaltates, and iron pnictides. While none turned out to share an analogue of the two-dimensional high-T_c superconductivity of cuprates, a breakthrough recently came with the discovery of infinite-layer nickelates $RNiO_2$ (R = rare-earth). Nickel stands immediately to the left of copper in the periodic table, and nickelates' structure consist of square-planar NiO_2 planes in the Ni^{1+} oxidation state with a cuprate-like $3d^9$ electronic structure and lifted orbital degeneracy. Nickelates thus realize a true superconducting analogue of the CuO_2 planes with Cu^{2+} state in the high-T_c cuprates.

Indeed, despite the difficulty of the synthesis, nickelate superconductors share the closest electronic structure to the cuprates to date and also some of the cuprates's key properties (charge order and magnons, linear resistivity, strange metal near optimal doping, and Fermi-liquid in the overdoped regime), yet, crucially, not all. Notably, depending on the rare earth elements and doping, they exhibit a range of electronic structure from 3D to quasi-2D, and a range of superconducting properties from the more to the less conventional. This prompts the question of the correlation between dimensionality and unconventional superconductivity, and of where does the superconductivity in nickelates stand between the quasi-2D high-T_c cuprates and the 3D high-T_c multiband iron pnictides. A second issue, considering the richness of cuprates' phase diagram, is that of new phases or orderings that would coexist with superconductivity in nickelates, and their role and relation to the pairing mechanism, especially if quantum critical transition exists. For example, a charge ordering (translational symmetry breaking) was reported in the undoped and underdoped regimes of the hole-doped nickelates. However, inside the superconducting dome, a coexisting symmetry-breaking state (like the charge order in cuprates) has yet to be observed in nickelates.

In our studies, we investigated several families of nickelates: $Nd_{1-x}Sr_xNiO_2$ and $La_{1-x}R_xNiO_2$ (where R = Ba, Ca or Sr), in thin films form with maximum thickness of typically 15 nm (current state-of-the-art), some lithographied into Hall bars for magnetotransport measurements. Contacts were made by wirebonding through the protective capping layer. Depending on dopants and the rare-earth spacer layer (figure 52), we observe a crossover from a two-dimensional to a three-dimensional superconducting state in the angular dependence of the upper critical fields at temperatures down to 0.5 K at high pulsed magnetic fields. From this, we speculate that $La_{1-x}Ba_xNiO_2$ is a purely 2D superconductor with the highest hope of achieving cuprates-like pairing, whereas a Ca-doped $NdNiO_2$ (which has yet to be synthesized) could carry the strongest 3D-like character and potentially nodeless superconductivity. In addition, in critical current and magnetoresistance measurements, we find that the superconducting state in all nickelate families studied exhibit an in-plane C_2 rotational symmetry (nematic) which breaks the C_4 rotational symmetry of the square lattice of NiO_2 planes.

Finally, while in $Nd_{1-x}Sr_xNiO_2$ we confirmed previous studies that the Pauli-limit is respected, in $La_{1-x}R_xNiO_2$ we find a surprisingly large (2-3 times) violation of the Pauli-limit, in all crystallographic directions and over the entire superconducting dome (with H_{c2} of the order of 30 T despite T_c around 7 K). This suggests the tantalizing possibility that nickelates might also exhibit an evolution from spin-singlet to spin-triplet superconductivity with the appropriate spacer layer.

These early results evidence the promises of nickelates as true superconducting analogues of the CuO_2 planes in high-T_c cuprates. Searching for the differences, nickelates are fast emerging as a promising touchstone to understand high-T_c superconductivity.

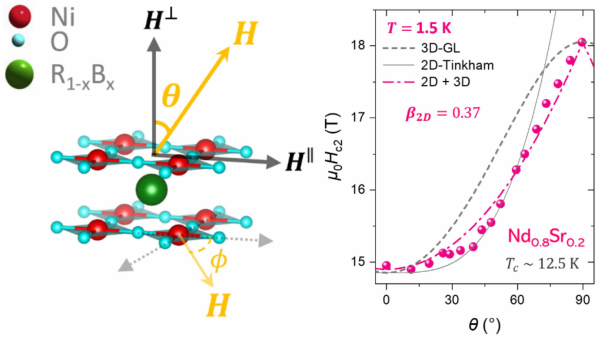

FIG. 52. *(left) R = La/Nd, B = Sr/Ca, crystal structure of nickelates showing the NiO_2 layers analogous to cuprates. (right) angular dependence of the upper critical field in Nd-nickelates at T=1.5 K. The 2D-Tinkham model fits well near T_c, whereas neither a purely 2D-Tinkham nor a 3D-GL-like model fits at the lowest temperatures, but rather a combination of the two.*

For more details please see [Chow, *et al.* arXiv 2204.12606 (2022)] and [Chow, *et al.* arXiv 2301.07606 (2023)].

M. Leroux, M. Pierre, M. Goiran, W. Escoffier
L.E. Chow, A. Ariando (National University of Singapore), Z.Y. Luo, S. Zeng, K. Rubi, N. Harrison (NHMFL, Los Alamos), K. Y. Yip, X.Y. Liu, S. K. Goh (The Chinese University of Hong Kong), C.J. Li (Southern University of Science and Technology, Shenzhen)

^{29}Si NMR study of the iron silicide superconductor LaFeSiH

Superconductivity was recently found below $T_c = 10\,\mathrm{K}$ in the iron silicide compound LaFeSiH, thus enlarging the broad class of Fe-based superconductors to materials without pnictogen or chalcogen elements. Interestingly, it has also been reported that LaFeSiH undergoes an orthorhombic transition upon cooling.

This immediately raises the question as to whether LaFeSiH has concomitant stripe-type antiferromagnetic order, as found in Fe pnictides, or a ground state without magnetic order, as found in the singular case of FeSe. In order to answer this question, we have performed ^{29}Si nuclear magnetic resonance (NMR) experiments in a LaFeSiH powder sample [Hansen *et al.*, arXiv:2309.02241].

In general, magnetic order is detected in NMR through changes in either the resonance lines or the spin-lattice relaxation rate T_1^{-1}. Here, all observables measured in our ^{29}Si NMR data of LaFeSiH show a weak and smooth temperature dependence that rules out the presence of magnetic order; both the Knight shift (figure 53c) and $(T_1T)^{-1}$ (figure 53d) decrease smoothly upon cooling and saturate to a constant value below $\sim$20 K.

With a detection limit set by the NMR linewidth of 45 kHz (figure 53a), we derive an upper bound of $\sim 0.01\mu_B$ for a putative ordered moment. We further notice that ordered moments as small as $0.05\,\mu_B$ lead to an enhancement of T_1^{-1} upon cooling for ^{31}P in $BaFe_2(As_{1-x}P_x)_2$ ($x \simeq 0.3$), which is totally excluded by our ^{29}Si data here. This confirms that there is no ordered moment greater than $\sim 0.01\mu_B$ in LaFeSiH.

In fact, both K and $(T_1T)^{-1}$ are well described by an activated form,

$$a + b\,\exp\left(\frac{-\Delta}{k_B T}\right),$$

that yields virtually identical gap values: $\Delta_K = 106 \pm 24$ K and $\Delta_{T_1} = 101 \pm 38$ K, respectively. This activated dependence is typical of strongly overdoped Fe-based superconductors. In strongly overdoped $Ba(Fe_{1-x}Co_x)_2As_2$, the thermal activation of $(T_1T)^{-1}$ (also satisfying $\Delta_{T_1} \simeq \Delta_K$) has been ascribed to spin fluctuations involving small momentum transfer (so-called "intra-band" scattering).

Further, the constant linewidth down to 2.8 K (figure 53b) and the absence of stretched-exponential behavior (not shown) of the magnetization recovery in T_1 measurements are typical of spatially homogeneous systems with weak electronic correlations.

In conclusion, our NMR study unambiguously show that LaFeSiH has neither spin order nor even local moments with stripe-type AFM fluctuations. This raises the prospect of enhancing the T_c of LaFeSiH by appropriate chemical substitutions. These presented data also contribute to establishing a solid, quantitative phenomenology of NMR in overdoped Fe-based superconductors that could be confronted to theoretical predictions based on realistic band structures.

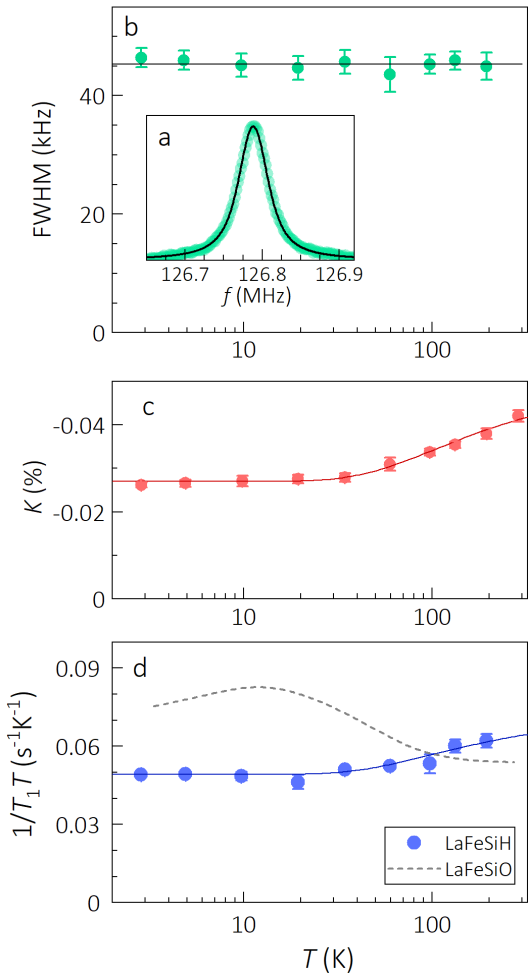

FIG. 53. *(a) ^{29}Si NMR line (green) in a field of $\sim$15 T and T = 2.85 K. The line is a fit to a Voigt profile. (b) Full width at half maximum. (c) Magnetic hyperfine shift K. The solid trace is a fit to an activated dependence (see text). (d) Spin-lattice relaxation rate T_1^{-1} divided by T. The solid trace is a fit to an activated dependence (see text). For comparison purpose, the dashed trace shows $(T_1T)^{-1}$ data in LaFeSiO from Hansen et al. npj Quantum Mater. **7**, 86 (2022). While the values are similar, the T dependence is very different, due to the presence of (rather weak) magnetic fluctuations in LaFeSiO.*

T. Pelletier, H. Mayaffre, M.-H. Julien
J.-B. Vaney, M.R. Suchomel, S. Tencé (ICMCB, Bordeaux)

High-field NMR study of spin fluctuations driving field-reinforced superconductivity in UTe_2

Uranium-based superconductor UTe_2 provides an attractive platform for studying the novel physics of spin-triplet and topological superconductivity (SC) in bulk materials. Magnetoresistivity measurements performed in 2019, both in continuous and pulsed fields, revealed that SC in UTe_2 is significantly enhanced when the magnetic field (H) is applied along the crystallographic b axis (figure 54). This leads to an increase of the upper critical field up to the field of a metamagnetic transition $\mu_0 H_m = 35$ T. An essential ingredient for this field-reinforced SC has been proposed to be an interplay with U-5f electron spin fluctuations.

To confirm the presence and elucidate the nature of spin fluctuations in UTe_2, we conducted ^{125}Te-NMR experiments in high magnetic fields [Tokunaga *et al.*, Phys. Rev. Lett. **131**, 226503 (2023)]. For the experiment, we prepared ^{125}Te-enriched high-quality single crystals having $T_c = 2.0$ K using the molten salt flux method discovered recently by ourselves. The natural abundance of ^{125}Te nuclei is only 7%, so that our enrichment up to 99% largely enhanced the NMR signal, allowing us to measure the field dependence of the NMR relaxation rates $1/T_1$ and $1/T_2$ up to 32 T.

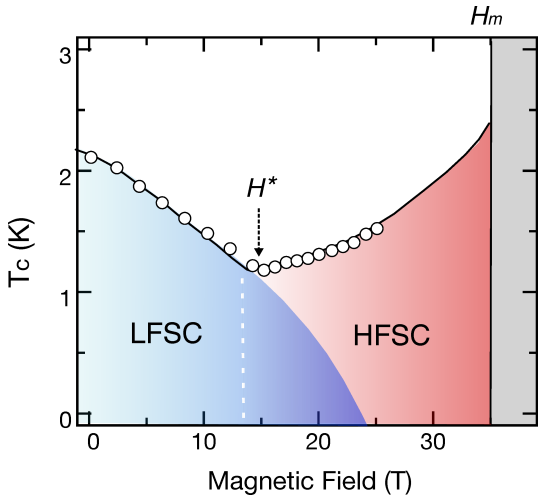

FIG. 54. *Schematic H-T phase diagram for UTe_2 in $H\|b$ presents a high-field SC (HFSC) and a low-field SC (LFSC) phases. The $T_c(H)$ data (white circles) are from [Sakai et al., Phys. Rev. Lett.* ***130****, 196002 (2023)].*

Figure 55 shows our $1/T_1$ and $1/T_2$ data for $H\|b$. The observed magnetic field dependence and the scaling between the two relaxation rates, $(1/T_2)/(1/T_1) \approx 36$, demonstrates that the dominant fluctuations in this material are the *longitudinal* ones. While $1/T_1$ and $1/T_2$ are nearly field-independent at lower fields, both quantities start to increase above $\simeq 15$ T and show a tendency to diverge above 32 T. Above 32 T, T_2 values become extremely short, shorter than the dead time of NMR spectrometer, preventing us to observe NMR spin-echo signals (grey area in figure 55). This confirms the divergence of spin fluctuations in the vicinity of the field-induced metamagnetic transition at H_m. Previous macroscopic studies defined $\mu_0 H^* \approx 15$ T as the characteristic field above which $T_c(H)$ shows an upturn as a high-field SC phase emerges on top of a low-field SC phase (figure 54). Our NMR results show that H^* is also the characteristic field above which spin fluctuations begin to develop on approaching the metamagnetic transition, confirming that these fluctuations indeed enhance the pairing interactions.

Figure 55 also presents the apparent scaling of the field dependence of our NMR relaxation rate data and of the quadratic coefficient A extracted from a Fermi-liquid fit to the electrical resistivity at low temperatures in $H\|b$. The strong increase of A near H_m has been regarded as due to the enhancement of the effective mass m^*. A similar strong field-dependence, accompanying a sharp maximum around H_m, has also been observed in the Sommerfeld coefficient γ. Our NMR data in $H\|b$ thus provide experimental confirmation of recent theoretical prediction that longitudinal spin fluctuations should give rise to the enhancement of the A coefficient and the γ around the metamagnetic transition.

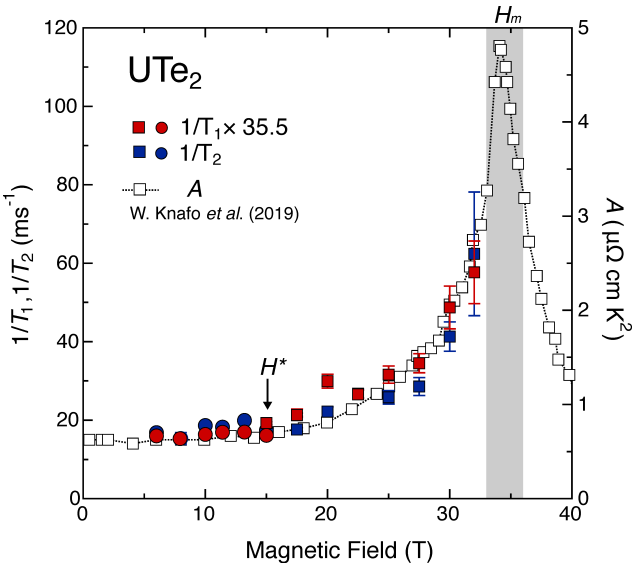

FIG. 55. *Magnetic field dependence of our $1/T_2$ and $1/T_1$ (scaled by a factor of 35.5) NMR data, compared to the quadratic coefficient A of the low-T resistivity data from [Knafo et al., J. Phys. Soc. Jpn.* **88***, 063705 (2019)].*

M. Horvatić, S. Krämer
Y. Tokunaga (Japan Atomic Energy Agency, Tokai), K. Ishida (Kyoto University), D. Aoki (Tohoku University, Oarai), G. Knebel, G. Lapertot (CEA-Grenoble)

Tuning the pairing mechanism of a superconductor

For a long time, all known superconductors shared a common mechanism responsible for this superconducting (SC) state; the interaction between electrons and the underlying lattice. The discovery that superconductivity could also be induced by direct interactions between electrons, for example mediated by their magnetic properties, was a real breakthrough. Nowadays, this seems to be always the case for strongly correlated electron systems. However, a precise identification of this pairing mechanism remains a major challenge. In the high-T_c cuprates for example, even though it is clear that electron-electron interactions are responsible for the record large critical temperatures, still no consensus emerges on which interactions control the formation of the Cooper pairs. Very recently we have shown [Rosuel *et al.*, Phys. Rev. X **13**, 011022 (2023)] that another strongly correlated system, UTe_2, is the first system for which two different pairing mechanisms can lead to different SC states. Moreover, a magnetic field can tune which mechanism will drive the SC state.

It was known already that superconductivity is reinforced in UTe_2 when a magnetic field is applied in a particular crystallographic direction, corresponding to the hard magnetization axis (b-axis of the orthorhombic structure). This very surprising phenomenon has been explored on high quality crystals with new measurements of specific heat and thermal expansion, performed up to 36 T and down to very low temperatures. With these probes, we revealed that the field-reinforcement of the SC state is due to a thermodynamic phase transition into a new SC phase above 15 T (see figure 56). It was also discovered that the anomaly (the specific heat jump) which marks the transition between the normal state and the SC state broadens more than 4 times in the field reinforced state. This is unique; in the very few other examples of superconductors displaying multiple SC phases, the SC states differ only by a change of symmetry, and in such a case, there is no remarkable change of the specific heat anomaly. Here in UTe_2 it is likely that the low field spin-triplet SC phase is driven by ferromagnetic fluctuations, whereas the high field phase with a broad specific-heat anomaly would emerge from other magnetic fluctuations developing under magnetic field.

A peculiarity of the phase diagram of UTe_2 apparent on the figure is that the field-reinforced SC state abruptly disappears above 35 T: this coincides with a metamagnetic transition, characterized by a large first-order jump of the magnetization of $\simeq 0.5\mu_B$. These "other" magnetic fluctuations are most likely related to the emergence of the metamagnetic transition. Detailed analysis shows that a pairing mechanism controlled by the metamagnetic field could explain quantitatively the strong broadening of the specific heat anomaly, as well as its high sensitivity to a small misalignment of the field from the b-axis. However, there is a surprise ingredient in this explanation; one has to admit that the high field phase, contrary to the low-field one, would be a spin-singlet. This is counter-intuitive; a spin singlet state for the Cooper pairs is usually detrimental for superconductivity at high magnetic field, because of the loss of magnetic energy due to the alignment of spins in the field. In contrast, a triplet state, allows to form Cooper pairs with spins polarized along the applied magnetic field, hence it should be favored at high field. Nevertheless, this additional twist is consistent with some theoretical predictions studying precisely the competition of different pairing mechanisms in this system under pressure, where several SC phases have also been discovered.

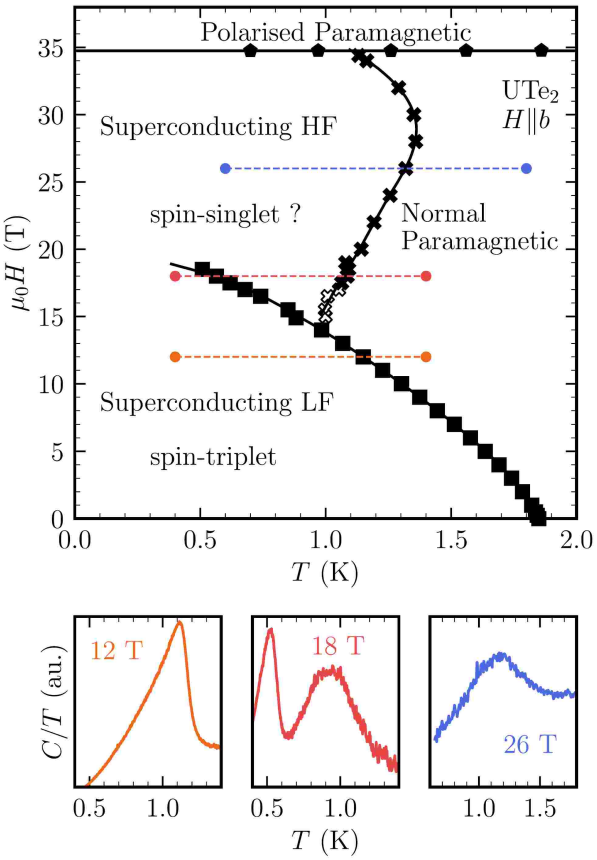

FIG. 56. *Two different SC phases in UTe_2 as observed by thermodynamic specific heat measurements, showing the transition line between the two phases. At the bottom, the change of the specific heat anomaly, becoming very broad in the high field phase is very clear: note the curve at 18 T where both anomalies are successively observed.*

A. De Muer, G. Seyfarth
A. Rosuel, G. Knebel, A. Pourret, N. Marquardt, Q. Niu, S. Rousseau, G. Lapertot, D. Braithwaite, J. Flouquet, J.-P. Brison (INAC, CEA Grenoble), C. Marcenat, T. Klein (Néel Institute, CNRS-UGA, Grenoble), D. Aoki (Tohuku University)

High-sensitivity specific heat study of the low-temperature high-field corner of the $H-T$ phase diagram of FeSe

FeSe is a particularly interesting iron-based superconductor, composed only of c-axis stacking of FeSe layers without any charge reservoir. In contrast to other iron-based materials, this system does not order magnetically (but still undergoes a structural phase transition), and superconductivity here competes with an orbitally ordered nematic state. Despite its moderate critical temperature ($T_c \simeq 9\,$K), FeSe can be seen as an extremely high T_c material due to its very low Fermi energy E_F, comparable to the superconducting gap Δ_{SC}.

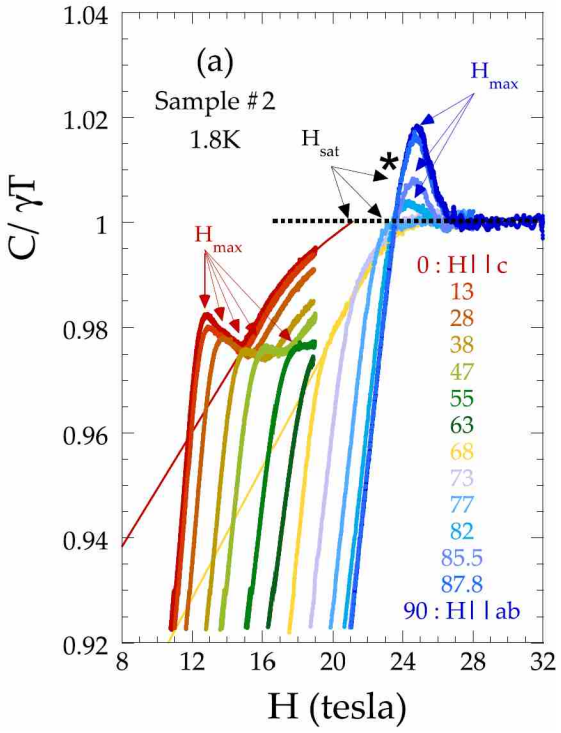

FIG. 57. *Magnetic field dependence $C(H)$ at $T = 1.8\,K$ for the indicated values of the angle θ between the magnetic field and the c axis. Note that no increase of C/T above H_{max} is observed for $\theta \gtrsim 80°$, but a clear kink remains visible below H_{max} in this angle range (marked by the star).*

Here we report [Klein *et al.*, Phys. Rev. B **107**, 224506 (2023)] on an extensive experimental study of the low-temperature high-field corner of the H-T phase diagram in FeSe using high-sensitivity specific heat C measurements. Indeed, since Δ_{SC}, E_F and the Zeeman energy are surprisingly close in this compound, different superconducting phases as well as Lifshitz transitions in the electronic structure may exist.

We show that two distinct anomalies are visible in $C(H)$ (below $\simeq 3\,$K), see figure 57 and figure 58(a), notably a (smeared) jump at the superconducting transition and a kink in $C(H)$. This second structure lies either below (for H close to the ab plane) or above (for field orientations close to the c direction) the superconducting transition, indicating that it is most probably related to a field-induced change in the electronic structure. Moreover, quantum oscillations are clearly observed below $\simeq 2\,$K (see figure 58(b), with a frequency of about 200 T and yielding an effective mass $m^\star \simeq 4m_e$.

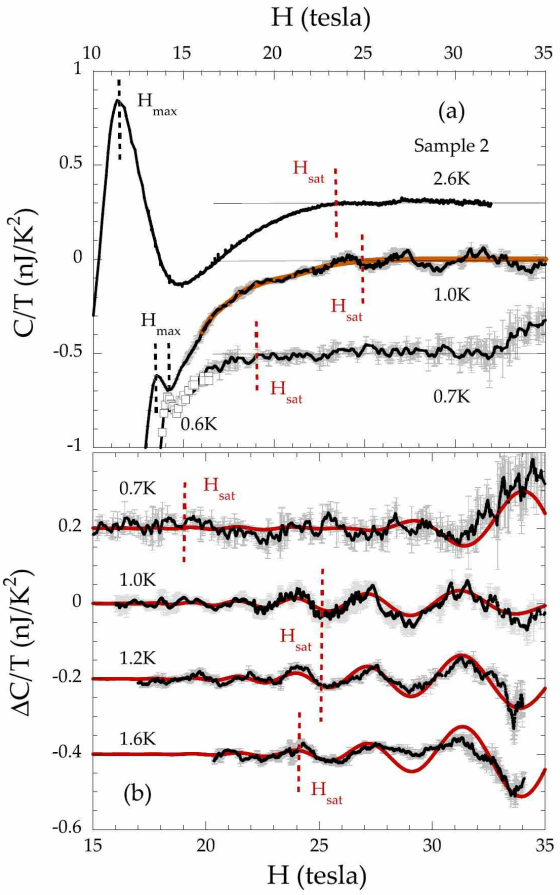

FIG. 58. *(a) Field dependence of C/T for the indicated temperatures ($H \parallel c$), the different curves have been arbitrarily shifted for clarity. A (smeared) superconducting jump is visible for $H \simeq H_{max}$, and C/T still increases above the transition saturating for $H \simeq H_{sat}$.(b) Quantum oscillations (for the indicated temperatures) after subtraction of a smooth background [solid brown line in (a)]. The red lines are fits to the data using the standard Lifshitz-Kosevich model. Note that the oscillations are observed well below H_{sat} for $T \simeq 1\,K$, indicating that H_{sat} lies within the normal state.*

A. DeMuer, G. Seyfarth
L. Doussolin, T. Klein, H. Cercellier, P. Toulemonde (Néel Institute, CNRS-UGA, Grenoble), A-A. Haghighirad, F. Hardy (Karlsruhe Institute of Technology), C. Marcenat (INAC, CEA Grenoble)

Magnetic transitions in the highly anisotropic ferrimagnet $ErFe_5Al_7$

RFe_5Al_7 with tetragonal crystal structure exhibits strongly anisotropic ferrimagnetic properties with easy-plane (R = Tb, Dy, Ho, and Er) or easy-axis (R = Tm) anisotropy at low temperatures. The balance between exchange and anisotropy interactions is modified at high magnetic fields, which results in field-induced magnetic transitions with a noticeable spin-lattice coupling under magnetic fields applied along the easy magnetization axis. $ErFe_5Al_7$ is exceptional in this family of compounds, since it shows field-induced transitions under magnetic fields applied along the hard magnetization axis [110] as well as along the easy axis [100] within the basal plane of the tetragonal lattice. $ErFe_5Al_7$ orders with a collinear ferrimagnetic structure at the Curie temperature T_C = 201 K, and has a compensation point of T_{comp} = 33 K, where the magnitudes of the Er and Fe magnetic moments are equal.

In this work, magnetization, magnetostriction, and x-ray magnetic dichroism data have been combined to provide a comprehensive picture of the magnetic properties of the strongly anisotropic ferrimagnet $ErFe_5Al_7$ in pulsed magnetic fields applied along the hard magnetization axis [110], focusing on the microscopic nature of the two field-induced magnetic transitions observed around T_{comp}. In contrast to previous assumptions, we found (figure 59) that one of the field-induced transitions accompanied by strong magnetoelastic couplings originates from the rotation of the Er 4f magnetic moments from the easy to the hard axis. In addition, the Er 5d moments follow the rotation of the Er 4f moments due to the intra-atomic 4f-5d exchange coupling across the field-induced transitions. The other field-induced transition corresponds to a jump from the easy magnetization direction to the forced ferromagnetic state.

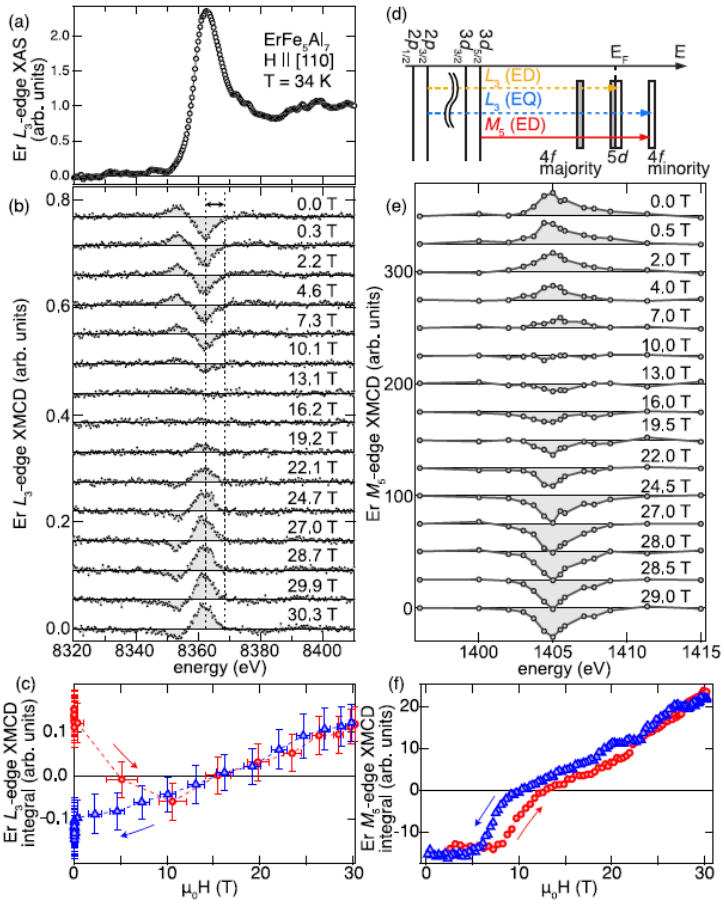

FIG. 59. *(a) Er L_3-edge XAS spectra at 30.3 T. (b) Er L_3-edge XMCD spectra at selected B. (c) B dependence of the XMCD signals where the electric-dipole transition ($2p_{3/2} \longrightarrow 5d$) is predominantly involved. (d) Schematic of the electronic structure involved in the electric-dipole (ED) and electric-quadrupole (EQ) transitions at the Er L_3 and M_5 edges. (e) Er M_5-edge XMCD spectra at selected B. (f) Er M_5-edge XMCD integrals as a function of B.*

F. Duc

S. Yamamoto, D.I. Gorbunov, A. Miyata, M. Uhlarz, J. Wosnitza (HLD-EMFL, Dresden), O. Prokhnenko, A. Gazizulina, E. Weschke (HZB, Berlin), I.F. Diaz-Ortega (Área de Química Inorgánica-CIESOL, Almería), C. Strohm (DESY, Hamburg), M. S. Henriques, A. V. Andreev (FZU Institute of Physics, Prague), O. Mathon (ESRF, Grenoble), H. Nojiri (Institute for Material Research, Sendai)

Biology and Molecular Magnetism

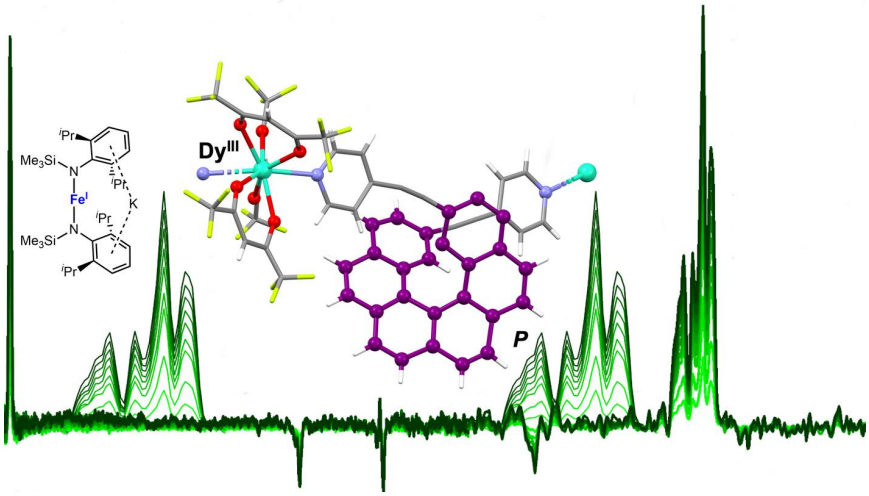

Single molecule magnetic behavior of linear Iron(I) Arylsilylamides

Single-molecule magnets (SMMs) have attained considerable interest as they pose potential for future applications in high-density information storage, quantum computing, and magnetic refrigeration. In this regard, SMM's based on two-coordinate 3d transition metal (TM) complexes came into the scientific spotlight recently. In comparison with other 3d-TM complex geometry they can exhibit unquenched orbital angular moment, that can contribute to the magnetic moment. The seminal example constitutes the $S = 3/2$ system $[Fe(C(SiMe_3)_3)_2]^-$ with an effective relaxation barrier of $U_{eff} = 226\,cm^{-1}$ at zero field. It allowed for the first-time observation of magnetic blocking for a mononuclear 3d-transition metal system. In few other previously reported cases it showed however that the presence of an $S = 3/2$ ion in a (quasi)linear environment is thereby not a sufficient criterion for the observation of magnetic blocking behaviour.

This divergent behaviour called for a study to shed light on this issue. We therefore studied the electronic properties and magnetic behaviour of two-coordinate iron(I) silylamide complexes (figure 60)

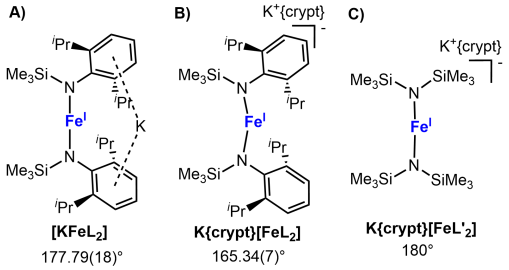

FIG. 60. *Linear iron(I) silylamide complexes (A,B) and comparison with previously reported complex (C).*

It showed that the highest barrier for the relaxation of magnetisation is observed in case of a near-linear ligand geometry ($U_{eff} = 184\,cm^{-1}$) with a geometrically constrained ligand set (figure 61) as found in [KFeL2]. This also results in magnetic blocking below 4.5 K, that is still unusual for mononuclear 3d-metal complexes. Temperature dependent magnetic measurements further revealed that the behaviour of [KFeL2] can be fitted by the using the classic spin Hamiltonian with Zeeman and zero field-splitting,

$$\hat{H} = \mu_B \vec{B}\boldsymbol{g}\vec{S} + D[\hat{S}_z^2 - \tfrac{1}{3}S(S+1) + \tfrac{E}{D}(\hat{S}_x^2 - \hat{S}_y^2)].$$

This gave $g_x = g_y = 2.27$, $g_z = 3.31$ and $D = -104\,cm^{-1}$. This approach is formally forbidden for near-linear complexes with degenerate ground states, yet is apparently also applicable here. Theoretic calculations of complex $[KFeL_2]$ using ab-initio ligand field theory showed, that the observed barrier coincides with an excitation from the magnetic ground state $m_J = 7/2$ to the first excited state $m_J = 5/2$ ($E = 212\,cm^{-1}$). This was supported by vibrational spectroscopy at very low temperatures in a variable magnetic field, that yielded a magnetic transition at $182\,cm^{-1}$.

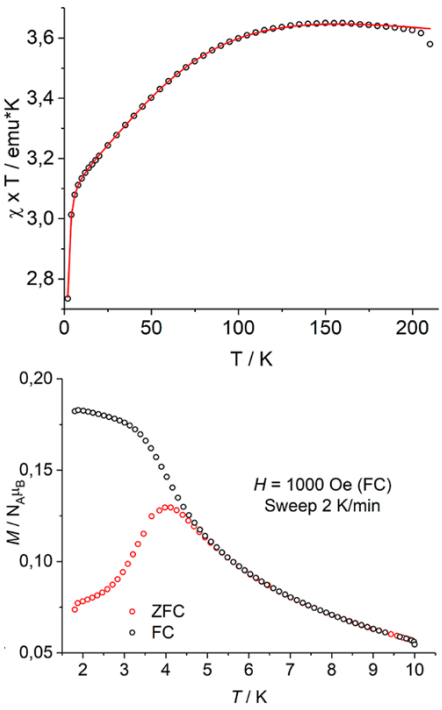

FIG. 61. *χT vs T measurements (top) and zero-field-cooled/field-cooled (ZFC/FC) magnetization measurements (bottom) of $[KFeL_2]$.*

Together with the limited literature precedence, following guiding principles can be drawn for designing single ion magnets with two-coordinate iron(I) ions: A) Rigidity of the complex geometry, B) linearity of the principal bond axis and C) use of weak-field σ/π-donor ligands, whereas the local symmetry of the ligand (C_{2v} or C_{3v}), and its substituents are a lesser factor. This study thus expands on the synthetic possibilities for mononuclear transition metal complexes that show magnetic blocking, and might lead to other quasilinear ligand architectures for SMM's. Furthermore, the herein observed excellent agreement of theory with experiment will give credence to the in silico design of novel linear metal complexes, like ones with heavier donor atoms which to this day are synthetically unfathomable. For more details please see [Weller *et al.*, Inorg. Chem. **61**, 3153 (2023)].

I. Mohelsky, M. Orlita
R. Weller, C. G. Werncke (Philipps-University, Marburg), M. Atanasov, F. Neese (MPI for Kohlenforschung, Mülheim an der Ruhr), E. Bill (MPI for Chemical Energy Conversion, Mülheim an der Ruhr), S. Demeshko, T. Y. Chen, F. Meyer (Georg-August-University, Göttingen)

Magneto-chiral dichroism in a one-dimensional assembly of helical dysprosium(III) single-molecule magnets

Magneto-Chiral Dichroism (MChD) is the differential absorption of unpolarised light by a chiral system in the presence of a magnetic field (B) collinear to a light wave vector (k). One of the main interests in MChD is driven by the possible optical readout of magnetic data using unpolarised light. One way to achieve this is to implement chirality into single molecule magnets (SMM) potentially making them MChD active. Since, MChD is sensitive to the magnetic state of the system, it should then be possible to trace the magnetic hysteresis of SMM using unpolarised light.

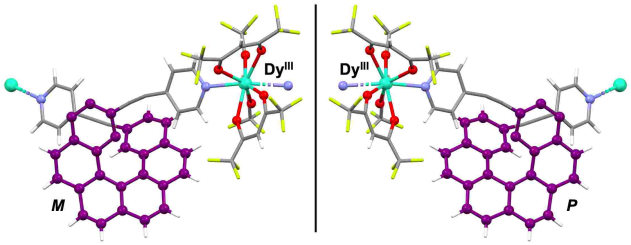

FIG. 62. *Molecular structure of* ***1****-(M) and* ***1****-(P).*

Due to their large spin-orbit coupling, chiral lanthanide complexes are among the best candidates to observe strong MChD, which was evidenced recently in a chiral helicene based Yb^{III} coordination polymer with record MChD signals observable up to room temperature. Therefore, since some of the best SMMs reported are Dy^{III} based, in this work, we studied the MChD of [Dy^{III}(H$_6$(py)$_2$)(hfac)$_3$]$_n$ [H$_6$(py)$_2$ = 2,15-bis(4-pyridyl)ethynylcarbo[6]helicene; hfac$^-$ = 1,1,1,5,5,5-hexafluoroacetylacetonate], **1**-(P) and **1**-(M) (figure 62), which are isostructural analogues to the previously reported Yb^{III} coordination polymer.

MChD measurements at $T = 4$ K with alternating B along k showed signals at different wavelengths (figure 63). They correspond to the f-f transitions between the ^{6}H$_{15/2}$ Dy^{III} ground state and spectroscopic levels derived from ^{6}F and/or ^{6}H terms. For the peaks at $\lambda = 1291$ nm and 1300 nm, the g_{MChD} dissymmetry factors at $B = 1$ T are 1.2% and 0.9% respectively, much are lower those observed in the Yb^{III} analogue, owing to the magnetic dipole forbidden nature of the transitions in Dy^{III} complexes.

The intensity of MChD signals at $\lambda = 455$ nm and 1291 nm closely follows the T dependence of magnetisation, highlighting the dominance of MChD C-term at low temperatures. In contrast with the magnetisation measured on microcrystalline sample, MChD measured on an oriented single crystal, is far from reaching saturation at 2 T (figure 64). This indicates that stronger MChD signals can be observed by pushing up the limits of the applied magnetic field.

To conclude, the investigation of the optical and magnetic properties of the chiral helicene based Dy^{III} coordination polymer showed the coexistence of both MChD and SMM behaviour. The system showed several MChD active transitions suitable to trace a magnetic hysteresis. These results point towards the development of Dy^{III} based chiral systems, with improved SMM properties for the realisation of optical readout of magnetic data using MChD.

For more details please see [Raju *et al.*, Inorg. Chem. **62**, 17583 (2023)].

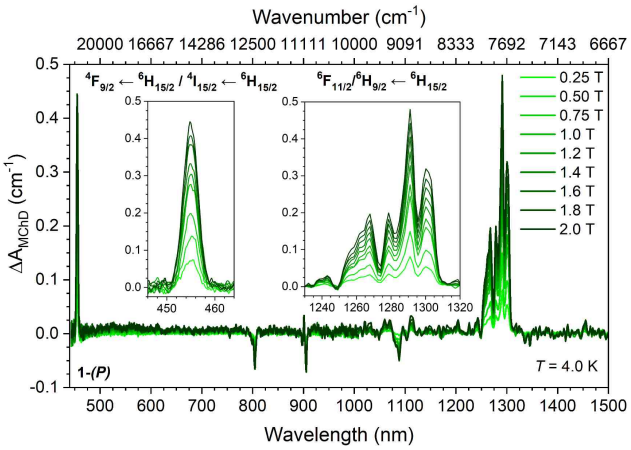

FIG. 63. *Magnetic field dependence of* ΔA_{MChD} *for* ***1****-(P).*

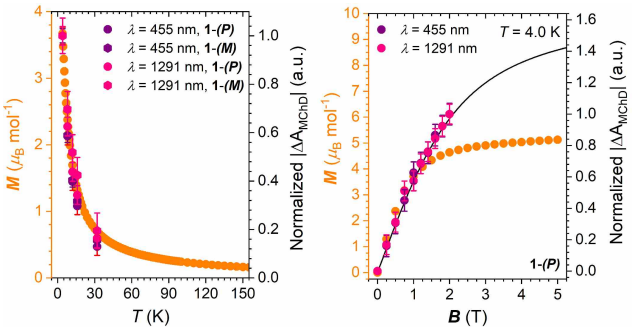

FIG. 64. *Temperature and magnetic field dependence of* ΔA_{MChD} *($\lambda = 455$ and 1291 nm) compared to the magnetization data. The black line is the simulated magnetization curve based on the Brillouin function assuming* $g_J = 4/3$ *and* $J = 15/2$.

M. S. Raju, I. Breslavetz, K. Paillot, G. L. J. A. Rikken, C. Train and M. Atzori
K. Dhbaibi, M. Grasser, V. Dorcet, O. Cador, B. Le Guennic, J. Crassous, F. Pointillart (University of Rennes)

Induced circular dichroism from helicoidal nano substrates to porphyrins - the role of chiral self-assembly

Induced circular dichroism (ICD) refers to the observation of natural optical activity in achiral objects through their interaction with chiral ones. One potential use of ICD is in the field of magneto-chiral dichroism (MChD), an optical effect where the absorption coefficient of a chiral system changes based on its handedness when irradiated by unpolarized light in the presence of an external magnetic field along the direction of the light propagation wavevector.

Here we explore the mechanism of interplay between ICD and MCD, inestigating nanocomposites fabricated using different chiral induction strategies on free base tetraphenylphorpyrinate-sulphate (TPPS), iron(III)- and copper(II)-TPPS and the naturally-occurring iron(III) porphyrin, hemin, deposited on silica chiral nanohelices (figure 65).

We have observed ICD and MCD of four achiral porphyrins associated to a nanometric helical silica platform. Three strategies of associating the nanohelices with the porphyrins were tested; direct surface grafting, ion exchange using hybrid helices, and drop-cast on inorganic helices.

The results clearly show that the silica helices can efficiently induce CD signals to all the studied porphyrin compounds. Nonetheless, depending on the interaction between the helices and the molecules, and on the nature of the porphyrin, the ICD varies considerably. These results are in contrast with the previous report of Ishii and collaborators who observed MChD in the Soret band for a chiral aggregation of TPPS. This can be explained by the extremely strong ICD observed in their system, 2000 mdeg compared to the 500 mdeg in our case. Furthermore, they observed a non-negligible MCD response at the Soret band.

Indeed, the formation of J-aggregates has been shown to play a key role and the DC technique which allowed the best head-to-tail stacking of the porphyrin led to the highest CD signals. For this reason, the highest ICD and MCD were observed with the free base porphyrin in the DC system. However, these strong ICD and MCD signals were not observed for the same transitions, Soret band for ICD and Q-band for MCD. Such an energy mismatch between the NCD- and MCD-active absorption bands are likely the origin of the absence of observable MChD signals.

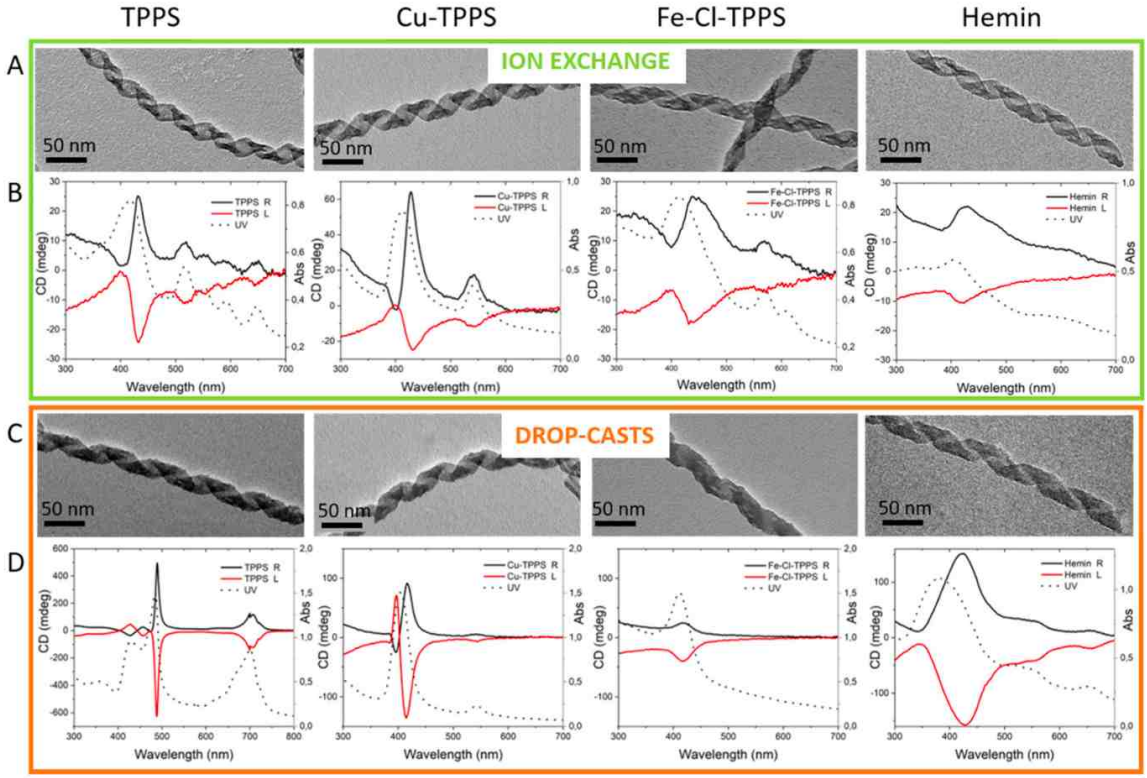

FIG. 65. *TEM images and their corresponding CD spectra and absorption spectra (solid and dashed lines, respectively) for the investigated nanocomposites with different chiral induction strategies.*

M. S. Raju, M. Atzori, C. Train, G.L.J.A. Rikken
G. Duroux, L. Robin, S. Buffière, Elodie Pardieu, Patrick Rosa, Elizabeth A. Hillard (ICMCB-CNRS, Bordeaux), P. Liu, E. Dols, M. De Souza Lima Mendes, A. Scalabre, S. Nlate, R. Oda, E. Pouget (CBMN-CNRS, Universitey of Bordeaux), T. Buffeteau (ISM-CNRS, University of Bordeaux)

Synthesis, characterization and magnetochemical study of cobalt, nickel and manganese coordination polymers

Three new polymeric compounds with the composition $[M_3(seb)_3(phen)_2]_n$, where M^{II} = Co**(1)**, Ni**(2)** and Mn**(3)**, seb = $(OOC\text{-}C_8H_{16}\text{-}COO)^{2-}$, phen = $C_{12}H_8N_2$ were synthesized and characterized by physical and physico-chemical methods. According to X-ray crystallography in the studied compounds the sebacic acid behaves as double anionic ligands, the charge balance and chemical composition are in agreement with the formation of isostructural trinuclear species ($P21/n$ space group) (see figure 66). Co1 is coordinated by six carboxylate oxygen atoms in a quite regular octahedral geometry. The coordination sphere of Co2 involves four carboxylate oxygen and two nitrogen atoms from o-phen ligand. Each trinuclear clusters are interconnected with six neighbours through sebacate linkers thus expanding in 3D coordination network. Assuming an isolated magnetic distribution of trinuclear cluster, the evolution of magnetic susceptibility data (figure 67) suggest antiferromagnetic interactions in the Mn_3 and Ni_3 cores and ferromagnetic interaction for Co_3 moiety.

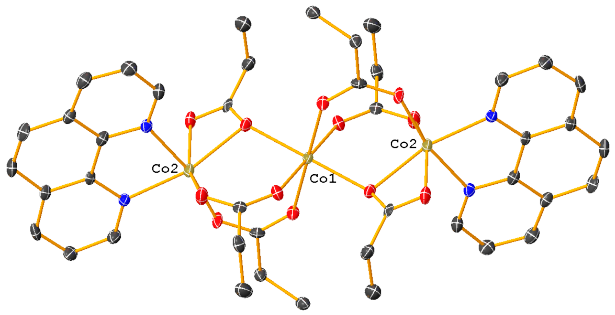

FIG. 66. *Crystal structure for $[Co_3(seb)_3(phen)_2]_n$,* ***(1)*** *(the hydrogen atoms were omitted for clarity).*

The temperature dependence of magnetic susceptibility and magnetization measurements for Mn was expressed using the isotropic spin Hamiltonian which include the exchange interaction (J) between three Mn(II) ions ($S_i = 5/2$) and the Zeeman splitting(g). The best fit of experimental data give $g = 2.039(1)$, $J = -1.43(1)\,\mathrm{cm}^{-1}$ and confirm the antiferromagnetic interaction in the Mn_3. In order to estimate the exchange parameters for the Ni_3 cluster the anisotropic spin Hamiltonian (J, D-axial and E-rhombic ZFS parameters, g-factor) was applied to analysis the magnetic data. The best fit corresponds to the values $J = 0.00(5)\,\mathrm{cm}^{-1}$, $g = 2.261(3)$, $D = 3.65(1)\,\mathrm{cm}^{-1}$ and $E = 0.30(7)\,\mathrm{cm}^{-1}$ indicating that decreasing of magnetic susceptibility at the low temperature is mostly represent the contribution of ZFS and the magnetic interaction is close to zero.

For strongly anisotropic Co_3 cluster the temperature dependence of magnetic susceptibility was analyzed by the following anisotropic spin Hamiltonian,

$$\hat{H} = -2J\left(\vec{\hat{S}}_1\vec{\hat{S}}_2 + \vec{\hat{S}}_2\vec{\hat{S}}_3\right) + \sigma\lambda\vec{\hat{L}}\vec{\hat{S}}\Sigma_{i=1}^{3}\left(\vec{\hat{L}}_{+_i}^2 - \vec{\hat{L}}_{-_i}^2\right) + \sigma^2 B_2^0\Sigma_{i=1}^{3}\left(3\vec{\hat{L}}_{z_i}^2 - \vec{\hat{L}}_i^2\right) + \tfrac{1}{2}B_2^2\Sigma_{i=1}^{3}\left(\vec{\hat{L}}_{+_i}^2 - \vec{\hat{L}}_{-_i}^2\right) + \mu_B\Sigma_{i=1}^{3}\left(\sigma\vec{\hat{L}}_{z_i} - 2\vec{\hat{S}}_i\right)H,$$

where $\sigma = -\frac{3}{2}\kappa$ is the combined orbital reduction parameters, λ is the spin orbital coupling parameters, B_2^0 is the axial distortion parameters and B_2^2 is the rhombic distortion parameters and J, similar to Ni_3 and Mn_3, reflect the isotropic interaction in the cluster Co_3.The obtained best fit parameters are $J = 0.32(6)\,\mathrm{cm}^{-1}$, $B_2^0 = 349(5)\,\mathrm{cm}^{-1}$ and $B_2^0 = 70.6(9)\,\mathrm{cm}^{-1}$ support the assumptions of presence ferromagnetic interactions in the reported Co_3 compound.

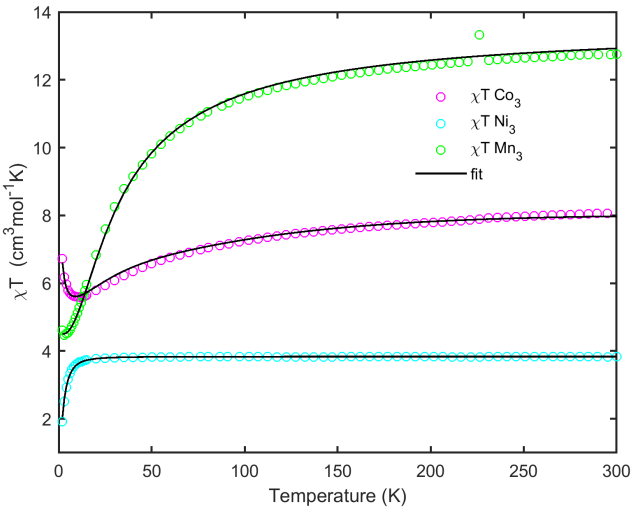

FIG. 67. *Temperature dependence of the $\chi_M T$ product for compounds Co_3* ***(1)****, Ni_3* ***(2)*** *and Mn_3* ***(3).***

For more details please see [Guzan *et al.*, Inorganica Chimica Acta **553**, 121526 (2023)].

G. Novitchi
O. Guzan, V. Lozan (Institute of Chemistry, Chisinau), S. Shova ("Petru Poni" Institute of Macromolecular Chemistry of the Romanian Academy, Iasi)

Applied Superconductivity

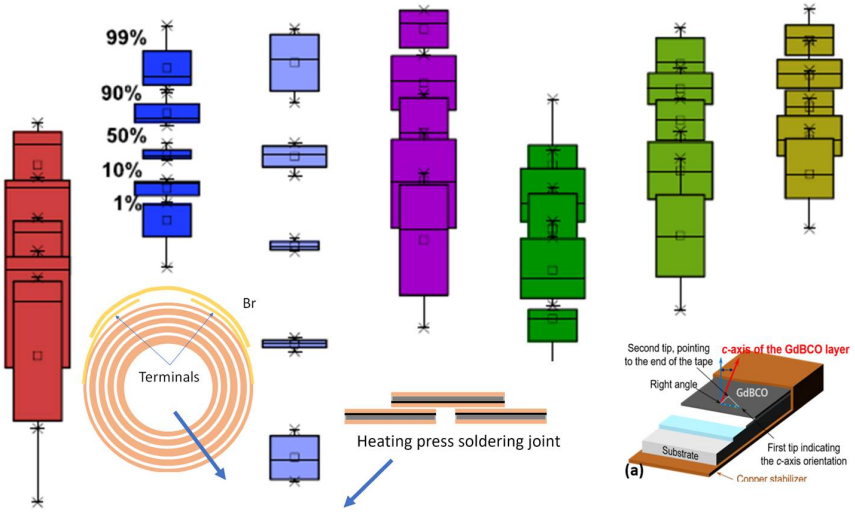

Delamination strength of REBCO HTS tapes

Rare earth barium copper oxide (REBCO) tape manufacturers have made efforts to reduce the production cost and improve the current density of their products. However, there are insufficient reports on the electrical and physical properties of these REBCO tapes under extreme conditions. Therefore, four REBCO products purchased in 2022 were tested (see figure 68): i) THEVA (TV); ii) Shanghai Superconductor Technology (SST); iii) Faraday Factory Japan (FFJ); and iv) Fujikura (FJK). Table I shows the specifications of the tapes. The width of all tapes was about 6 mm. The measured total thickness of three tapes were all approximately $\simeq 74-76\,\mu$m. In the case of FFJ, the measured total thickness values was about $\simeq 60-64\,\mu$m due to the thinner substrate.

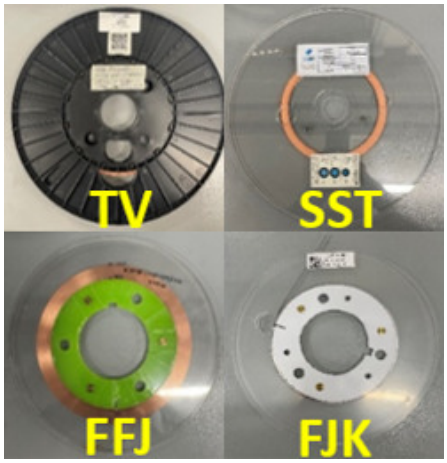

FIG. 68. *Spools of four REBCO tapes.*

TABLE I. Measured width and thicknesses of REBCO tapes. For the stabilizer the width is per side.

	Unit	TV	SST	FFJ	FJK
Width	[mm]	6 ± 0.1	6 ± 0.1	6 ± 0.1	6 ± 0.1
Stabilizer	[μm]	10 ± 2	10	10 ± 3	5
Substrate	[μm]	50	45	37 ± 0.3	50
Total	[μm]	74-76	74-77	60-64	73-75

For the construction of REBCO magnets, cutting, pre-tinning and soldering of the tapes are some tasks frequently performed. In addition, during these processes, polyimide tape is mainly used to protect and fix the REBCO tape, and removed after work. If the adhesion between the layers of the REBCO tapes is not sufficient during this process, delamination problems occur. Therefore, we checked the delamination strength as follows. The first step is to attach a polyimide tape on the REBCO tape and to remove it. The second is to cut the tape with scissors after pre-tinning the REBCO tape. Although this evaluation method is a rough one, it is a very practical approach for the construction of actual HTS magnets. In addition, to ensure reproducibility in evaluating tape delamination strength, we tested a minimum of eight samples from each company's product, selecting them from at least four conductor spools per company. Figure 69 and 70 show pictures of delaminated tapes. In the case of the first check (see figure 69), the tapes of three companies (TV, FFJ and FJK) were easily delaminated.

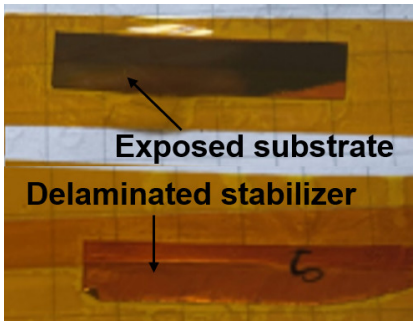

FIG. 69. *Delaminated tapes after removing polyimide.*

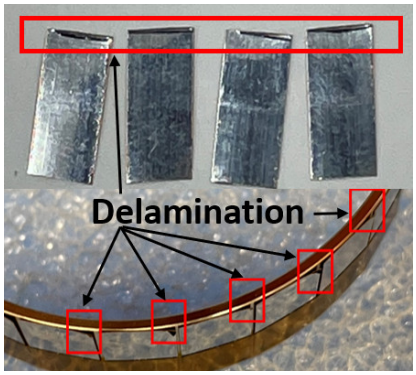

FIG. 70. *Delamination after cutting REBCO tapes.*

In the case of the second check (see figure 70), the tapes of two companies (TV and FFJ) were delaminated at the cut edge. In addition, even if the tapes did not delaminate immediately after cutting, it occurred several hours later, which means that the tapes with weak adhesion between layers are physically very unstable at the cutting area. Consequently, REBCO tapes of three companies, with the exception of SST tape, require an increase of their delamination strength. Recently, TV reported to us that they succeeded in developing a new tape with an improved delamination strength. The preliminary evaluation on samples of this new tape using Kapton showed no delamination; next, we are planning to evaluate the new TV tapes in the coil under high field.

J.B.Song, R. Raison, R. Pankow, J. Spitznagel, X. Chaud
A. Smara (THEVA GmbH, Ismaning)

Windability of REBCO HTS tapes

For construction of high magnetic field coils, it is very important to estimate the windability of the tapes because the coils require a large number of turns wound with high tension on a small diameter. Therefore, we undertake an evaluation of windability of four REBCO tapes. To construct double pancake (DP) coils for very-high-field magnet, the REBCO tapes were co-wound with a stainless-steel tape (Durnomag - 6 mm width and 30 μm thick) on a stainless-steel (SS) inner ring with a 50 mm diameter and a 1 mm thickness at a winding tension (WT) of 100 MPa. The reason for co-winding is to apply the advantages of the metal-as-insulator (MI) technique to the DP coils [Song *et al.*, IEEE Trans. Appl. Supercond. **32**, 4300206 (2022)]. If a deformation of the coil was noticeable at a WT of 100 MPa, the winding process was repeated by gradually reducing the WT to evaluate the maximum WT applicable with no deformation.

Figure 71 shows pictures of THEVA (TV) DP coils. The coils were wound uniformly without any deformation at a WT of 100 MPa, demonstrating that TV tape has good physical properties in terms of windability.

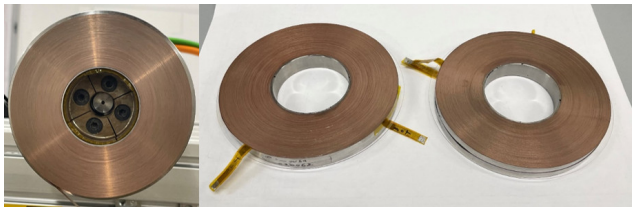

FIG. 71. *THEVA double pancake coils at a winding tension of 100 MPa*

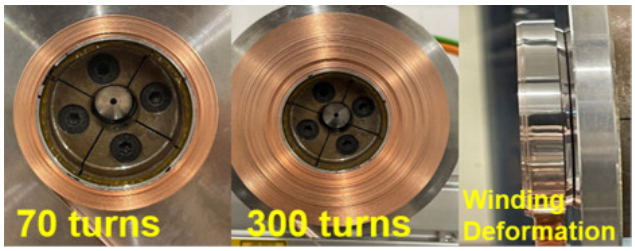

FIG. 72. *FFJ winding at a winding tension of 50 MPa*

Figure 72 shows the Faraday Factory Japan (FFJ) winding as the number of turns increases at a WT of 50 MPa. The FFJ coil not only had an uneven winding arrangement but was also deformed as the number of turns increased, even at a WT as low as 40 MPa. The reason for the winding deformation, as discussed with FFJ is probably due to the thinness (37∼40 μm) of the substrate and its geometry after electropolishing. Figure 73 shows a schematic drawing of FFJ tapes substrate after electropolishing. Since both ends of the tape width are thinner than the middle part, its thickness is inevitably asymmetrical when slitting the initial 12 mm width into 6 mm, which causes conical deformation of the windings. Moreover, in the case of 6 mm width tape cut from the center of 12 mm width tape for these tests (CNRS tape), the difference in thickness between the two ends of the tape is maximized (see figure 73a). Official products of FFJ are 4 mm and 12 mm wide tapes. FFJ will estimate the windability of their tape using a 6 mm width tape cut at both edges (see figure 73b) to use only the central part of the tape. This solution has of course a higher cost.

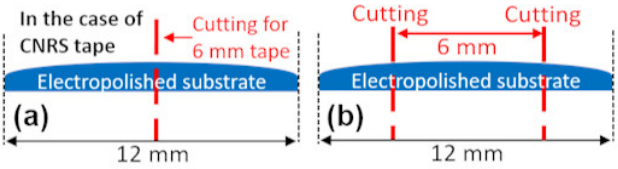

FIG. 73. *Schematic drawing of FFJ tapes substrate after electropolishing: Center cutting (a); and both-edge cutting (b) for 6 mm wide tape.*

Figure 74 shows pictures of Fujikura (FJK) windings. The coil shows good uniformity without any deformation during winding process. However, after unloading the coil from the winding machine, its outer part suddenly deformed at WTs from 100 MPa down to 50 MPa. To investigate the effect of edge direction on the windability, we performed the winding process again at a WT of 50 MPa after changing the edge direction of the tape. Deformation of the winding did not occur after unloading the coil (see figure 74b). However, after a $T = 77$ K test, the sapphire DP spacer maintained by the single-pancake coils slightly moved, which implies that it is difficult to completely prevent winding deformation.

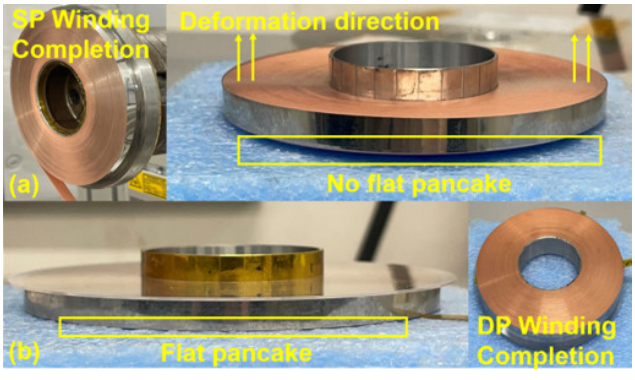

FIG. 74. *FJK coils before (a) and after (b) changing edge direction.*

J.B.Song, R. Raison, R. Pankow, J. Spitznagel, X. Chaud
A. Smara (THEVA GmbH, Ismaning), V. Petrykin (Faraday Factory Japan, Sagamihara), S. Richardson (Fujikura, Chessington, Surrey)

Windability of SST REBCO HTS tapes

Figure 75 shows pictures of Shanghai Superconductor Technology (SST) double pancake (DP) windings at a winding tension (WT) of 100 and 60 MPa. In the case of 100 MPa, the winding was well aligned without any issue up to 249 turns. At 250 turns, the winding was suddenly deformed into a conical shape (see the far right of figure 75a). At a WT reduced to 70 MPa, deformation of the winding could not be avoided. At a WT of 60 MPa, the SST DP coil was successfully wound without deformation. However, deformation of this winding occurs in some area during charging-discharging tests in a liquid nitrogen (LN_2) bath at 77 K in self-field (see figure 75b). Finally, at a WT of 50 MPa, the SST winding was free from deformation after winding process and LN_2 test.

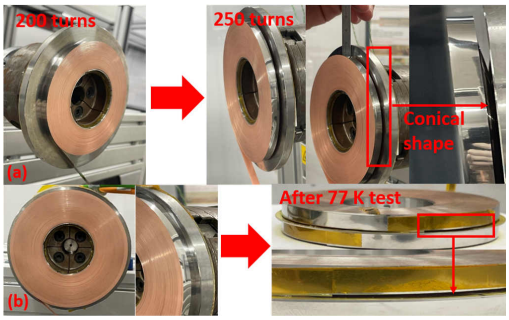

FIG. 75. *Deformed SST MI coils at winding tensions of (a) 100 MPa and (b) 60 MPa.*

SST investigated the causes of deformation of REBCO tapes at high WT and found that one edge is slightly thicker ($\sim 3\,\mu$m thickness difference) than the other. The reason for the thickness difference between the edges of SST tape is that (i) the substrate has a slight thickness variation along its width and (ii) the bottom end of tape tends to be thicker because the tape is placed vertically during copper-plating. Figure 76 illustrates the winding deformation using REBCO tapes with a different thickness between edges at high WT. When the thicker edge of the tape faces the bottom of the coil, the winding is denser than at the top of the coil wound with the thinner edge. If the coil is wound with a large number of turns at a high WT, the coil may suddenly deform into a conical shape at a certain number of turns exceeding the critical point of deformation. In contrast, if the thin edge is placed toward the bottom of the pancake, the deformation of the coil might be mitigated, but may also reduce winding uniformity. Moreover, even in this case, as the number of turns increases, the outer of the upper part of the coil wound with a thick edge may deform downward. Recently, SST notified us that they successfully reduced the difference in thickness between the edges of the tape to less than 1 μm, and that there was no deformation of DP coils using such tapes under the same winding conditions as ours. In the near future, we will evaluate the windability of SST's new products.

To estimate thickness uniformity of the REBCO tapes along longitudinal direction, the diameters of the windings were measured by vernier calipers. Figure 77 shows the conductor thickness estimated from the diameter of each winding. As seen in figure 77, the estimated thickness of THEVA tapes was within the measured thickness range of tapes, indicating that the tape has a consistent thickness in both the width and length directions of tape. In the case of SST, the evaluated tape thickness was slightly higher than the measured thickness because one edge of the tape is thicker than the other. In the case of Fujikura (FJK), the estimated thickness values of tapes were within the measured values for three spools. However, the estimated thickness of tape in one spool after winding was 70 μm, which is up to 5 μm thinner than the measured thickness. We discussed with FJK about this difference in thickness before and after winding, but the cause is not known yet. In the case of Faraday Factory Japan, it was difficult to evaluate the tape thickness by winding diameter because unevenness and deformation of the windings could not be prevented in these tests.

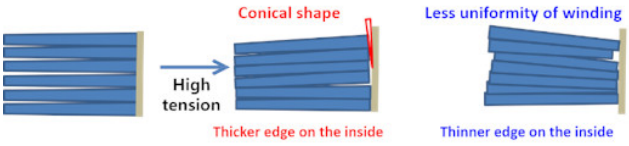

FIG. 76. *Illustration of winding deformation under WT using a tape with a difference of thickness between the edges.*

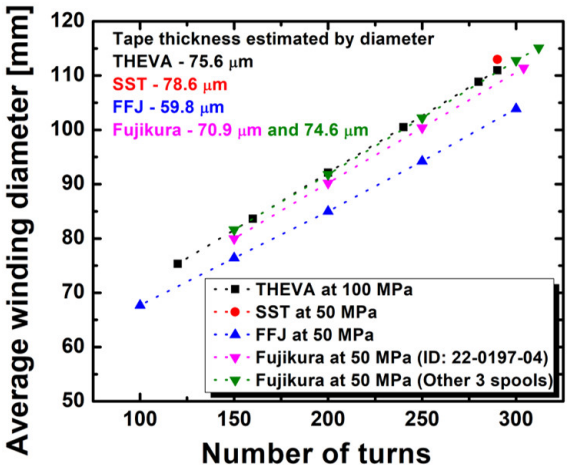

FIG. 77. *Number of turns versus winding diameter of DP coils wound with four REBCO tapes.*

J.B.Song, R. Raison, R. Pankow, J. Spitznagel, X. Chaud
B. Song (Shanghai Superconductor Technology)

Charging and quench tests of a THEVA prototype magnet at 4.2K

To estimate electrical performance and mechanical strength of REBCO windings, for the first test of the prototype magnet, THEVA (TV) double pancake (DP) coils were selected because TV tape was the only one that showed no deformation at a winding tension (WT) of 100 MPa among the four REBCO products. The two TV DP coils are stacked on a support structure that is intended to keep an uniaxial pressure of 10 MPa even after cooling at 4.2 K. TV tapes have a unique feature compared to other company's products; the c-axis of the REBCO layer is tilted by approximately 30 degrees with respect to the substrate normal due to the epitaxial growth of the REBCO layer on a biaxially textured MgO buffer layer. Therefore, when the DP coils were wound and stacked, we paid attention that TV windings have ab-planes approximating the direction of the field lines at the top and bottom. For a detailed description, figure 78 shows c-axis arrangement of the two DP coils.

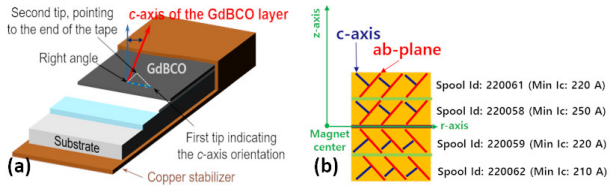

FIG. 78. *Schematic drawing of the TV REBCO tape (a) and half view of the assembled TV DP coils (b)*

Figure 79 shows the charging and quench test results of the model magnet at current ramp rate of 1 A/s under several external applied magnetic field (B_{ext}) at 4.2 K. To compare electrical performance of the TV magnet with regards to B_{ext}, test results of a previous magnet wound with a combo of TV and SuperPower tapes are added to figure 78(closed squares and closed triangles) [Song *et al.*, IEEE Trans. Appl. Supercond. **30** 4701806 (2022)].

Note that, except for the number of turns, the previous TV-SPo metal-as-insulator (MI) magnet has similar geometry as the TV magnet. In self-field tests at 4.2 K, the prototype magnet was charged up to 500 A and the previous test magnet was charged up to 555 A. The magnetic field (8.5 T) generated by the TV magnet is higher than the field (7.9 T) of the previous test magnet because of the higher number of turns. At B_{ext} = 5 T and 10 T, the TV magnet was successfully charged up to 500 A, whereas a quench of the previous test magnet occurred at 455 A and 375 A at B_{ext} = 5 T and 10 T respectively, even though it produces a lower magnetic field (5.3 T at B_{ext} = 10 T) compared to the TV magnet (8.4 T at B_{ext} = 10 T). This result demonstrates that the new TV tape has improved electrical performances under high field. At B_{ext} = 15 T, a quench of the TV magnet finally occurred at 405 A, after which the magnet was gradually degraded by repeated quenching events (see closed circle and red arrow).

To find the cause of the degradation, the magnet was disassembled and unwound. There were no damage or signs of deformation of the TV windings, however, the HTS pieces and tape for internal and external electrical junctions were delaminated and kinked (see figure 80), especially in the internal junction of the top DP coil. To confirm whether the TV tapes inside the windings were damaged or not, their critical current (I_c) distribution were estimated again by the Tapestar quality control device at the TV company and compared with measurements performed in similar condition prior to the delivery of the tapes. The I_c distributions of each tape before and after quench events are similar, which implies that the cause of the magnet degradation is from damaged junctions probably due to the weak delamination strength of the tape. In other words, THEVA tape not only has good physical properties for high pressure windings, but also has high electrical performance under external magnetic fields. However, its delamination strength should be improved for its use in HTS windings. Recently, TV sent a new tape with an improved delamination strength to us. The preliminary evaluation on samples of this new tape using Kapton showed no delamination.

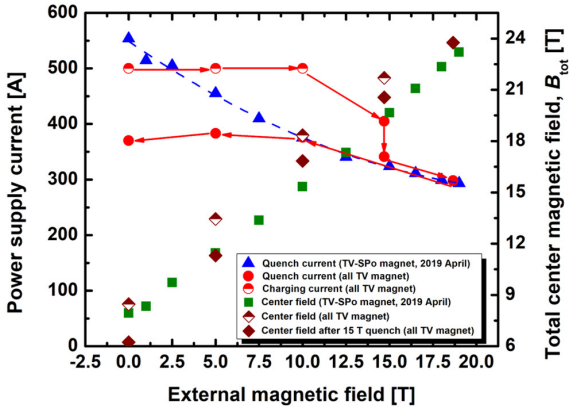

FIG. 79. *Test results of THEVA-SuperPower and all THEVA model magnets under various B_{ext} at 4.2 K*

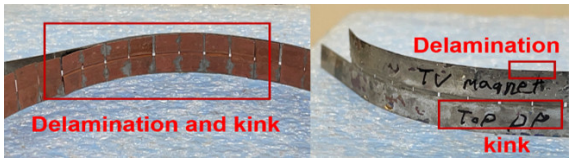

FIG. 80. *Internal electrical junctions between single pancake coils after quench events.*

J.B.Song, R. Raison, R. Pankow, J. Spitznagel, F. Debray, X. Chaud
P. Fazilleau, T. Lécrevisse (DACM, IRFU, CEA, Gif sur Yvette), A. Smara (THEVA GmbH, Ismaning)

Joint characteristics and in-field performance of REBCO HTS tapes

For the construction of HTS magnets many electrical junctions have to be made to connect the different pancakes or double-pancakes (DP). Therefore, we investigated a large number of junctions for REBCO tapes of four companies to optimize (minimize) the resistance without degrading the critical current (I_c). To evaluate the junction properties of each tape, the samples were tested at 77 K in a liquid nitrogen (LN_2) bath in self-field (see figure 81). Table II lists test results of joining samples. The maximum joint resistance values of all samples were less than 17 nΩ and their I_c values were not degraded at least at 77 K in self-field. In other words, all tapes show good electrical performance for the joint.

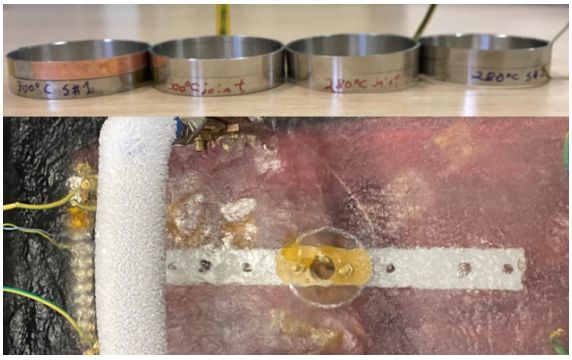

FIG. 81. *Fabricated and tested joints of REBCO HTS tapes.*

TABLE II. Test results of REBCO tape joints measured at 77 K in self-field.

	Unit	TV	SST	FFJ	FJK
Min.I_c of HTS pieces	[A]	130	224	272	200
Min.I_c of HTS conductor	[A]	220	224	179	200
Max. joint resistance	[nΩ]	6.0	16.8	6.5	11.3
Surface resistivity	[nΩ·cm^2]	24.2	60.6	25.7	44.8
I_c of the samples	[A]	218	263	258	274

Figure 82 shows some lift factors of REBCO tapes under various fields perpendicular to the ab-plane ($B_\perp$). In the particular case of THEVA (TV), the c-axis of the REBCO layer is tilted by approximately 30 degrees with respect to the substrate normal [Song *et al.*, IEEE Trans. Appl. Supercond. **30** 4701806 (2022)]. As shown in figure 82, the TV tape shows the highest performance. Figure 83 shows current carrying capability (CCC) of the tapes per unit width under various $B_\perp$. The critical current density of all REBCO tapes was over 1000 A/mm^2 under a $B_\perp$ of 30 T at 4.2 K, which implies that all REBCO tapes are suitable as conductors for fabricating of very-high-field magnet in terms of electrical properties. At this level of current density, the performance of the magnets is limited by the mechanical properties. The CCC of TV REBCO tape was evaluated by reflecting the lift factor to the average I_c(77 K) of purchased 6 mm width tapes. Meanwhile, Faraday Factory Japan (FFJ) informed us that their evaluation results of CCC differ from our test results. Although they measured the CCC of their tape up to a $B_\perp$ of 13 T, the tape shows approximately 14.3% better performance under a $B_\perp$ of 30 T compared to our result (if their result is extrapolated). The reason why our measurement was lower than that of FFJ is probably because the tape may be mechanically damaged under high field due to its thinner substrate.

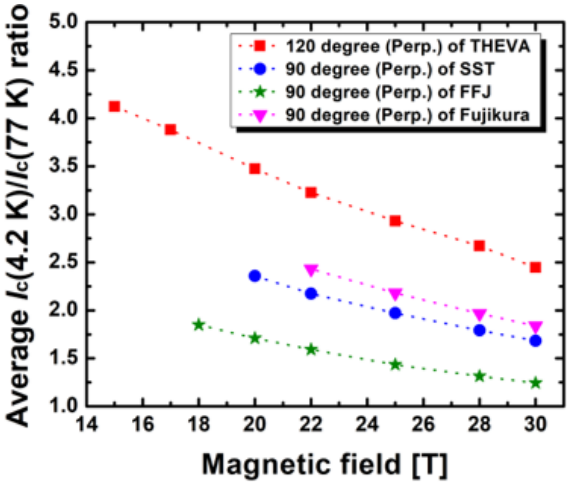

FIG. 82. *Lift factor of the tapes under various perpendicular fields from ab plane.*

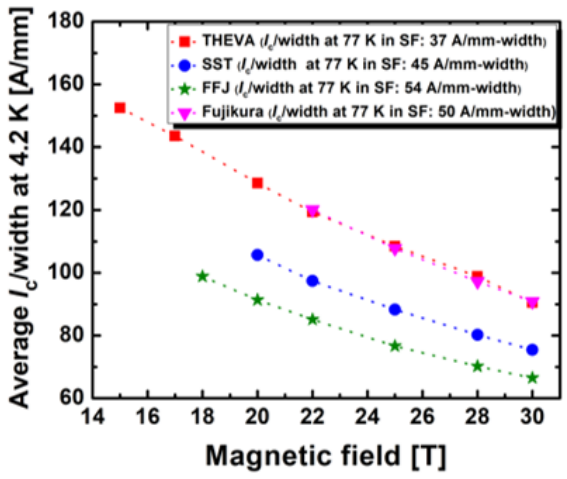

FIG. 83. *Current carrying capability of the tapes per unit width under various perpendicular fields from ab-plane.*

J.B.Song, R. Pankow, F. Debray, X. Chaud
R. Huiskamp, M. Dhallé (University of Twente, AE Enschede), V. Petrykin (Faraday Factory Japan, Sagamihara)

Magnetization of HTS double-pancake coils with soldered joints

High temperature superconductor (HTS) double-pancake coils, compared to HTS-stacked ring magnets [Liao *et al.*, J. Appl. Phys. **134**, 083902 (2023)], offer better symmetry in field distribution due to their regular shape. These coils, made with commercial HTS tapes, can generate strong magnetic fields with high current. However, they often need external power sources, leading to heat loads that limit current transport, affecting high-current operations and magnetic field stability. Recent flux pump developments allow for non-contact flux injection, facilitating direct current generation. Despite these advances, limitations in coil turns and magnetic field strength persist. This study exams an HTS double-pancake coil sample magnetized through field cooling, assessing its potential as a trapped field magnet. It has soldered joints which can maintain closed-loop current in the coil.

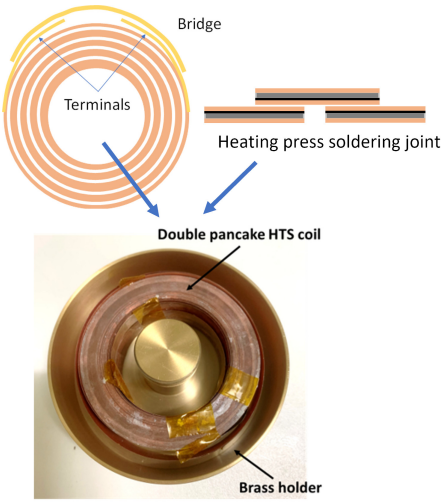

FIG. 84. *Finished HTS double-pancake coil*

Bridge-type soldering process were employed for the joints and the resistance of the joints at 77 K was measured to be around 12 nΩ. The HTS coil was impregnated with paraffin wax in the brass sample holder. The finished HTS coil is shown in figure 84. A cryogenic Hall sensor was placed in the centre of the sample for measuring the central field during and after magnetization.

The central fields during 1.07 T and 4.5 T field cooling magnetization are shown in figure 85 and figure 86. The central field commences its upward trajectory as the applied field starts its decrement and continues to rise until the applied field is zero. Following the end of the external field's decrement, there is a gradual decline in the central field, caused by the combined effects of flux relaxation and the resistive attributes of the joints. In figure 86, the central field attains its peak at approximately 4.6 T before it witnesses a consistent decline. A temporal progression of 30 minutes witnesses the central field's decay to 4.55 T, a value which still exceeds the originally applied 4.5 T.

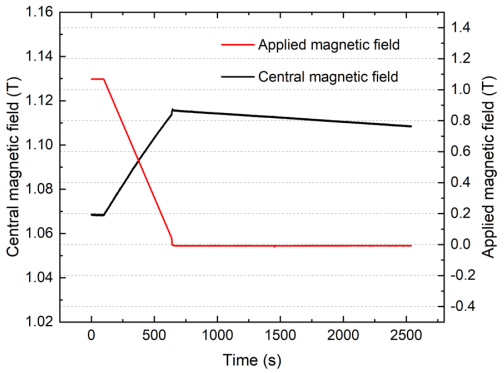

FIG. 85. *Central field of the HTS double-pancake coil during 1.07 T magnetization.*

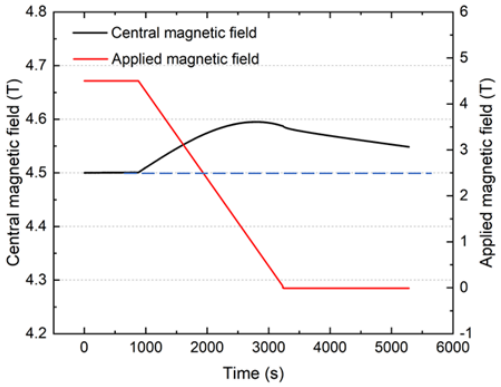

FIG. 86. *Central field of the HTS double-pancake coil during 4.5 T magnetization.*

When the external field is completely removed, the closed-loop HTS double-pancake coil can be seen as an RL circuit that is short-circuited, so the central field can be calculated based on,

$$F_c(t) = A_0 \exp\left(-\frac{Rt}{L}\right),$$

where $F_c(t)$ is the time-dependent central trapped field of the HTS coil and A_0 is the initial field during field decay. According to the equation, the resistance of the joints under liquid helium is calculated to be 2 nΩ. Besides, the decay rate can also be calculated. After 3 hours, the central field decayed to 4.4 T, a 3.9% reduction. With higher inductance (more turns) and lower resistance, the decay rate can be further reduced. This study underscores the potential and challenges associated with HTS double-pancake coils and suggests references for further research and optimizations.

X. Chaud, J.B. Song
H. Liao, W. Yuan, M. Zhang (University of Strathclyde)

Effects of the oxygen source configuration on the superconducting properties of internally-oxidized internal-Sn Nb_3Sn wires

The Nb_3Sn superconductor currently stands as the favored choice for the conductor in the upcoming generation of high field accelerator magnets. A notable instance is the high luminosity upgrade of the large Hadron collider (HL-LHC) at the European organization for nuclear research (CERN). Within this initiative, the aim involves the installation of high-field large-aperture Nb_3Sn quadrupole magnets in the interaction region, featuring a peak field on the conductor reaching 12 T. Achieving this ambitious goal necessitated the development of Nb_3Sn wires with a non-Cu J_c, specifically the critical current (J_c) divided by the wire's non-Cu area (comprising Nb_3Sn, residual bronze, and barriers), attaining 2450 A mm^{-2} at 4.2 K and 12 T.

CERN is concurrently engaged in a study for a prospective proton-proton collider known as the future circular collider (FCC-hh). This envisioned collider boasts a $\simeq$ 100 km circumference ring equipped with 16 T Nb_3Sn dipole magnets, resulting in a collision energy of 100 TeV. To meet the imperative of attaining a dipole field of 16 T in a compact and economically viable magnet, the non-Cu J_c target for the Nb3Sn wires is set at 1500 A mm^{-2} at 4.2 K and 16 T. By way of comparison, under analogous conditions, the wires developed for the HL-LHC upgrade can manifest a non-Cu J_c value as high as 1250 A mm^{-2} at 4.2 K and 16 T.

In the context of a collaborative effort between UNIGE and CERN, this study presents the findings of an investigation into internal Sn wires with an internal oxide source (OS) aimed at enhancing the superconducting properties of Nb_3Sn. The research explores methodologies to incorporate an internal OS into a simplified rod-in-tube (RIT) wire, mimicking a subelement of RIT wires with a reduced number of Nb-alloy filaments. The absence of powder in the design of current RIT wires necessitates preliminary studies to assess the effects of powder OS in different layouts on wire deformability/fabrication and superconducting properties.

Successfully manufacturing 12-filament rod-in-tube Nb_3Sn wires with oxide nanoparticles formed by the internal oxidation method, the study employed Nb-7.5 wt%Ta-1 wt%Zr and Nb-7.5 wt%Ta-2 wt% Hf alloys along with oxygen sources (OSs) in two different configurations in the core of Nb filaments (coreOS) and at the boundary between the filaments and the Cu tube (annularOS). This rapid research and development activity allowed for an in-depth investigation into the effects on the superconducting properties concerning the position of the OS relative to the Nb_3Sn formation front.

Figure 87 illustrates the ranges of B_{c2} values at different criteria measured on multiple samples of each wire type. Experimental data indicate that $B_{c2}(4.2)$ K calculated using the 99% criterion increases to 29.2 and 29.3 T for Zr-annularOS and Hf-annularOS samples, surpassing by more than 1 T the B_{c2} value of 28 T for a sample fabricated with the same procedure and using Nb-7.5 wt%Ta alloy (NbTa-noOS).

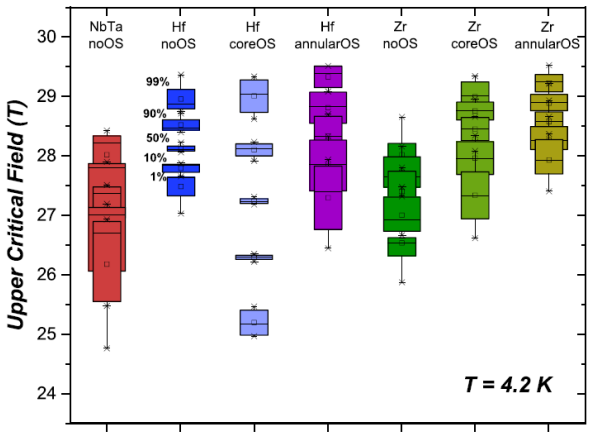

FIG. 87. *B_{c2} values at temperature $T = 4.2$ K values of several samples of each wire estimated using with different criteria (from top to bottom: 99%, 90%, 50%, 10%, 1%). Comparison with wire NbTa-noOS, is given.*

The simultaneous presence of the OS and of Hf or Zr reduced the average Nb_3Sn grain size to around 50 nm, resulting in an enhancement of the layer critical current density (J_c) up to 3000 A mm^{-2} at 4.2 K and 16 T for the Hf-annularOS wire. Samples manufactured with an OS exhibit a shift toward higher reduced magnetic fields of the position of the maximum in pinning-force density. This shift is more pronounced when SnO_2 is added in the annularOS configuration and for the Hf-containing samples. This enhanced pinning at higher magnetic field levels proves beneficial for high-field magnet applications.

For more information, please see [Bovone *et al.*, Supercond. Sci. Technol. **36** 095018 (2023)].

D. LeBoeuf
G. Bovone, F. Buta, F. Lonardo, T. Bagni, M. Bonura, C. Senatore (University of Geneva)

Magneto-Science

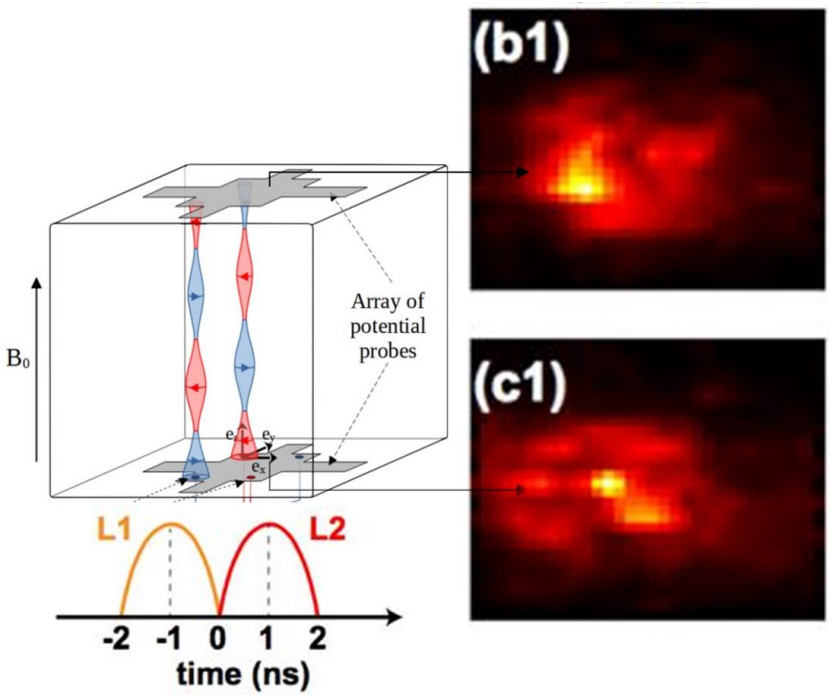

Laser pulse propagation in a magnetized under-dense plasma

The propagation and energy coupling of intense laser beams in plasmas are critical issues in laser-driven inertial confinement fusion (ICF). Applying magnetic fields to such a setup has been evoked to enhance fuel confinement and heating, and mitigate laser energy losses. For ICF, it is critical that the maximum laser energy possible is coupled, either directly to the fuel in direct-drive or to the hohlraum wall in indirect-drive, in a spatially homogeneous manner, as the laser's imprint seeds hydrodynamic instabilities that limit fuel compression.

Laser-plasma interaction (LPI) can be either beneficial to ICF, *e.g.* when spatially smoothing the laser energy distribution, or detrimental, *e.g.* by conversely causing spikes in the laser pattern through self-focusing, or by inducing energy loss through stimulated Raman and Brillouin scattering (SRS and SBS, respectively).

In this context, we have recently been able to perform experimental measurements demonstrating improved transmission and increased smoothing of a high-power laser beam propagating in an underdense magnetized plasma.

To assess the impact of magnetization on laser propagation and coupling, we experimentally explored the dynamics of a single speckle laser beam propagating through pre-ionized under-dense plasma targets. For this setup, a large-scale and strong (20 T) transverse magnetic field was applied. This is used as a proxy for the indirect-drive ICF hohlraums environment.

As shown in figure 88, we could show, via time-resolved and two-dimensional (2D) space-resolved transverse imaging of the transmitted beam, that magnetization of the plasmas allowed enhanced energy transmission and improved beam smoothing in a magnetized plasma, which is favourable in terms of illumination inhomogeneity of the final target. This is due to the magnetization favouring a lower electron density and higher electron temperature, thus leading to a lower absorption (via inverse Bremsstrahlung).

Additionally, measurements of the backscattered SRS indicate an increased signal level at different plasma densities in the magnetized case. 2D particle-in-cell (PIC) simulations confirm this trend and reveal that hot electron confinement (with energies up to 100 keV) is responsible for this increase, which will reduce preheating of an ICF target.

For more details please see [Yao *et al.*, Phys. Rev. Lett. **130**, 265101 (2023)].

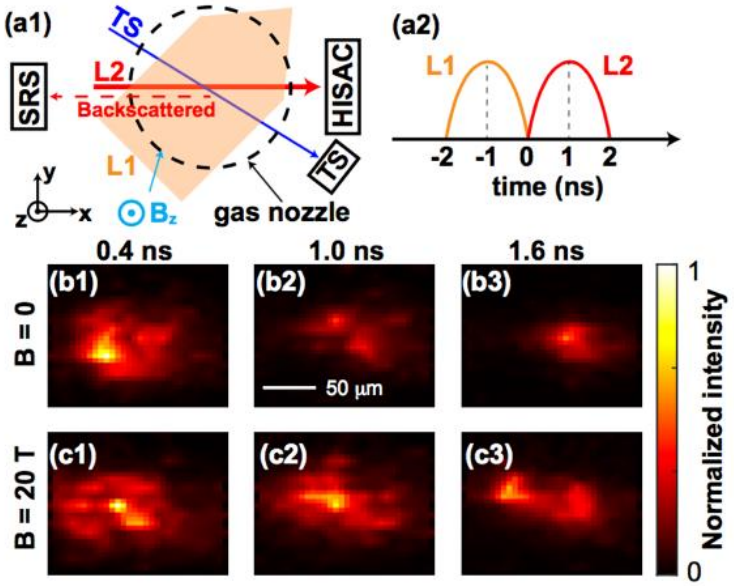

FIG. 88. *(a1) Schematic displaying the experimental configuration (top view). (a2) Time sequence of the pre-heating (L1) and interaction (L2) beams. (b-c) Temporal snapshots from the HISAC diagnostic, displaying transmitted L2 laser light, for a peak electron density* $ne = 0.04nc$ *and magnetic field* $B = 0$ *and 20 T, respectively. All panels are normalized by their respective maximum intensity and share the same colormap on the right.*

J. Béard

W. Yao, J.-R Marquès, K. Burdonov, A. Castan, T. Gangolf, L. Lancia, J. Fuchs (LULI-CNRS, CEA, UPMC, Palaiseau), A. Higginson (University of California San Diego), P. Antici (INRS-EMT, Varennes), M. Borghesi, B. Coleman (Queen's University Belfast), A. Ciardi (Sorbonne Université, Paris), L. Gremillet, P. Loiseau (CEA-DAM-DIF, Arpajon), S.N. Chen (NIPNE, Bucharest-Magurele), E. d'Humières, X. Ribeyre (University of Bordeaux), B. Khiar (ONERA, Palaiseau), A. Soloviev, M. Starodubtsev (IAP-RAS, Nizhny Novgorod), Q. Wang (IAPCM, Beijing)

Grenoble axion haloscopes - from BabyGrAHal to GrAHal

Particle physics is not confined to the high energies, the low energy frontier *i.e.*, the eV/sub-eV range, is also promising for major discoveries. One of the emblematic particles for this new physics is the axion, a pseudo-scalar predicted to solve the fundamental problem of the apparent non-violation of the CP symmetry by the strong interaction. This particle could also be the main dark matter component of our universe and is one of the leading candidates and rare non-supersymmetric ones. In addition, it has been recently proposed that, using graviton to photon conversion in a magnetic field, haloscopes can also be used to search for gravitational waves (GW) with frequencies above the kHz range, *i.e.*, out of reach of LIGO-Virgo-KAGRA interferometers.

This innovative approach has the potential to revolutionize cosmology by providing observational insights into primordial cosmology or new sources of GW. Within the scientific scope of the GrAHal experiments, attention is also drawn to Chameleons and dark photons. The former, a hypothetical scalar particle with effective mass depending of its local matter environment, appears in several theories beyond the standard model and could be responsible for dark energy. The latter, a hidden gauge vector boson also common to many extensions of the standard model, could also be a component of the dark matter.

Investigating the ultra-low energy frontier require specific developments of various technologies, including cryogenics, high magnetic field environments, microwave engineering, ultra-low noise receivers, and amplifiers, to build haloscopes. This type of experiment initially proposed by P. Sikivie in 1983, was designed to detect photon conversion in strong magnetic field of any feebly interacting particles crossing the Earth. Interestingly, all the required experimental tools are common to those generally used in condensed matter physics. In this context, the synergy between four main laboratories in this collaboration are bringing together key expertise to build and operate haloscopes for axion, ALPs, Chameleon and GW searches with unprecedented sensitivity.

Using our modular high-field hybrid magnet associated with state-of-the-art high quality factor RF cavities, with quantum amplifiers and ultra-low temperature cryogenics, GrAHal will reach beyond state-of-the-art sensitivities opening new opportunities for major discoveries within the axion/axion like particles (ALPs) mass range 1-150 eV.

First results of the GrAHal's experimental run can be found in Grenet *et al.* arxiv:2110.14406v1. Two main components are present in the experimental part of this project: BabyGrAHal and GrAHal. BabyGrAHal is composed of two haloscopes targeting the frequency range 4-7 GHz; a first one is already in operation at 4.4 K and the second one is in construction within an existing 14 T superconducting magnet equipped with a 50 mK dilution refrigerator.

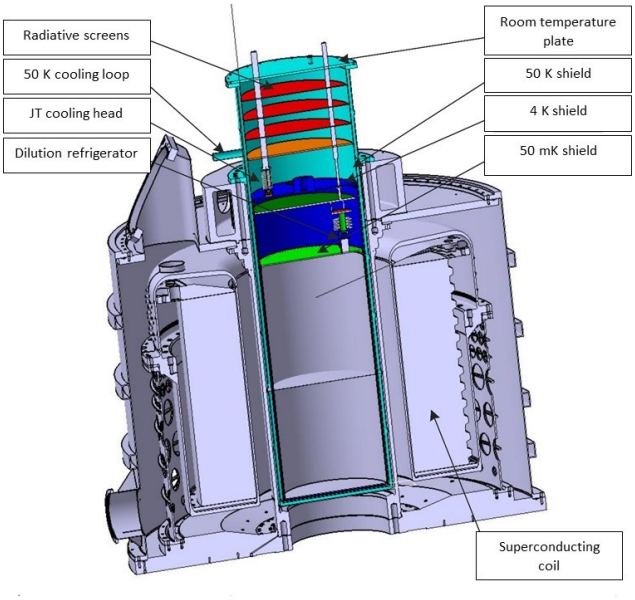

FIG. 89. *Schematic of the GrAHal-CAPP haloscope cryostat within the large bore SC of the hybrid magnet with thermal shields at 50 mK, 4 K and 50 K.*

For GrAHal-CAPP, we have focused to the design of a low frequency haloscope for the 300-600 MHZ range. Using the state-of-the-art magnet provided by the 9 T superconducting "outsert" coil of the hybrid magnet, a haloscope with unprecedented sensibility, *i.e.*, reaching the Dine-Fischler-Srednicki-Zhitnitskii (DFSZ) limit, can be built. The RF cavity of 700 mm diameter will be integrated inside the 50 mK shield of the cryostat shown in figure 89 and will be connected to a first dilution refrigerator. A second dilution refrigerator will be dedicated to the cooling to 100 mK of the RF electronic components, including the near quantum noise amplifier foreseen for the phase-2. The RF cavity will be made out of Cu with a quality factor in the range of few 10^5. A dedicated tuning mechanism based on a piezoelectric motor will be developed and combined with various tie rod diameters to cover the whole targeted frequency range. All these developments are based on proven technologies.

R. Pfister, P. Pugnat
R. Ballou, C. Bruyère, P. Camus, T. Grenet, P. Perrier, N. Roch, A. Talermin, J. Vessaire (Institut Néel, CNRS, University Grenoble Alpes), A. Barrau, K. Martineau, J. Quevillon, C. Smith (LPSC, CNRS, Univiversity Grenoble Alpes) H. Byun, W. Chung, O. Kwon, Y. K. Semertzidis (CAPP/IBS, KAIST, Daejeon)

Characterisation of the birefringent waveplate associated to layers of a high reflectivity interferential mirror

Following our work on the optical noise affecting vacuum magnetic birefringence experiments [Agil *et al.*, Eur. Phys. J. D **76**, 192 (2022)], we devoted a large part of 2023 to reducing this noise in our experiment, the *Biréfrigence Magnétique du Vide* (BMV) experiment, to improve its sensitivity.

The BMV experiment is dedicated to test a prediction of quantum electrodynamics (QED) which states that in vacuum and in the presence of a magnetic field whose direction is transverse to the propagation of light, the speed of light polarised in the direction of the field and orthogonally to it are different. A birefringence thus appear characterized by a difference of refractive index along these two directions $\Delta n = k_{\mathrm{CM}} B^2$ with $k_{\mathrm{CM}} = 4 \times 10^{-24}\,\mathrm{T}^{-2}$ the so-called Cotton-Mouton constant predicted for vacuum by QED. Experimentally, this birefringence is detected by the ellipticity acquired by a beam of light propagating through vacuum under a transverse magnetic field. The BMV experiment uses a Fabry-Perot cavity to increase the acquired ellipticity by trapping the light inside the magnetic field region.

We previously showed that, in the absence of a magnetic pulse, our experiment is limited by a noise originating from the birefringent nature of the optical cavity itself. To lower this noise, a possibility is to use birefringenceless mirrors. We therefore explored this prospect in collaboration with Safran Electronics & Defense, a leading manufacturer of high reflectivity interferential mirrors.

Interferential mirrors consist of a stack of alternating dielectric layers of high and low refractive indices deposited on a substrate. The thickness of the layers are chosen so that the beams reflected at each interface observe constructive interference. The experimental phase retardation of this kind of stacked layers decreases with its reflectivity *i.e.* with the number of layers deposited. To explain this observation, a proposed model suggests that stresses between the substrate and the first deposited layer are the cause of the observe birefringence. With added layers the birefringence decreases because the stresses relax.

We set out to verify this empirical trend as, according to it, a mirror with a lower birefringence could be fabricated with a high number of deposited layers. We therefore undertook a large study of the phase retardation of interferential mirrors as a function of the number of deposited layers and of the nature of the substrate. This work was the object of a publication [Agil *et al.*, Eur. Phys. J. Appl. Phys. **98**, 61 (2023)] and was carried out in two stages. In the first stage Safran manufactured 20 mirrors under the same conditions and we measured the phase retardation δ_1 and orientation of the optical axes θ_1 of all of them. Then, Safran deposited two additional pairs of layers on each mirrors under the same conditions as before, in particular with the same orientation, and we measured the phase retardation once again.

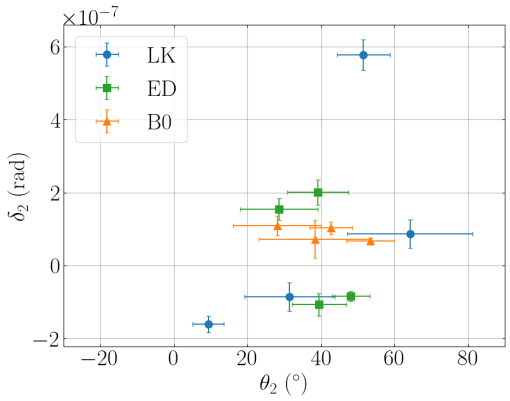

FIG. 90. *Phase retardation per reflection of the additional layers δ_2 as a function of the direction of their optical axes θ_2. Results for mirrors of fused silica substrate from Laseroptik "LK", and from Edmund Optics "ED", and in Zerodur substrate "B0" are presented.*

The first series of measurements showed the importance of the surface quality of the substrate before deposition as the substrates polished by Safran showed a lower phase retardation than other mirrors. Moreover, the measured orientation of the optical axes of all the mirrors are grouped around $\theta \sim 40°$ indicating a preferred direction during the mirror deposition precess.

With the additional layers we observed an increase in reflectivity as expected. As a matter of fact, we obtained never reached before reflectivities for our wavelength. As far as the phase retardation is concerned, we did observe a decrease of the intrinsic birefringence for some mirrors, however, we also saw an increase for others, as a whole staying around $\delta \sim 2\times10^{-7}$ rad, in contradiction with the empirical trend. Also, the orientation of the optical axes of the mirrors moved when the additional layers were deposited. Both of these facts are a clear indication that a birefringent waveplate was added along the additional layers, and with our measurement we can retrieve its contribution for each mirror, shown in figure 90, all around $|\delta_2| \sim 10^{-7}$ rad.

Our work is the first direct measurement of the birefringence of dielectric layers. Using a computational model, we conclude that our mirrors are currently at the lowest phase retardation possible. To control and eventually erase mirror phase retardation, further work is needed to understand the origin of the favoured direction during layer deposition.

J. Agil, S. George, J. Billette, J.-M. Lagarrigue, J. Béard, T. Moraine, R. Battesti and C. Rizzo
B. Letourneur (Safran Electronics & Defense, Montluçon)

On the speed of light in a vacuum in the presence of a magnetic field

The *Biréfrigence Magnétique du Vide* (BMV) experiment is designed to determine if the speed of light in a vacuum changes when a magnetic field in present. As of today, the experimental answer to this fundamental question remains unanswered, even though it has been stated in modern terms for more than a century. To fully understand the importance of such a question in physics, we undertook a review of the main facts and concepts from a historical point of view.

In our article [Agil *et al.*, Eur. Phys. J. H **48**, 2 (2023)], we start with the first descriptions of light and magnetism in treatises of ancient philosophers such as Euclid's *Optics* and Plato's *Ion*, and we expose the point of view of Aristotle on the non-existence of vacuum in his book *Physics*. We jump to the 17th century where developments in our three topics are found. Indeed, at the beginning of this century Gilbert's *De magnete* was published, this book can be seen as the foundation of the science of magnetism. At the middle of the century, Torricelli seemingly achieved a pneumatic vacuum thanks to his famous experiment. In the addition of discovering atmospheric pressure, this experiment relighted debates on the existence of vacuum. Among thinkers of the time, the common assumption is that in a vacuum movement as well as light propagation is impossible and a "subtle matter" needs to be always present. The concept of the "ether" entered science.

From this point on tremendous efforts were made by scientist both theoretically and experimentally to clarify the properties of this substance filling the whole cosmos. In the 18th century, soon after the discovery that light can be polarized, the first magneto-optical effects was uncovered by Faraday. This was considered a clear indication of the connection between light and magnetism. Subsequently confirmed by the successful description of light as electromagnetic waves by Maxwell in a theory where ether is put forward to explain light waves propagation. Then, a long series of experiments up to the 19th century tried to probe the existence of ether by propagating light near electric or magnetic fields and measuring a variation on its speed using interferential methods. The assumption was that electric and magnetic fields can be described respectively as a translation and a rotation of ether, and because ether is the propagation medium of light, a movement of ether was expected to induced a variation of the speed of light, but none was detected.

It was actually experiments looking for a movement of ether without electromagnetic fields that gave the final answer. Fizeau's experiment found that the speed of light in a moving medium changes by a value in between the speed at rest and the sum of this speed and the speed of the moving medium in which the light is propagating. This was interpreted as a partial drag of the ether by the movement of matter. This contradicted the result of another experiment by Michelson and Morley which found that the speed of light is the same no matter the direction probed with respect to the movement of Earth *i.e.* ether does not get dragged by the movement of Earth.

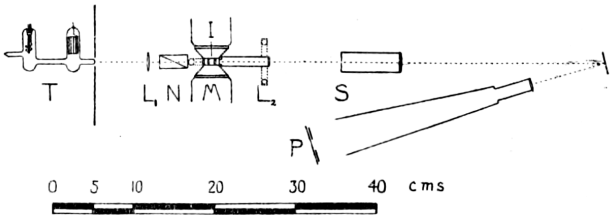

FIG. 91. *Watson's experiment to determine the influence of a transverse magnetic field on the speed of light in vacuum. He used a Neon tube discharge as a photon source, T, that he polarized using a Nicol prism, N. He then used a Fabry-Perot interferometer, I, inside a magnet, M, to create an interference pattern. He expected fringe broadening but measured none outside of uncertainties.*

Despite the ether being ruled out, experimentalists did not stop to look for a variation of the speed of light under a magnetic field as in the case of Watson's experiment figure 91, an experiment peculiarly close to a modern vacuum magnetic birefringence search but without clear theoretical foundations.

For these foundations to appear, new physics needed to be introduced first. The novelty came by way of Dirac, Euler, Heisenberg and Weisskopf who developed the quantum theory of vacuum at the beginning of the 20th century. In this theory a quantum of light can be absorbed in vacuum and transformed into a electron-positron pair in the presence of other electromagnetic fields. The phenomenon of absorption of light in a vacuum is incompatible with classical electrodynamics where fields can be superimposed without interacting. Scientists therefore introduced a non linear theory of electromagnetism in which the optical properties of a vacuum are function of the fields present, under this theory the speed of light is therefore function of the electromagnetic fields. The non linear properties of vacuum was confirmed by the emergence of the new theory of quantum electrodynamics (QED) the following years and experimentalists began to search for experimental signatures of variations of the speed of light.

One of the prediction of QED is that vacuum acts as a birefringent medium, a property that the BMV experiment tries to demonstrate. Since QED predictions seem to be always correct for other systems, we expect the same for vacuum. However, in a quantum vacuum everything exists in a virtual state, what is known as well as what is unknown. Experiments could add pages to this story that began centuries ago, an endeavour in which the BMV experiment is actively taking part.

J. Agil, J. Billette, J.-M. Lagarrigue, J. Béard, T. Moraine, R. Battesti and C. Rizzo

The effect of magnetic field on water - preliminary results and perspectives

In 2006, a Japanese group led by Sumio Ozeki at Shinshu University observed that a static magnetic field combined with a motion of water in the field gradient of a 6 T superconducting magnet would lead to a reduction of the contact angle (in other words a better wetting) between distilled water and a platinum substrate [Otsuka *et al.*, Phys. Chem. B Letter **110**, 1509 (2006)]. We have preformed several experiments to reproduce and confirm this phenomenon, with new results concerning the effect of the substrate choice, the field intensity, the water composition and the motion of water in the field profile. Preliminary results in figure 92 show the evolution of the contact angle as a function of time in the presence of an applied magnetic field of 8 T.

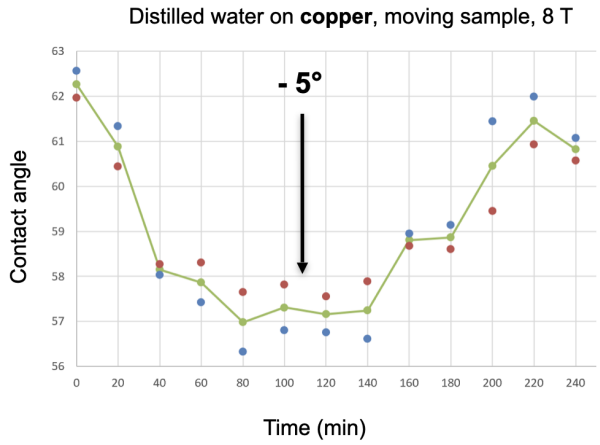

FIG. 92. *Contact angle between magnetized water and the copper substrate as a function of time. A magnetic field of 8 T is applied from 0 to 150 minutes. The evolution of the contact angle with time reveals a delay before reaching a stable value of the angle, both after switching on, and after switching off, the magnetic field. The green line/symbols is the average value of two measurements (blue and red symbols).*

The mechanisms responsible for this phenomenon are still unclear and require new experiments in high field to probe magnetic field effects on water properties.

To elucidate this issue we have investigated the effect of magnetic field on water, independently of any interaction with a substrate. A device was designed, where a water droplet is placed in a contactless diamagnetic levitation environment and excited by an acoustic wave. The vibration of the water droplet is accurately probed by a confocal sensor. The resonant frequencies and the time constant of the exponential decay of the free oscillation mode allows the determination of the surface tension and of the viscosity of the water.

An example of the oscillation of a diamagnetically levitated water droplet excited by an acoustic wave is shown in figure 93. Our preliminary results indicate a slight decrease of surface tension in magnetic field, accompanied by a large increase of viscosity, the main uncertainty being the estimation of the volume of the levitated droplet.

We have now started to investigate both the wetting on substrates and physical properties of water alone in high magnetic field. The experiments on wetting angle will be reproduced with more samplings for reproducibility testing. Different water solution with controlled ionic contents, magnetic and non magnetic, will also be used. As an alternative to investigating moving and non-moving water in the magnet, the effect of vibrations will also be tested. Oscillations of diamagnetically levitated droplets will be reproduced, taking into account the time effect, as a large time constant has been observed in wetting angle experiments. Also different ionic content (in that case only diamagnetic ions to maintain a stable levitation) could be tested.

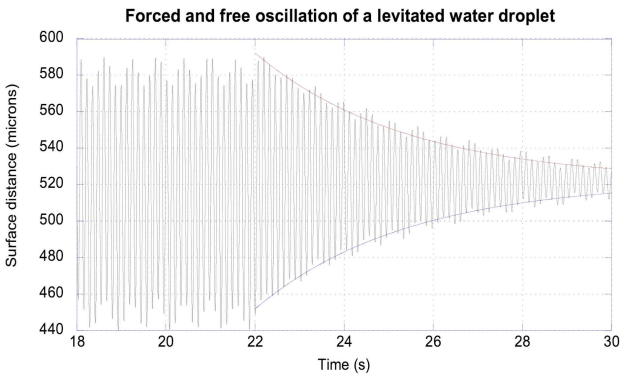

FIG. 93. *Preliminary results showing the resonance of a diamagnetically levitated water droplet excited by an acoustic wave. The resonant mode is $L = 2$. The first part of the trace (Time < 22 s) corresponds to a forced oscillation when excited with an acoustic wave. The second part (Time > 22 s), with a characteristic exponential decay, corresponds to the free decay of the resonance in the absence of acoustic excitation.*

Eric Beaugnon
Nicolas Glade (Recherche Translationnelle et Innovation en Médecine et Complexité (TIMC), CNRS-UGA-INP Grenoble), Noriyuki Hirota (NIMS, Tsukuba)

Normal field instability in undercooled Co-Cu melt

Immiscible Co-Cu equimolar alloys were solidified under high magnetic fields and high magnetic field gradients with a deep under-cooling, ranging from 191 to 280 K. Such a high under-cooling was obtained thanks to high purity components and boron oxide flux glass encapsulation of liquid metallic alloys. Prior to solidification, the liquid system consists of two immiscible liquid phases, a Co rich highly paramagnetic phase, and a Cu rich non magnetic phase. Due to high undercooling (actual solidification temperature below melting point), the solidification is very rapid and freezes the liquid distribution between the two phases.

In zero field (figure 94), the CoCu alloy exhibits a typical core/shell structure, where the Co rich phase is centered in the sample. The under-cooling was 280 K at that time. This structure is due to the coalescence of Co rich liquid phases during cooling at the time of liquid phases separation and to surface tension effects (Marangoni convection) in the radial thermal gradient during cooling.

The next samples in magnetic field are both influenced by the magnetic field value and the magnetic force value, related to half the square field gradient $B\,dB/dz$. In 1.02 T and 8.33 T^2/m, the microstructure still exhibits a 2 phases separation. In addition the cobalt rich phase is sedimented downward due to the vertical magnetic forces acting on the strongly under-cooled Co rich paramagnetic phase. The under-cooling was 191 K at that time. Increasing the magnetic field (4.152 T) and the magnetic force gradient (133.14 T^2/m) will give rise to a new microstructure. As seen on figure 94, the Co rich phase exhibits a normal field instability as it is known in ferro-fluids. Thanks to the high undercooling (219 K), the Co rich phase is very magnetic and self organizes as peaks and valleys as in ferro-fluids.

The inter peak spacing is given by,

$$\lambda_c = 2\pi \left(\frac{\sigma}{\rho g + M \frac{dB}{dz}} \right)^{\frac{1}{2}},$$

where σ is the interfacial energy, ρ is the specific mass, g is the acceleration due to gravity, M is the magnetization, and dB/dz is the field gradient.

The magnetic field gradient and force $M dB/dz$ play a major role in the surface instability as the peaks spacing depends on the local gravity, including both earth gravity and magnetic force. Without magnetic force, the interpeaks spacing could exceed the sample size so that no effect would be seen. Thanks to the strong magnetic force acting as an added gravity force, the peaks and valleys structure took place in the sample size.

For more details please see [Wei *et al.* Appl. Phys. Lett. **18**, 123 (2023)].

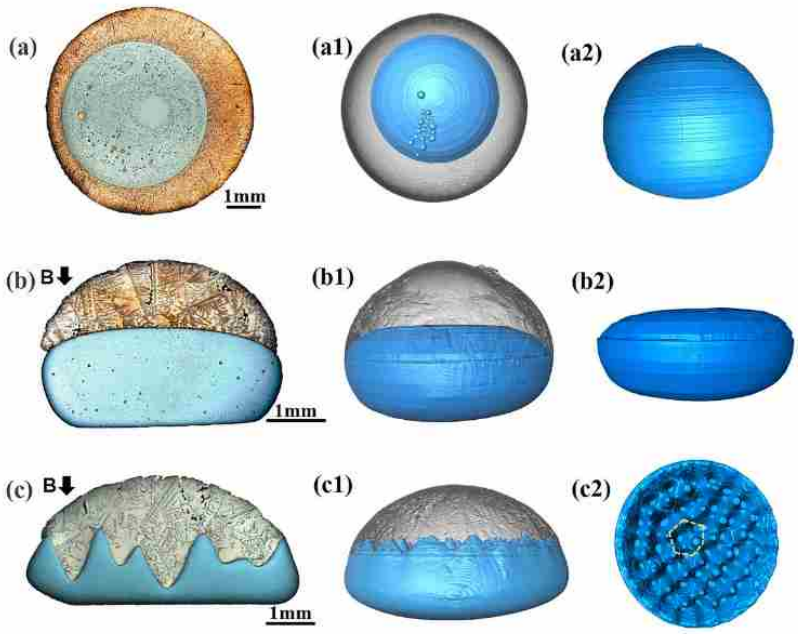

FIG. 94. *Microstructure of a CoCu immiscible alloy, undercooled and solidified in zero magnetic field (a, a1, a2), 1.02 T field (b, b1, b2) and 4.152 T field (c, c1, c2). a, b, c are seen from SEM vertical cuts along the field axis. a1, a2, b1, b2, c1, c2 are 3D CT referring to a,b and c samples. The Co rich phase is in blue.*

E. Beaugnon
C. Wei, J. Wang, Y. He, Y. Yan, J. Li (Northwestern Polytechnical University, Xi'an)

Alfven waves at low magnetic Reynold's number

We have investigated Alfven waves in a liquid metal. These waves combine transverse oscillations of the magnetic and velocity fields and propagate along the magnetic field lines. First predicted by Alfven in 1942, [Alfven, Nature, **150**, 405 (1942)], these waves were shortly after observed by Lundquist using a vessel filled with liquid sodium. More recently, experimental tests conducted at the Grenoble DC high field facility using a gallium alloy reported evidence of Alfven waves propagation [Alboussiere *et al.*, Phys. Fluids, **23**, 096601 (2011)].

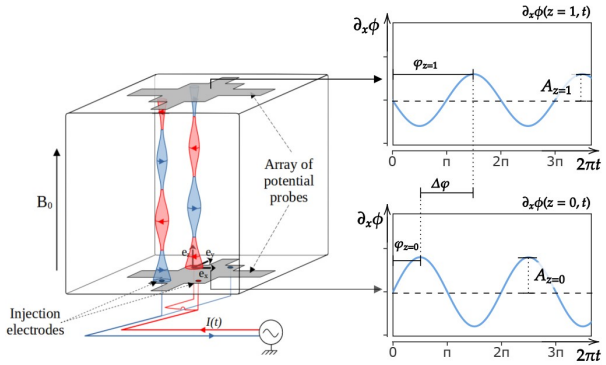

FIG. 95. *Illustration of two Alfven waves developing in the Flowcube device. The magnetic field B_o is vertical and injection current flow parallel to the bottom array of probes. The cube dimensions are* $150 \times 150 \times 100\,mm^3$.

At present, the dynamics of these waves and their role in energy transfers remain not fully understood. In astrophysics, these waves are suspected to be one of the main mechanisms for heating the solar corona to temperatures of several million Kelvin. However, they are very difficult to observe in this environment and even more difficult to study. We investigate these waves at a laboratory scale in a controlled environment that prevent any other parasitic waves from developing.

Figure 95 depicts two typical Alfven waves develop in the so called FLOWCUBE device subjected to a vertical, static and uniform magnetic field (up to 10 T in a 376 mm warm bore in this work). In this present illustration, waves are forced through an array of 2×2 injection electrodes, each being alternately connected to the output and then to the common.

Each electrode will inject a current which in return will induce a magnetic disturbance at the bottom plate. Due to the reflection of waves at horizontal plates, nodes and anti-nodes will appears, as illustrated in the same figure (for both velocity and magnetic field disturbances). Figure 96 gives the details of the organization of the potential probes located on the bottom plate.

Using the array of potential probes, and thanks to the noise reduction work operated this year, the potential gradient (in the x and y directions) at the bottom and top plates can be measured and recorded. From these potential gradients, the amplitudes and the phases of the Alfven waves can be determined. The last experimental campaign in May 2023 was successful in terms of signal to noise ratio thanks to the preliminary tests performed to optimize the sensitivity of the measurements. A detailed comparison has been conducted with a semi-analytical modeling.

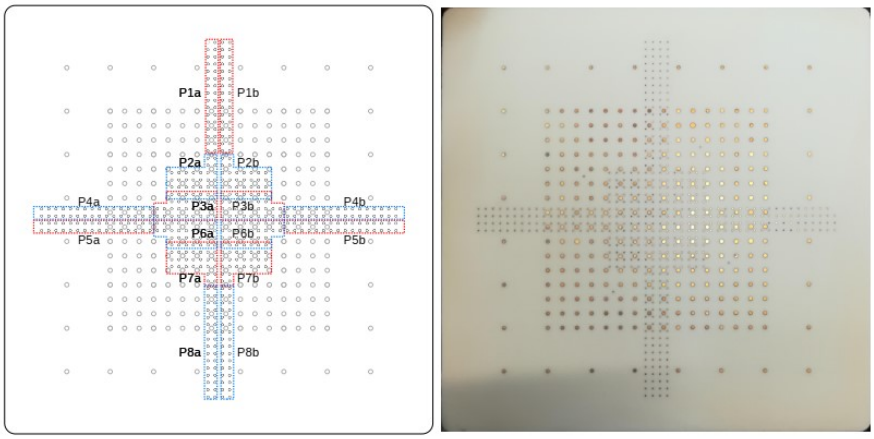

FIG. 96. *(Left panel): Diagram of the ceramic side of the bottom horizontal plate. The measurement areas that can be selected through the probe interfacing board are represented. (Right panel): Image of the ceramic side of the bottom horizontal plate.*

S. Lalloz, F. Debray, J. Spitznagel
L. Davoust (SIMAP, INPG, Grenoble), A. Potherat (Coventry University)

Instrumentation

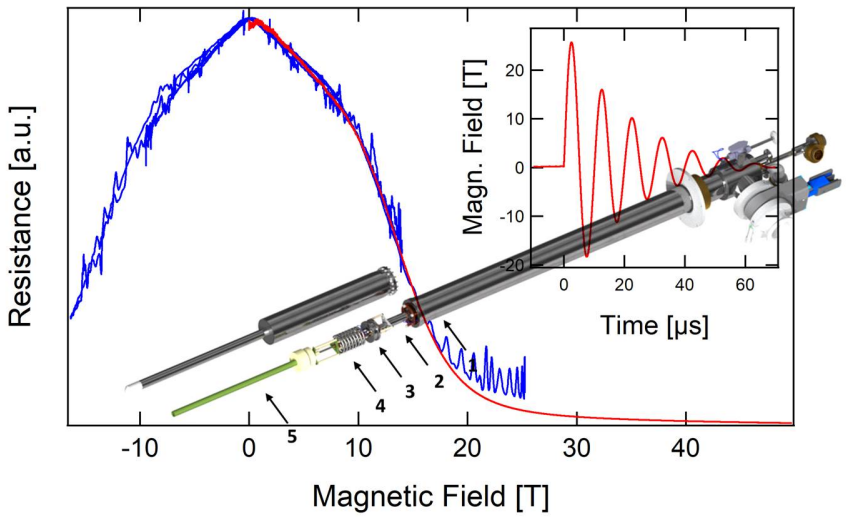

Cryogenic developments for the Megagauss generator

We report several improvements on the equipment of an additional measuring station. Located at the second termination of the generator current leads, the new experimental site is equipped with a frame supporting a cryostat.

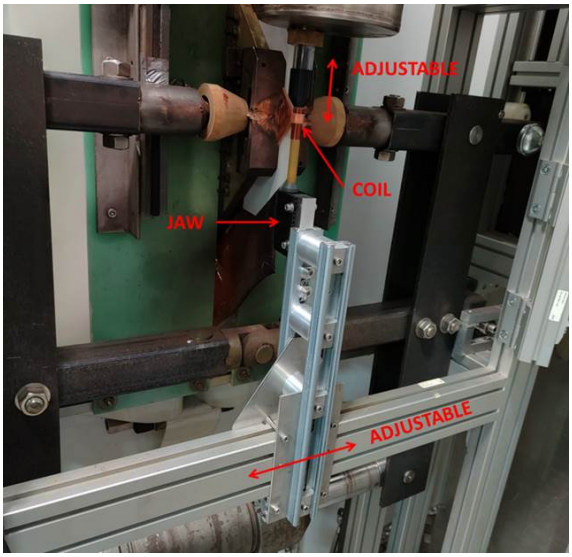

FIG. 97. *Cryostat mounted in the second cell of the Megagauss installation. The jaw gripping the fiberglass tube containing the tail is clearly seen.*

The overall rigidity of the chassis was improved by the addition of a beam allowing it to be firmly anchored to the walls of the room.

Centering the tail of the cryostat in the single-turn coil and maintaining it in position during the shot was accomplished with the help of a fiberglass tube placed in the coil, and into which the tail is inserted. The dimensions of the tube were chosen to minimize the clearance between the coil and the tail. The position of the assembly is then held rigidly thanks to a jaw, bolted to the frame and gripping the fiberglass tube (see figure 97).

The plastic-metallic extensions of the cryostat were lengthened by 40 mm which made it possible to move the tail connection part away from the coil. This was a weak point of the previous design because this part was having previously been damaged by successive shots.

The room was finally equipped with pumping lines and a gas handling panel (see figure 98) allowing the pumping on the helium bath, the gas recovery and the pumping on the cryostat insulation vacuum. The 60 m^3/h rotary-vane pump connected to the helium bath and the insulation vacuum pumping stations are placed outside the workstation for safety reasons, and also due to the impossibility of installing mains electricity inside.

FIG. 98. *The MegaGauss workstation arrangement showing the helium pumping and recovery system.*

M. Nardone, A. Zitouni, M. Barragan, L. Bendichou, N. Bruyant, O. Drachenko, O. Portugall, M. Massoudzadegan

A metallic-plastic ^{3}He-^{4}He dilution refrigerator for measurements in pulsed magnetic fields up to 60T

We report the design, and the initial phases of the assembly, of a dilution refrigerator devoted to magneto-transport measurements in pulsed magnetic fields up to 60 T.

The refrigerator will have a base temperature $\simeq 50$ mK, and is designed to suppress eddy current heating in the mixing chamber zone, with a sturdy and reliable construction for ease of use. The design integrates some of the technical solutions validated on a prototype commissioned in 2007.

A 3D overview of the system is shown in figure 99. A pumping line located above the still integrates, from top to bottom, an exchanger allowing precooling of the incoming 3He gas down to a temperature of 4.2K and a second exchanger, of the Joule-Thomson (JT) type, where the gas is cooled taking advantage of the enthalpy of the cold gas pumped into the still. This exchanger, replacing a classic 1K pot, allows avoiding the installation of a line and an additional pumping system, thus simplifying the construction and use of the apparatus. The gas is then JT expanded and enters the still, where it is further cooled. At the exit of the still a 2nd JT expansion allows almost total liquefaction. The gas undergoes a final cooling in a counter-current exchanger before entering the mixing chamber.

The mixing chamber is made of plastic and G10 fiberglass, while the metal parts are mainly made of stainless steel and the capillaries equipping the exchangers are made of CuNi. The choice of materials makes it possible to almost completely eliminate heating by eddy currents due to (i) the limited number of metallic parts, and (ii) due to the relatively low electrical conductivity of the metals used.

The parts located below the 4.2 K exchanger are included in a removable vacuum chamber equipped with an indium gasket flange.

A straight stainless steel tube connecting the upper end of the refrigerator to the bottom of the mixing camber allows the introduction of a fiberglass rod equipped with pairs of twisted wires for the magneto-transport experiments. Passing through all the exchangers, this tube ensures the perfect thermalization of the measuring wires, before they enter the mixing chamber. This flexible design allows the use of different rods, equipped with optical fibers or coaxial cables allowing us to perform a wide variety of measurements.

Unlike the previous prototype, the refrigerator will also be equipped with a heating system located inside the still. This heater will make it possible to control the temperature of the liquid and, consequently, the circulation rate of the gas which conditions the cooling power of such a refrigerator.

Construction of the refrigerator is underway, and functional tests are planned for the first quarter of 2024.

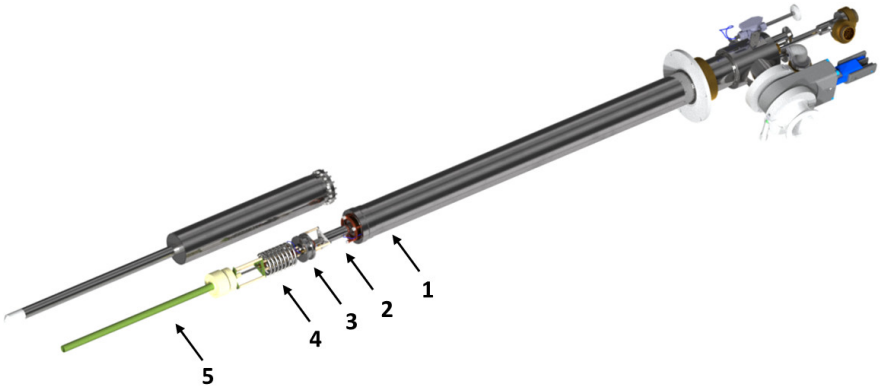

FIG. 99. *3D view of the ^{3}He-^{4}He dilution refrigerator for use in pulsed fields up to 60 T, showing (1) the 4.2K exchanger, (2) the JT exchanger, (3) the still, (4) the counterflow exchanger and (5) the mixing chamber.*

M. Nardone, A. Zitouni, M. Barragan, L. Bendichou, R. Martin

Megagauss developments and activities

TED measurements in MegaGauss fields: Transient electromagnetic disturbances (TED) are an inseparable part of MegaGauss (MG) fields, whose generation depends on the ability to handle high-voltage pulsed power on a very short timescale. Disturbances originating from switching processes reaching 100 kV with nanosecond rise times thus propagate by inductive and capacitive coupling as well as radiatively in MG-generators. An important preliminary step for implementing new measurement techniques is therefore to identify the precise source of TED, their propagation channels, as well as their point of entry into the measurement setup. TED are now for the first time investigated systematically in order to improve the protection of sensitive measurements. First results have revealed that different probes tend to exhibit similar TED structures thereby providing a possible handle for data corrections. The use of pick-up coils with opposite polarity has furthermore confirmed that some TED affect measurements via intentional or unintentional ground connections. Further investigations are in progress.

Electric transport measurements: Charge transport is a key characterization technique in condensed matter physics. Its implementation in MG fields is challenging, but the motivation to do so is high; the observation of quantum oscillations in optimally doped high-T_c superconductors or of new exotic states beyond the quantum limit in graphite are just 2 examples requiring transport measurements in the highest possible fields. In Toulouse, a transport setup making use of RF-techniques is being developed. Over the last couple of years, the project has given rise to a step-by-step improvement of the MG-generator's experimental environment and is now in a state of producing first proof-of-principle results under realistic conditions. As an example, figure 100 shows the magneto-resistance of InAs obtained in a non-destructive oscillating field produced with the MG generator. Under these conditions the measurement setup has to cope with the same TED, short duration and a somewhat reduced but still significant eddy-current heating. The principal advantage of the non-destructive operation mode is the possibility to repeat experiments rapidly for testing purposes.

Miniaturized magnetization probes: New miniaturized magnetization probes have been developed that are compatible with a bath-type cryostat introduced in 2022. With the new probes the temperature limit for magnetization measurements is reduced to typically 2.5 K which can be reliably produced with the new cryostat.

SF_6 recycling circuit: Spark-gaps operated with mixtures containing the greenhouse gas SF_6 are without alternative when it comes to the switching of high-voltage pulsed-power installations such as the MG-generator. As each discharge decomposes part of the SF_6, thereby changing its isolation properties and giving rise to chemically aggressive reaction products, the gas is normally renewed after each shot. In order to reduce the environmental impact associated with this practice and to avoid problems with an ever-tightening legislation, a recycling circuit has been developed. While in its present form the system permits the purification and repeated use of the same gas, it is planned to extend its functionalities so as to permit a quantitative analysis and correction of the gas mixture.

French-Japanese MG collaboration: To motivate a wider use of MG-fields, facilities involved in this area need to address three key issues; the overall improvement of measurement conditions, in particular as far as TED are concerned; the development of new measurement techniques such as electric transport; and the production of exemplary scientific results with high visibility. To cope with the significant scale of these tasks, MG-groups in Toulouse and Kashiwa (ISSP, University of Tokyo) have started to intensify and formalize their long-standing collaboration.

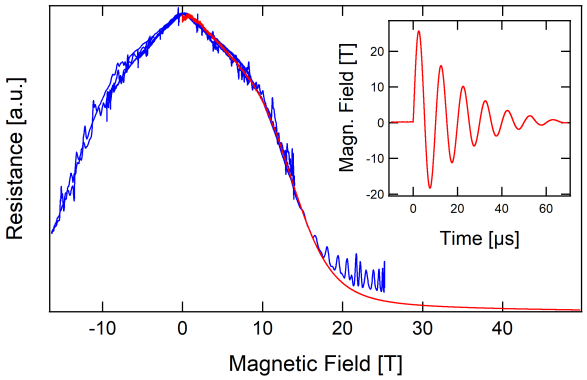

FIG. 100. *Proof-of-principle low-field measurement of the magneto-resistance of InAs with the MegaGauss (MG) generator (blue) as compared to a recording obtained with conventional pulsed magnetic fields (red). The MG trace sweeps back and forth several times in accordance with the oscillating field shown in the inset. It exhibits more noise but coincides clearly with the reference measurement. Subsequent recordings at full field have revealed comparable data, albeit with some deviation attributed to eddy-current heating. To avoid the latter, steps are currently taken to reduce the sample size further.*

O. Portugall, O. Drachenko, S. Badoux, M. Barragan, N. Bruyant, M. Massoudzadegan, M. Nardone, C. Proust, D. Vignolles, A. Zitouni
B. Reulet (University of Sherbrooke), Y. Skourski (HLD Dresden), Y. Matsuda, A. Miyata (ISSP, University of Tokyo)

Magnet Development

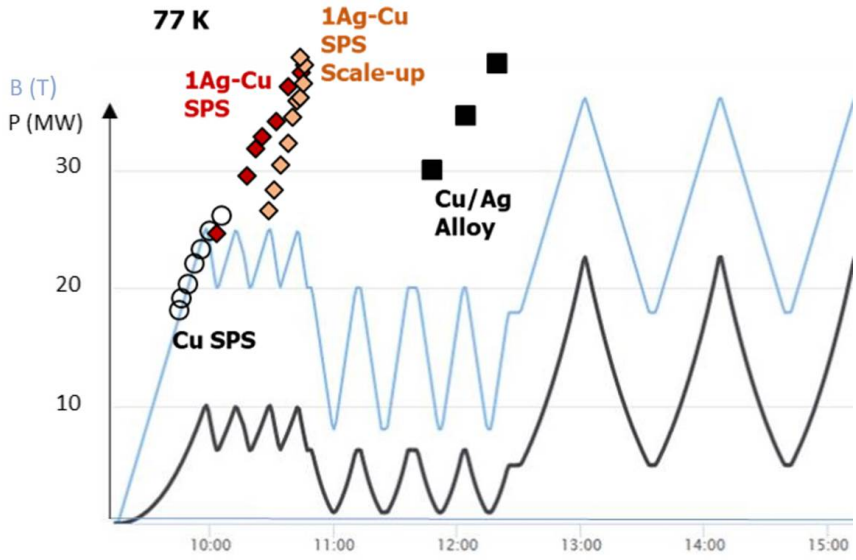

The UpAlim project at the DC high magnetic field installation

The main objective of this project is to put into operation a new 60 MVA 225 kV/15 kV transformer. This will happen, after the final acceptance is made in 2024, transferring the ownership to CNRS. The transformer will be used to power the high field DC resistive magnets in Grenoble.

FIG. 101. *28th of September 2023; arrival of the new 60 MVA 225 kV/15 kV from SIEMENS-Italy through the Frejus Tunnel.*

The first goal of this direct connection to the high voltage grid (which was provided by RTE) of the new 60 MVA transformer is to be able to power the high field magnets up to 30 MW instead of 24 MW which is the actual limit since 25 years. In 2023, decisive milestones were reached in the Upalim project. Namely, (i) delivery of the 60 MVA transformer on site (figure 101), (ii) integration in the new building (figure 102) and (iii) qualification tests of the 18 MW + 12 MW magnet configuration that will be used during the final test (figure 103).

To prepare the 30 MW operations with the new transformer we have performed tests of a large bitter coil modified to accept a maximum power of 18 MW. Figure 103 shows the chronogram of one of the tests performed after the setting of new parameters on our AC/DC convertor. A maximal power of 16.04 MW was successfully injected into the magnet which corresponds to a high voltage power of 17.85 MW. Actual limitation of the old 15 KV lines prevents us from testing at higher power.

FIG. 102. *Installation of the new transformer in its building after assembly of the two side heat exchangers. On the right, one distinguishes the departure of the 15 KV orange lines connected on the other side to the HTA Cells located in the LNCMI building.*

Since all the electrical power is converted into heat, we have to ensure that 30 MW of cooling capacities would be available from the river. We therefore tested the hydraulics, which usually operate up to 1400 m^3/h with a single pump, to prepare the upgrade to 1800 m^3/h with two pumps.

The final test at 18 MW and then at 30 MW will be made when the new transformer will be made available during 2024.

FIG. 103. *Qualification test for 30 MW operation. Chronogram of the 25th of October 2023. Blue: Magnetic Field, Purple: Power on the bitter coils, Green: total Power. The high field magnets are made of two submagnets powered and cooled independently (only the low pressure cooling side is in common). Powering a 30 MW magnet will consist of powering one submagnet at 18 MW and the other one at 12 MW.*

R. Barbier, F. Debray, C. Grandclément, R. Jaymond, K. Paillot, B. Vincent, C. Warth

Upgrade of resistive Bitter magnets for 18 MW

A power upgrade from 24 to 30 MW is ongoing at the Grenoble facility. Starting from 2024, a maximum of 18 MW DC Power (12.5 MW today) will be available for the external Bitter coils. The 18 MW installation will deliver a nominal current $I_o = 33$ kA. Around ten years ago, similar large diameter Bitter coils were designed at the Dutch high magnetic field facility (HFML-Nijmegen). In the framework of the European project ISABEL, we carry out a design study to investigate the possibilities that both Bitter coil sets will be suitable for the available extra power. We recall that a Bitter magnet is built by stacking of copper alloys disks.

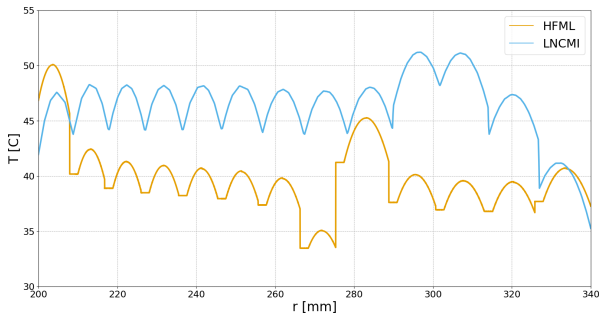

FIG. 104. *New inner Bitter coil temperature distribution (Axi model) for $I = 31$ kA at $z = 0$. Comparison between HMFL tool based on analytical 1D model and in-house numerical Axi model.*

The actual Bitter magnets are designed for a power of 12.5 MW. To account for the power upgrade to 18 MW while keeping the available Bitter disks at our disposal, we simply increase the size of the central section of the innermost Bitter. This allows to obtain a new stacking scheme. This minimizes the impact on the assembly process, and the commissioning of the magnets, since these operations are complex and time-consuming. Dimensions of the new inner Bitter stacks are given in table III. With this design, the Bitter magnets are expected to provide 12.06 T for a maximum power of 18 MW (10.25 T with 12.5 MW in the actual design).

r_1 [mm]	r_2 [mm]	L [mm]	n
199	341	41.39	6
		522.6	158
		41.39	6

TABLE III. *18 MW inner Bitter. The Bitter is divided into 3 sections. The angular shift between 2 Bitter disks is constant.*

To confirm these estimates, tools from HFML were used as well as a new 2D axisymetrical numerical model for Bitter magnet simulations developed in-house (figure 104 and figure 105). This model relies on *Feel++*, the FEM library used for poly-helices insert.

An inner Bitter has been assembled following this design and tested up to 20.6 kA to keep the electric power below 12.5 MW. Comparisons between measured data and estimates by our 2D Axisymetric model are displayed in figure 106. The computed magnetic field factor is 3.75 G/A. The measured one is 3.77 G/A. Subsequently we ran the new Bitter magnet at 31 kA which corresponds to 16 MW, 11.7 T which is 5% less than the computed value for the power and 2.5% less for the magnetic field.

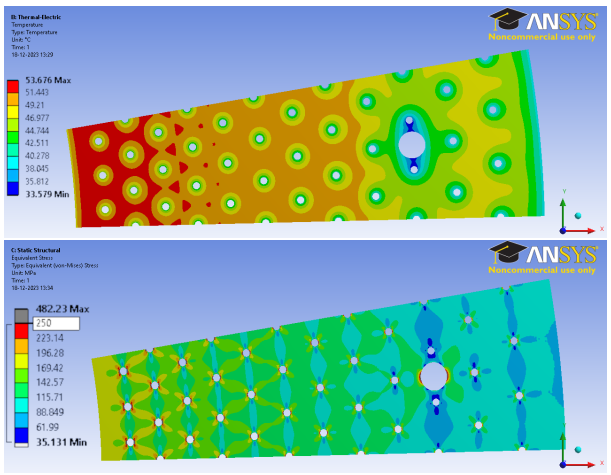

FIG. 105. *New inner Bitter (HMFL model) (top) temperature distribution in the mid-plane for $I = 31$ kA. The maximum temperature is about 53°C; (bottom) von-Mises distribution in the mid-plane. The maximum von-Mises stress in the new configuration is about 250 MPa compared to 225 MPa in the previous design.*

Finally, we explore more advanced designs with the HMFL optimization tools. Preliminary studies show that we can slightly increase the magnetic field to 12.25 T for 18 MW with a complex stacking (with 7 sections instead of 3 and with a non-constant angular shift between the disks).

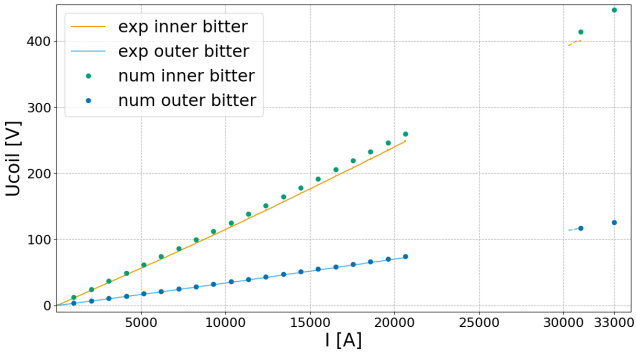

FIG. 106. *Comparisons of measured (plain lines) and computed voltage drop (dots) for the inner and outer Bitter.*

F. Debray, J. Muzet, C. Trophime
F. Wijnen (HMFL, Nijmegen)

DC high magnetic field facilities - from intermittency to flexibility

From an energy point of view, the use of DC high field magnets is characterized by a large intermittency linked to the fact that users work "one user at a time" so there is no averaging of the power consumption. Representative power and magnetic field versus time traces are shown in figure 107. The energy trace of the facility is directly linked to the strategy of a given researcher for his/her experiments. This is in contrast to what is observed in a Synchrotron, with dozens of beam lines operating in parallel.

In 2023, the DC high magnetic field facility has consumed 11 GWh of electricity for 2000 hours of magnetic field operation which leads to an average power of 5.5 MW for a maximum magnet power available of 24 MW. This intermittency can be described mathematically using traditional statistical tools, mean values, standard deviation, *etc.*

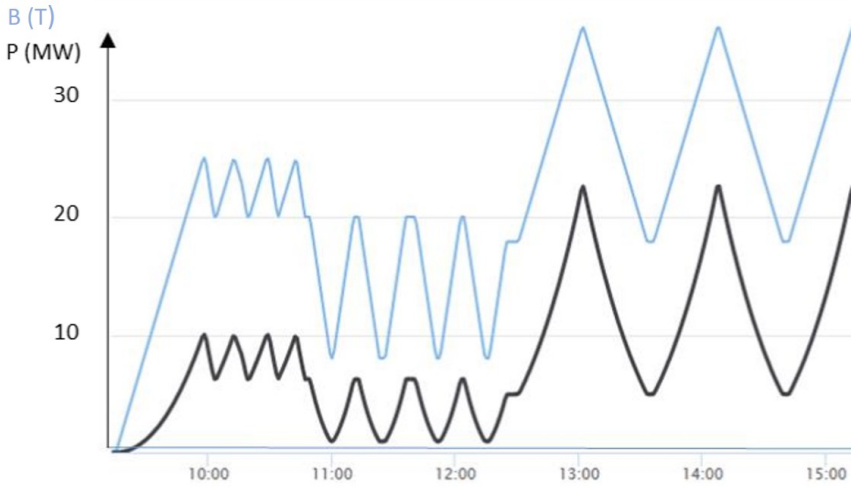

FIG. 107. *Representative power used (black curve) and magnetic field generated (blue curve) versus time traces at the DC high magnetic field facility displaying the large variability of power consumption.*

On the other hand, the notion of flexibility cannot be understood from a purely mathematical approach, as it incorporates the underlying notion of reaction to social and technical demands. These demands are numerous and vary from one year to the next:

- The smooth running of the scientific experiments
- The optimisation of the purchase of electricity
- Projects to recover waste heat
- Participation in network balancing mechanisms

The variability of external constraints means that a purely statistical analysis of the laboratory's operation is no longer sufficient to optimize its energy use. Between 2018 and 2022, we were seeking to quantify these constraints either through experimentation (load shedding operations involving the researchers) or through reorganization of the planning for waste heat recovery optimization (figure 108).

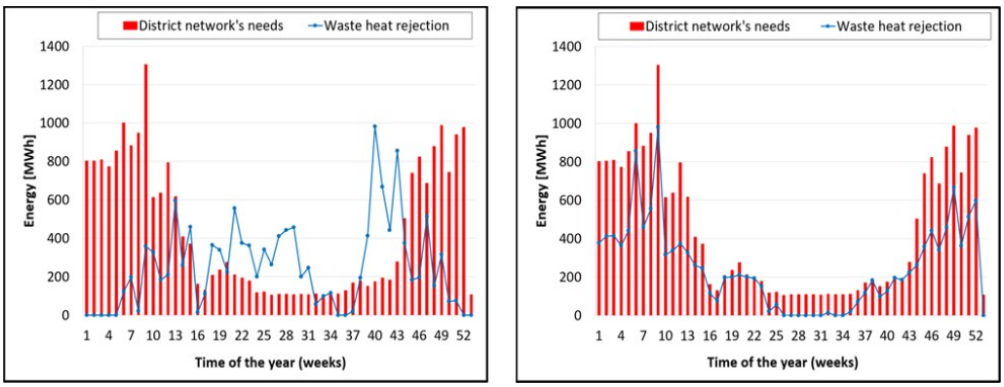

FIG. 108. *(Left) Waste heat of the DC magnetic field facility (blue line) and energy demand by the Grenoble heating network (red bars) . (Right) The graph corresponds to a reorganisation of the DC magnetic field facilities weekly consumption blocks to maximise the recovery of calories from the heating network [Hodencq 2021]*

In order to take advantage of the social science perspective on energy issues, the DC high magnetic field facility has proposed itself as a field of study for inter-

disciplinary projects at the UGA concerning "energy in neighbourhoods". The interest of integrating the social sciences into the question of energy optimization was raised by us during discussions at the conference on "Sustainable energy for research infrastructures" held at the Grenoble Synchrotron in September 2022.

To develop this approach over a wider scale we have written a project about Flexibility in Research Infrastructures for global CArbon Neutrality (FlexRICAN) which has been funded for 2024-2026 (figure 109). It brings together three large scale infrastructures that currently have, or are envisioned to have when their operation commences, different energy usage profiles, namely:

- The European Spallation Source, Sweden.
- The Extreme Light Infrastructure, with two facilities in Czech Republic and Hungary.
- The European Magnetic Field Laboratory, Grenoble and Nijmegen for DC fields and Dresden and Toulouse for pulsed fields.

Through the development of a multi-energy approach integrating academic knowledge in social sciences, open access tools for multi-energy modeling and two actors of the energy sector (Alfa Laval and Energy Pool), the project will propose new solutions to reduce the environmental impacts of research infrastructures for contributing to their the long-term sustainability and to the European energy system resilience.

This project will benefit from ongoing works to assess the carbon footprint of the DC high magnetic field facility following the Labo1.5 standards recommended by CNRS. For the Grenoble site, it shows that the 11 GWH of annual electricity for the DC magnetic field facility accounts for about a third of the laboratory's carbon footprint. The dominant item is actually purchasing.

This shows how important it is for future investments to calculate the life cycle assessment (LCA) of future magnets or instrumentation apparatus to be brought into operation (*e.g.* the use of helium versus electricity). Finally we are participating in the priority research program of the French Government which seeks to develop a socio-technical approach to address the question of flexibility in advanced energetic systems.

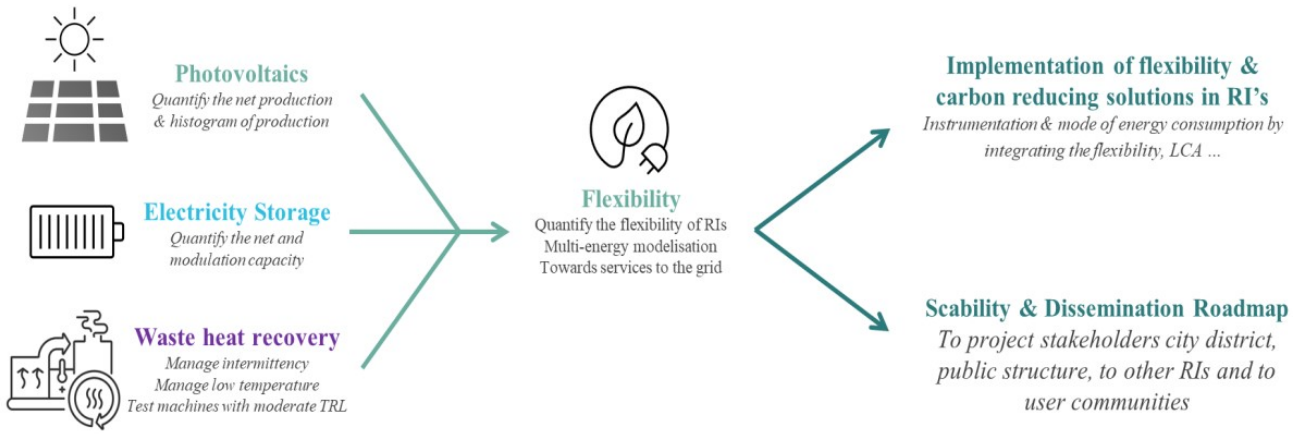

FIG. 109. *FlexRICAN Project concept from intermittency to flexibility and services to networks.*

F. Debray, R. Raison, K. Paillot, B. Vincent
S.Hodencq, F. Wurtz, N.K. Twum-Duah, B. Delinchant (G2Elab, INPG-UGA-CNRS, Grenoble)

Commissioning status of the 43+T hybrid magnet

The hybrid magnet is a modular user platform based on resistive and superconducting technologies. It will produce various high DC magnetic field and flux configurations ranging from 43 T in 34 mm diameter bore with 24 MW of electrical power to 9 T in 810 mm diameter bore, when the superconducting coil is used alone. Thanks to the ongoing upgrade of the electrical power installation from 24 MW to 30 MW, the opportunity to increase the total field significantly above 45 T was anticipated for the superconducting part as well as for the mechanical structure and will require an optimization of the resistive inserts. The large-bore "outsert" coil of the hybrid magnet is based on a specifically developed Nb-Ti/Cu superconducting conductor.

FIG. 110. *View of the hybrid magnet from the ground floor. The total height is about 5.4 m for a total weight of about 52 tons. Water cooling system for the 24 MW resistive inserts can also be seen.*

The magnet cryostat with its support structure includes an eddy-current shield and is connected via a cryogenic line to a cryogenic satellite, fed by a fully dedicated 150 l/h He liquefaction plant. All parts have been built, tested and delivered to LNCMI-Grenoble, where integration and final assembly were successfully completed in 2022 (figure 110). The commissioning tests of the overall system started thereafter and was pursued in 2023.

Several project milestones have been achieved in 2023 such as: (i) Mounting of the polyhelix magnets and improving the centering of the resistive and the superconducting coils (figure 111), (ii) Successful thermal cycle of the superconducting coil with warm-up from 1.85 K to 252 K for the 2022-2023 winter break followed by a cool down to 1.85 K for the phase-2 of the commissioning, (iii) Powering cycles of the superconducting coil up to the nominal current of 7150 A, corresponding to a central field of 8.5 T, (iv) Tests of the magnet safety system and energy extraction ones with fast and slow energy dump, progressively by steps of 25%, up to the nominal stored energy of 77 MJ, (v) First tests of electromagnetic coupling between resistive and superconducting magnets, and (vi) Measurements of the field map in the axial direction.

The superconducting magnet is now slowly warmed up by stopping LHe transfer and maintaining the LN_2 flow for the winter break. This step is also part of the commissioning program and required dedicate tuning of the cryogenics to limit the maximum temperature of the superconducting coil, hopefully to about 110 K, prior to restart the cooling down in March 2024. The commissioning tests of the hybrid magnet, *i.e.* with superconducting, Bitter and polyhelix coils, will be pursued in 2024 up to 41 T and then 43 T as first steps. Discussions are ongoing to profit from these powering cycles to perform in parallel scientific experiments. At present a total of five scientific proposals have been selected to be performed, starting in 2024.

FIG. 111. *Installation of the external Bitter coil inside the warm bore of 814 mm diameter, seen from the mezzanine covering the upper part of the hybrid magnet cryostat.*

More information can be found in [Pugnat et al., IEEE Trans. on Appl. Supercond. **32**, 1-7 (2022)].

R. Barbier, F. Debray, C. Grandclément, M. Kamke, S. Krämer, Y. Krupko, K. Paillot, R. Pfister, P. Pugnat, L. Ronayette, E. Verney
C. Berriaud, B. Hervieu, F. Molinié (CEA-Saclay, Gif-sur-Yvette)

Toward normal operation of the cryogenics for the hybrid magnet

The technology choices for the superconducting "outsert" coil (SC) of 1100 mm inner diameter of the hybrid magnet is based on the low temperature superconductor Nb-Ti/Cu cooled down by about 1500 litres of pressurized superfluid He. The production of the superfluid He requires a dedicated cryogenic satellite designed by CEA-Saclay and built by Air Liquid. This cryogenic satellite is fed with LHe at 4.5 K and 1.3 bar coming from a 4500 litre dewar connected to a fully dedicated cryoplant, including a He liquefier of 150 l/h production rate designed and manufactured by Air Liquide (figure 112).

FIG. 112. *Overview of the core part of the cryogenic utilities with on left side the He liquefier cold box connected to the intermediate dewar of 4500 l providing LHe to the cryogenic satellite producing the pressurized superfluid He to cool down the superconducting magnet.*

During the phase-1 of the commissioning in 2022, an unexpected stop of the cooling water distribution provoked the automatic switch-off of the pumping group with as ultimate consequence the growth in the 4 K - 1.8 K heat exchanger of a solid air plug preventing the production of superfluid He. The decision was made at that time to stop the 1.8 K pumping unit and let the magnet to warm up to 4.4 K and stabilize it at that temperature for first powering tests with a limitation of the magnet current to 2 kA. As expected, the partial warmup of the cryogenic system during the 2022/2023 winter break allowed the unblocking of the 1.8 K pumping line. Prior to launch the second cool down, several improvements were made to the cryogenic system including: (i) Repair of the leak causing the solid air plug inside the 1.8 K pumping line and the water pipes of the rough pumps; (ii) Implementation to the cryogenic control system of some automated processes; (iii) Reconditioning of all cryogenic circuits because of a fault operation sequence polluting the system; (iv) Implementation of a glass box ventilated with N_2 gas around the top of the current leads to reduce ice formation on the upper part of the cryogenic satellite; (v) Maintenance of the 125 m^3/h recovery compressor for storage of gaseous He up to 200 bars. The time evolution of the average magnet temperature during the second cool down starting at 252 K down to 1.85 K shown in figure 113. Experience gained during phase-1 allowed a significant reduction of the cooling time from 10 K to 1.85 K of about 5 days. At present, the total cool down duration is fully limited by manpower resources.

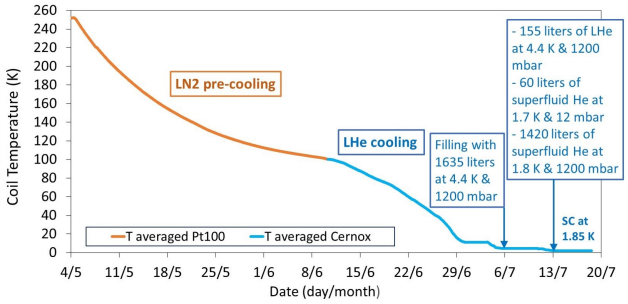

FIG. 113. *Average temperature of the superconducting "outsert" coil during the second cooldown with the LHe inventory. The time spent to cool down the SC from room temperature to 252 K during the first cooldown was about 3.5 days.*

During energy discharge test of the superconducting coil within the dump resistors, severe disturbance of the cryogenic system was observed due to large AC losses in the SC. The superfluid He level in the pumped bath showed strong oscillations without attenuation requiring delicate manual tuning of the PID (proportional-integral-derivative) parameters. Since an optimized PID-setting has not yet been found, the discharge test at 8.5 T was postponed to the phase-3 of the commissioning. Thunderstorms on July 24th provoked a general power outage and the cryogenics were manually put into the fallback state with second warmup launched, ending the phase-2 of the commissioning for the summer break. No damage was noted and the commissioning was restarted in September, starting with a cool down from 91 K. The overall test program of the superconducting coil alone was prematurely stopped on 6th of October because of a problem occurring on the recovery compressor, that was later one solved. The cryogenic system was then put in standby mode with LN_2 cooling to limit the magnet warm-up to about 90 K during the winter break. The commissioning of the overall hybrid magnet up to the nominal field of 43 T, *i.e.* with resistive inserts, is expected to be completed in 2024.

R. Barbier, C. Grandclément, Y. Krupko, R. Pfister, P. Pugnat, L. Ronayette C. Berriaud, B. Hervieu, F. Molinié (CEA-Saclay, Gif-sur-Yvette)

Powering-up tests of the hybrid magnet outsert

Prior to powering cycling, the electrical measurements from the commissioning phase-1 were repeated to check that no damage had occurred during the thermal cycle. Identical results have been obtained for the resistance, the residual resistance ratio (RRR), the electrical capacitance of the SC coil with respect to ground, and its inductance. The insulation with respect to ground measured at 500 V during 2 minutes was found to be much higher, with leakage current of 1.1 μA corresponding to an insulation resistance better than 470 MΩ , mostly due to the ventilated box with N_2 gas around the top of the current leads, which significantly reduced the humidity coming from ice formation and melting.

The second commissioning phase was devoted to the powering of the superconducting coil by steps of 25% of stored energy up to the nominal field of 8.5 T followed by discharge tests in dump resistors (figures 114 & 115). Numerous spikes were observed on the differential voltages used for the magnet protection with amplitudes exceeding the 100 mV quench detection threshold. Their duration of a few ms never reached the magnet safety system (MSS) validation time of 100 ms, and no false quench detections were triggered.

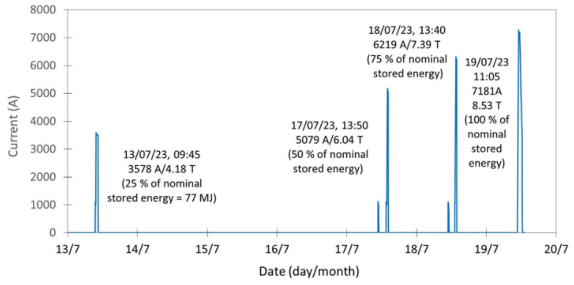

FIG. 114. *Powering cycles of the SC outsert magnet corresponding to the increase of magnetic stored energy by steps of 25% up to the nominal field. Except for the last one, the flat top was ended by a FD tests within 70 mΩ dump resistors. The FD test was performed at nominal current during the phase-3 of the commissioning.*

The occurrence of spikes in a superconducting magnet, due to the mechanical activity of the winding, is analogous to the earth's crust seismicity with earthquakes. This is the Kaiser effect, which originates fracture precursors of some materials submitted to successive mechanical loadings. In figures 115 at low current, no spikes or seismic events are observed until the previous mechanical loading is exceeded. At higher current values, an overlap is observed, but with a significant attenuation of the spike amplitudes during the second loading. The spike location, obtained from the position of the voltage taps, suggests that most spikes develop at the interface between the first/last double pancakes and the upper/lower flanges respectively. They probably originate from sliding frictions at these locations, but without sufficient energy deposition to trigger training quenches, as expected.
The current ramping of the SC to reach the nominal field of 8.5 T/7155 A was performed at 4.62 A/s. Because of AC losses, the SC temperature was increased in average by 80 mK with a minimum margin on the flat top of 180 mK between the hottest double pancake, which is the upper one, and the lambda point of the superfluid He. For this current ramp-rate value, one can guess that the critical heat flux of the superfluid He in the conductor channel was exceeded. However, for a ramp-rate of 1.45 A/s, no temperature increase of the SC was observed, suggesting that the heat deposition in the superfluid He bath originating from AC losses is extracted without affecting the enthalpy margin of the superconducting conductor. This needs to be more deeply investigated to define the proper magnet energization rate.

For the phase-2 of the commissioning, only the Bitter coils were mounted inside the hybrid magnet, the poly-helix ones being in run-in test on another site of the laboratory. The Bitter coils were first powered up to 9 T/30532 A with a ramp-rate of about 22.2 mT/s. A controlled fast de-ramp of the Bitter at 88.3 mT/s was then performed and no quench detection from the MSS was triggered. Among other tests performed, a trip of the power converter of the Bitter coils was triggered at 5 T/16962 A provoking a quench detection by the MSS and a fast current discharge in dump resistors. All these coupling between resistive and superconducting coils will be deeply studied in 2024 together with high magnetic field plateaus up to 43 T. For more details please see [Pugnat *et al.*, IEEE Trans. on Appl. Supercond. **34**, 1 (2023)].

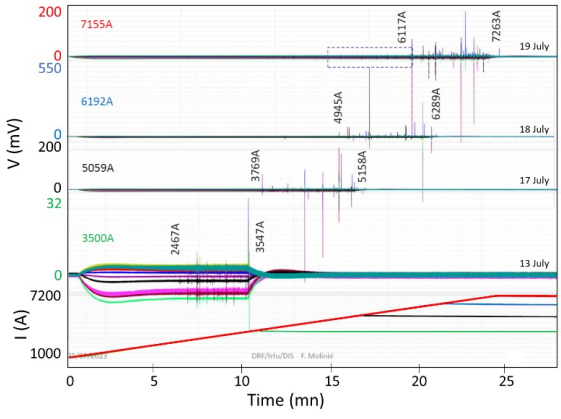

FIG. 115. *Superconducting magnet seismicity during its successive powering up to the nominal field/current of 8.5 T/7155 A. The Kaiser effect is observed in spike occurrence recorded from differential voltage measurements used as inputs of the MSS.*

R. Barbier, C. Grandclément, R. Pfister, P. Pugnat, L. Ronayette
C. Berriaud, F. Molinié (CEA Saclay, Gif-sur-Yvette)

Alternating field – a new opportunity in high field resistive magnets

We have developed a method to generate alternating magnetic field with a high sweep rate and large amplitude using resistive magnets and the 24 MW DC power supplies. This was motivated by the need to extend the AC magnetic field range of the magnetochiral dichroism (MChD) setup, as well as the need to broaden the experimental possibilities for future users. Previously, to reverse the polarity using single-quadrant power supplies we had to:

- Set the field to 0 T and switch off the power supplies,
- Physically change the polarity of the magnet connections,
- Restart the power supplies.

This procedure takes $\simeq$ 1 minute preventing the polarity from changing continuously.

The high field resistive magnets are made of two concentric sub-magnets powered by independent current sources. Recently, we developed the possibility to control each sub-magnet independently in order to use EcoNRJ mode, which saves 13% energy at constant usage [Paillot *et al.* IEEE, **32**, 6, (2020)]. We have extended this concept to develop an unconventional control mode where the two sub-magnets have opposite polarity. In this configuration, no physical change in magnet connections are required, and the field polarity can be reversed simply by adjusting the current in each sub-magnet as illustrated schematically in figure 116

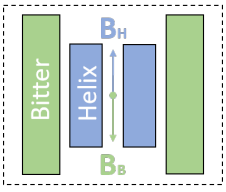

FIG. 116. *AC magnetic fields can be generated using sub-magnets with opposite polarities.*

Figure 117 shows the experimental traces of tests performed in March 2023 which illustrate the working principle. B is the sum of the magnetic field created by the Helix and Bitter magnets which are connected to have opposite polarity. Independently controlling the current to each sub-magnet we can generate a total field of either polarity.

We have added functions to the GPIB interface to remotely control the current for each magnet. A LabVIEW software has also been created to allow the user to control the amplitude and sweep rate of the alternating field. The MChD setup was installed for preliminary measurements. Finally we used the high resolution surveillance system of the power supplies and magnet to record technical data.

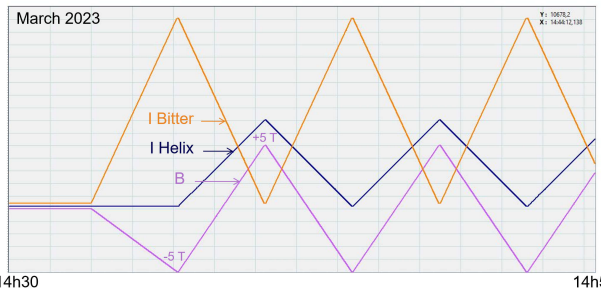

FIG. 117. *Generating AC magnetic field using a 24 MW resistive magnet. The currents of Helix and Bitter coils with opposite polarity independently ramp up and down to produce AC magnetic field.*

In this mode, maximum field amplitude is limited by the Bitter magnet to ±10 T and the maximum sweep rate is twice the maximum field rate allowed by the Bitter magnet. This has been tested for a magnetic field amplitude of ±5 T at a sweep rate of up to 1600 G/s. However, the magnet and power supply specifications should allow at least 2000 G/s with an amplitude up to ±10 T. This could be verified in the near future if required by users.

Figure 118 shows an interesting working point at "zero field" where the magnetic field of each sub-magnet exactly cancel at the field center.

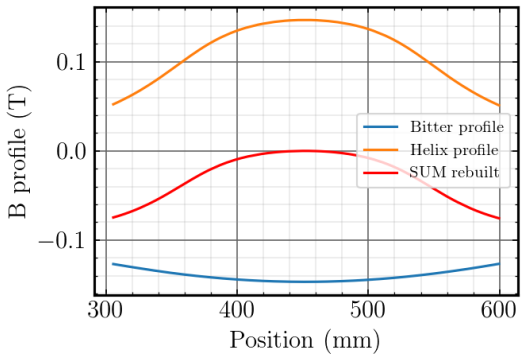

FIG. 118. *Magnetic field main axis-profile using this mode at "zero field". The field cancels out only at the center since both sub-magnets have a different geometry.*

Preliminary MChD measurements have been performed and validated by comparing the results with those obtained on the ±2 T superconducting magnet. A proposal has already been accepted for a future experiment using AC field generated by a 24 MW resistive magnet.

K. Paillot, C. Grandclément, M. Atzori, M.S. Raju, B. Tomba, F. Debray, C. Train

Self-consistent model for estimating the critical current of the Nougat HTS insert

To accompany the in-house development of high temperature superconductor (HTS) magnets we have initiated an activity on implementing numerical models to simulate HTS using some specific tools of the multiphysics toolbox *CFPDES* of the *Feel++* Open-Source library we have developed in collaboration with IRMA-University of Strasbourg.

Validations of the models have been performed on examples from the HTS modeling platform. A GitHub repository named feelpp-hts containing modeling files reproducing simple cases with *Feel++* is available, as well as the documentation.

We applied them to the Nougat insert, an HTS solenoidal coil composed of 9 stacked double pancakes. We present some simulations run in parallel that we carried out for the estimation of the critical current I_c as a function of the external applied magnetic field using an iterative algorithm based on the magnetic vector potential A,

$$\nabla \times \left(\frac{1}{\mu} \nabla \times A \right) = J,$$

so that $B = \nabla \times A$ where B is the magnetic flux density (T) and J is the current density (A/m^2).

The electrical resistivity of the HTS material is defined by the so-called $E - J$ power law,

$$E = \rho_{\mathrm{HTS}} J = \frac{E_c}{J_c(B,\theta)} \left| \frac{J}{J_c(B,\theta)} \right|^{n-1} J,$$

with E, E_c, $J_c(B,\theta)$ and n respectively the electrical field (V/m), the critical electrical field (V/m), the critical current density (A/m^2) and a material dependent index. $J_c(B,\theta)$ describes an anisotropic dependence of J_c on the magnitude and orientation of B for the considered HTS material. It depends on the tape design and is defined by a fit function obtained from measurements.

For our model to estimate the critical current, the power law can be inverted to find the current I_i within each tape Ω_i,

$$J_i = J_c(B,\theta) P_i,$$
$$I_i = P_i \int_{\Omega_i} J_c(B,\theta) d\Omega_i,$$

with $P_i = E_i/E_c \times |E_i/E_c|^{1/n-1}$ and E_i is the electric field, uniform across the cross-section of the i^{th} tape.

J. Muzet, C. Trophime, X. Chaud
C. PrudHomme, V. Chabannes (IRMA, Strasbourg)

The Nougat HTS insert is operated in a resistive background magnetic field $\mathbf{B_{bg}}$. To estimate the dependence of I_c versus $\mathbf{B_{bg}}$ generated by resistive magnets, a self-consistent python algorithm was implemented following [Zermeño *et al.*, Supercond. Sci. Technol. **28** 085004 (2015)] using the *Feel++ CFPDES* toolbox. This algorithm is an iterative procedure computing J in the tapes for different imposed current until I_c is reached. Several stopping criterions are described in the article, and we used the most conservative one - the MAX criteria - to determine I_c. Here I_c is defined as the current at which E reaches its critical value E_c in at least one tape of the HTS insert.

The model is applied to the Nougat insert composed of 9 double-pancakes of 290 turns each in the 170 mm configuration of helices and bitter coils in an axisymmetric geometry. It was computed for different values of $\mathbf{B_{bg}}$, with a $J_c(B,\theta,T)$ fit function derived from the technical report of the CERN for SuperPower® superconducting tapes.

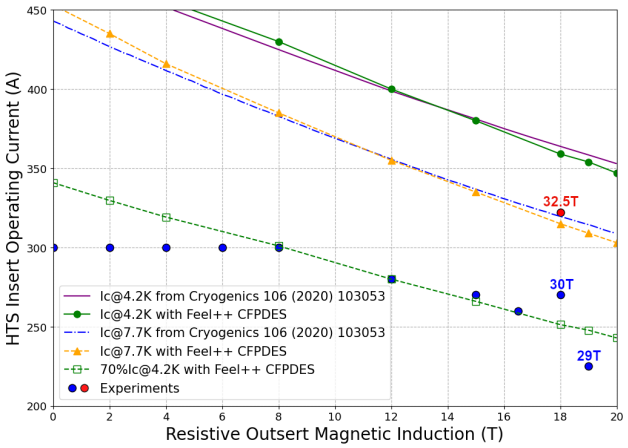

FIG. 119. *HTS Nougat insert current versus external resistive outsert magnetic induction* $\boldsymbol{B_{bg}}$.

The results are shown in the figure119. The red and blue closed circles are the measured Nougat critical currents described in [Fazilleau *et al.*, Cryogenics **106**, 103053 (2020)], while the lines show the computed values of I_c. The green plain line and the yellow dashed line represent respectively the critical current of the HTS insert Nougat at 4.2 K and 7.7 K obtained with *Feel++ CFPDES*.

Our results are compared with the measured I_c at 4.2 K, shown as a purple plain line. A small (0.95%) relative error is observed between the two estimates confirming the validity of our results.

Pulsed magnets and generators

In parallel to the production of standard 60 and 70 T magnets we continue developments of our multi-coil systems. The new insert for the 90 T dual-coil magnet wound at the end of 2022, combining for the first time copper-niobium and copper-stainless steel composite conductors, has been tested. The objective was to use as little Cu-Nb as possible in the context of the war in Ukraine, as this conductor is produced by a Russian company, and can no longer be purchased. The coil generated 92 T successfully before its failure. This result validates the design, using for the first three layers Cu-Nb, which generally makes up the entire coil, and the in-house copper-stainless steel composite wire, for the rest of the coil. This design will be generalized, and a second 90 T insert has been produced with a stronger wire, with 60% of stainless steel instead of 40%, and is now available for our users. A spare, and a large bore version, are under preparation. This third coil is required to generate an 80 T background field for the 120 T non-destructive pulsed magnet project.

FIG. 120. *Photo of the 1 MΩ resistors, the blue cylinders, installed on the capacitors for the automatic discharge. The fuses are the small vertical tubes above the resistors.*

We have equipped all the capacitors of the 21 MJ generator with 1 MΩ resistors, visible in figure 120. They are placed in parallel with each fuse during the dump process at the end of each charge. Their purpose is to automatically discharge a capacitor in about half an hour if its corresponding fuse is not functional for any reason. Thanks to this modification, it is no longer necessary to enter the room to manually discharge a capacitor to prevent degradation.

The refurbishment of the 1.15 MJ mobile capacitor bank is nearly finished. This generator, used at the ESRF and ILL, is composed of three modules, two boxes containing the capacitors, a crowbar circuit and protecting inductors, and a central module containing the charger, the thyristor stack and the automation. The replacement of the obsolete automation is completed. In January 2024 we will adapt the two capacitors boxes to the new central module, before the next experiments at the ESRF scheduled mid 2024.

In the context of high magnetic fields, an essential parameter to check after the pulse is the current that has been generated. The current generally between 10 and 20 kA is obtained by measuring the voltage across a shunt resistor placed in the circuit. The voltage to be measured is generally ≤ 10 V. However measuring this is complicated by the very high common mode voltage (up to 2000 V) which is unavoidable since the generators are situated far from the shunt resistors. Therefore, measuring the shunt voltage requires expensive instruments.

To solve this problem, we have developed an in-house electronic card, combined with an Arduino plus an ethernet shield. A differential amplifier coupled to an analog-to-digital converter, are the heart of the instrument. An optical impulsion triggers the acquisition, the digitized signal is then transmitted to the Arduino and sent to the programmable logic controller (PLC) by the ethernet shield using the very versatile MODBUS TCP protocol. A temperature probe is also measured, to correct the value of the shunt resistance as a function of the temperature. This provides a more accurate measurement of the current.

When used with our fast generators, for example the rapid 115 kJ generator for the 120 T project), which deliver ≥ 100 kA in $\simeq 100\,\mu$s, a shunt resistor is not suitable. Instead, an optional analog integrator is used to treat the signal from a pickup coil.

In our first tests, the difference between the current measured with the expensive (> 10 k€) Hioki usually used, and the in-house electronic card is less than 0,5% with a shunt resistor, and less than 1% with a pickup coil. This development is validated and will be duplicated in all our capacitor banks, including the mobile generators.

FIG. 121. *Photo of the in-house electronic card, placed on an Arduino with an ethernet shield, developed to acquire and transmit to the PLC the current of each capacitor bank.*

J. Béard, J. Billette, J-M. Lagarrigue, T. Lemaire, T. Moraine, J-P. Nicolin, E. Noël

Resistivity and tensile strength of silver-copper composite wires

We have investigated 1 vol. % Ag-Cu composite wires with a Cu matrix showing a bimodal grain-size distribution in order to obtain the best compromise between high strength and low resistivity. A schematic representation of the method and the expected microstructures of the samples is presented in figure 122.

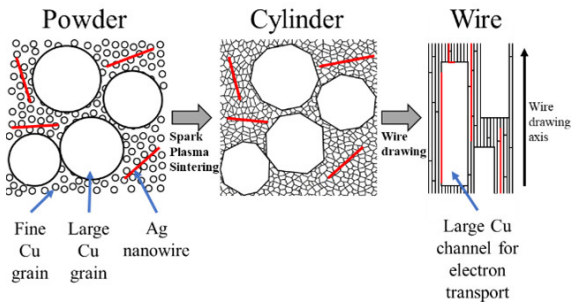

FIG. 122. *Schematic showing the method and the expected microstructure of the powder, cylinder and wire samples.*

Combining powder metallurgy, SPS sintering and wire drawing, it is possible to prepare 1 vol. % Ag-Cu composite wires with a Cu matrix showing a bimodal grain-size distribution. A fine Cu powder ($\phi \simeq 1\mu$m) and a coarse Cu powder ($\phi \simeq 20\mu$m) are mixed with a weight mixing ratio ($Cu_{1\mu m}/Cu_{20\mu m}$) 50/50 and 75/25. Composite powders are prepared by mixing of 1 vol. % Ag nanowires and bimodal Cu powder. They are consolidated into cylinders (8 mm in diameter and 30 mm long) by Spark Plasma Sintering (SPS) at 450 °C. The cylinders served as starting materials for room temperature wire-drawing for the preparation of fine wires ($1 - 0.2$ mm diameter). The bimodal character of Cu is preserved after all the preparation steps.

The wires are composed of Ag nanowires distributed at the boundaries of fine Cu grains whose size is close to that of a dislocation cell (0.2μm) and large and long micrometric Cu grains (indicated by an arrow in figure 123). Because they form large areas with few grain boundaries micrometric Cu grains can be considered as fast channels for electron transport. At 77 K, the resistivity of 0.2 mm wires is $0.51\mu\Omega$.cm for W_{100}, $0.45\mu\Omega$.cm for $W_{75/25}$, $0.40\mu\Omega$.cm for $W_{50/50}$. The presence of the larger Cu grains greatly reduce the electrical resistivity while having a moderate effect on the ultimate tensile strength (UTS). At 77 K, UTS value is 1138 MPa for W_{100}, 1082 MPa for $W_{75/25}$ and 954 MPa for $W_{50/50}$. The $W_{75/25}$ wires offer the best combination of high tensile strength and low electrical resistivity.

It is therefore possible to improve the low resistivity and high mechanical strength compromise by a simple modification of the initial composite powder. In addition, it is possible to adapt, if necessary, the properties of prepared wires by modifying the initial proportion of fine and coarse Cu grains. These results could provide important guidelines for the design and preparation of ultra-strong yet electrically conducting macroscopic wires. For more details please see [Tardieu *et al.*, Materials Today Communications (2023)].

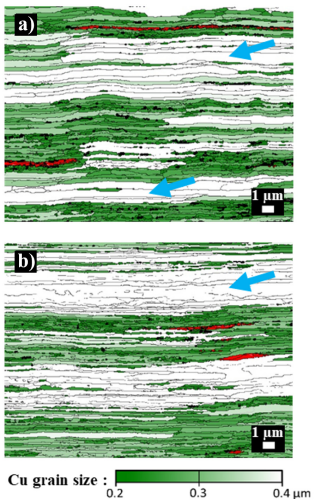

FIG. 123. *Grain size distribution maps of the longitudinal section of $W_{50/50}$ (a) and $W_{75/25}$ (b) wires ($\phi = 0.5$ mm). Color code, Ag: red. Cu: shades of green depending on the grain size (grains colored in white are larger than 0.4μm).*

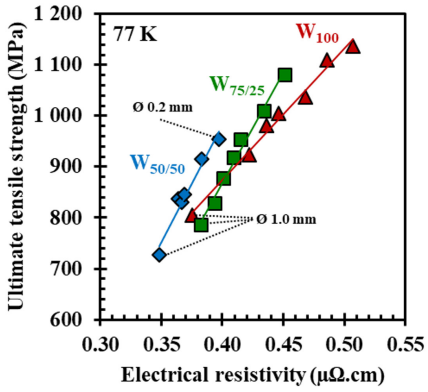

FIG. 124. *UTS versus electrical resistivity at 77 K for various wires. The dotted lines indicate wires with a diameter of 1 mm and the 0.2 mm wire for $W_{50/50}$.*

S. Tardieu, N. Ferreira, F. Lecouturier-Dupouy
D. Mesguich, A. Lonjon, C. Laurent (CIRIMAT, CNRS-UPS-INP, Toulouse), G. Chevallier, C. Estournès (Plateforme Nationale CNRS de Frittage Flash, Toulouse) A. Proietti (Centre de Microcaractérisation Raimond Castaing, Toulouse)

Scale-up of silver-copper composite wires for use in a 100T triple coil

The generation of non-destructive pulsed magnetic fields of 100 T involves high mechanical stress, due to the Lorentz forces, which few conductors can resist. Currently, the inner coil (the most mechanically stressed) of the 100 T triple coil consists of a winding of a copper-niobium (Cu-Nb) wire produced by Rusatom Metal Tech. Currently, it is one of the strongest mechanically conductors commercially available. However, in order to avoid dependence on such conductors, which can only be produced by a single manufacturer, we are working on solutions to limit their use or to replace them by new innovative conductors.

The first solution is to limit the quantity of Cu-Nb wire necessary for the manufacture of the inner coil. In order to achieve this, a new design is developed. This new design requires only about 200 g of Cu-Nb wire (current design requires 10 kg of Cu-Nb conductor), the rest of the coil being made up with macro-composite copper-stainless steel (Cu-SS) with a volumic fraction of 40 % of SS (1258 MPa; 0.41$\mu\Omega$.cm at 77 K) manufactured in-house and already used in the middle coil. Cu-Nb make up the first three layers of the coil then the other layers are wound with a Cu-SS wire. A brass junction allows the connection between the conductors.

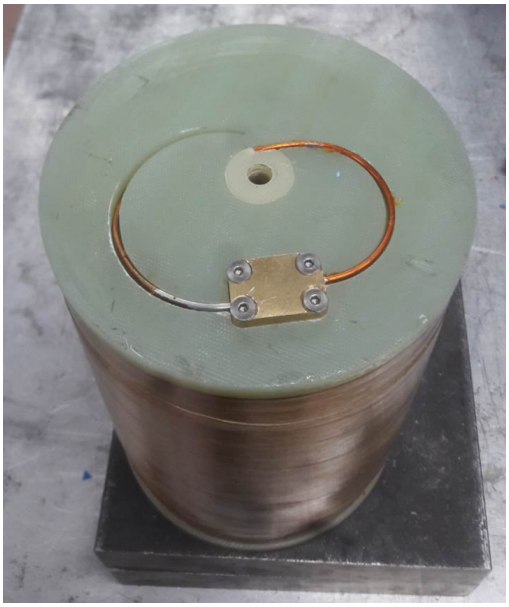

FIG. 125. *The first bi-material inner coil prototype showing the output of the 3rd layer of Cu-Nb (right) connected by a brass junction to the entry of the 1st layer of Cu-SS (left).*

This coil has been tested in a dual coil system and made it possible to generate several tens of magnetic fields pulses of 90 T. After integration in the triple coil system a maximum magnetic field of 92 T has been produced and the failure was due to the weakness of the Cu-SS wire and not to the junction between wires. Generating a higher magnetic field requires the use of a Cu-SS conductor with a higher ultimate tensile strength (UTS). Very high strength Cu-SS with a volumic fraction of 60 % of SS (6.0 mm^2; 1406 MPa; 0.61$\mu\Omega$.cm at 77 K) was therefore produced. These tests validate the design of a bi-material inner coil connected using a brass junction.

The second solution is to completely replace the Cu-Nb conductor by Ag-Cu composite wires. However, until then, the volume of the composite Ag-Cu wires produced (14 g) by this method was too small to consider their use in magnets. This is why we are involved in scaling-up the production of these samples. The main risk is that the macroscopic properties will be modified during the upscale and do not longer fit the initial specifications. The scaled-up Ag-Cu wires (140 g) show a UTS ranging from 853 to 1169 MPa and the electrical resistivity ranging from 0.46 to 0.51$\mu\Omega$.cm at 77 K. The properties of the wires are not impacted by the upscale, making such a composite wire a very good candidate to replace the Cu-Nb wire in the inner coil. In addition, it is possible to increase the silver content in order to achieve higher UTS values. We are now on the way to double the volume of the Ag-Cu cylinder produced (about 280 g) in order to wind a first prototype of magnet with these Ag-Cu composite wires.

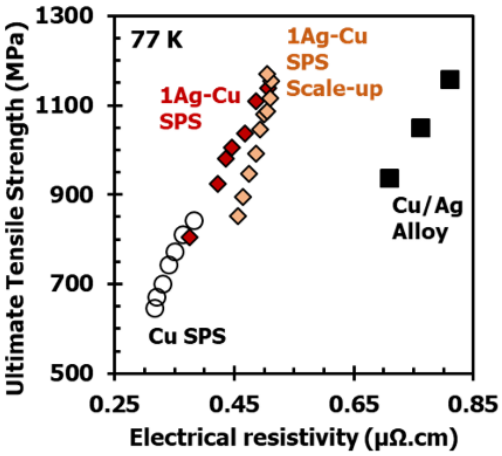

FIG. 126. *Ultimate tensile strength versus electrical resistivity at 77 K for Cu SPS, 1Ag-Cu and scaled-up 1Ag-Cu composite wires by SPS, Cu/Ag alloyed wires* 21 – 25 *vol. % Ag.*

S. Tardieu, J. Béard, N. Ferreira, F. Teyssier, T. Schiavo, F. Lecouturier-Dupouy
D. Mesguich, A. Lonjon, C. Laurent (CIRIMAT, CNRS-UPS-INP, Toulouse), G. Chevallier, C. Estournès (Plateforme Nationale CNRS de Frittage Flash, Toulouse)

PhD theses 2023

1. Nouâmane Cherkaoui
   Synthesis and study of chiral Prussian blue analogs and possible quantum spin liquids
   Doctorat de l'Université Grenoble-Alpes
   Thése soutenue le 6 février 2023

2. Vincent Oliviero
   Surface de Fermi et ordres électroniques dans les supraconducteurs non-conventionnels
   Doctorat de l'Université de Toulouse
   Thése soutenue le 27 mars 2023

3. Shuli Wang
   Investigation of the electronic properties of two-dimensional metal halide perovskites via magneto-optical spectroscopy
   Doctorat de l'Université de Toulouse: Délivré par l'Institut National des Sciences Appliquées de Toulouse
   Thése soutenue le 15 mai 2023

4. Jonathan Agil
   Biréfringence magnétique du vide : un test optique de l'électrodynamique quantique
   Doctorat de l'Université de Toulouse
   Thése soutenue le 31 août 2023

5. Himanshu
   Determination of the nuclear and magnetic structure of manganese oxide epitaxial thin films: an X-ray and neutron diffraction study
   Doctorat de l'Université Grenoble Alpes
   Thèse soutenue le 29 novembre 2023

6. Ivan Mohelsky
   Magneto-optical investigations of topological materials
   Doctorat de l'Université Grenoble Alpes
   Thèse soutenue le 30 novembre 2023

7. Nathan Aubergier
   Physics of the valley splitting in silicon MOSFETs : Untangling a multi-factorial dependency
   Doctorat de l'Université Grenoble Alpes
   Thèse soutenue le 13 décembre 2023

8. Rami Nasser-Din
   Nuclear magnetic resonance studies of paramagnetic relaxation enhancement at high magnetic fields: methods and applications
   Doctorat de l'Université Grenoble Alpes
   Thèse soutenue le 14 décembre 2023

9. Simon Rousseau
   Anomalous transport properties of the skyrmion compound EuPtSi
   Doctorat de l'Université Grenoble Alpes
   Thèse soutenue le 19 décembre 2023

List of Publications 2023

[1] Jonathan Agil, Rémy Battesti, and Carlo Rizzo, "On the speed of light in a vacuum in the presence of a magnetic field," The European Physical Journal H **48**, 2 (2023).

[2] J. Agil, R. Battesti, C. Rizzo, and D. Bakalov, "On the positronium g-factor," The European Physical Journal D **77**, 196 (2023).

[3] Jonathan Agil, Bruno Letourneur, Sylvie George, Rémy Battesti, and Carlo Rizzo, "Characterisation of the waveplate associated to layers in interferential mirrors," Eur. Phys. J. Appl. Phys. **98**, 61 (2023).

[4] Dai Aoki, Ilya Sheikin, Alix McCollam, Jun Ishizuka, Youichi Yanase, Gerard Lapertot, Jacques Flouquet, and Georg Knebel, "de Haas-van Alphen Oscillations for the Field Along c-axis in UTe_2," Journal of the Physical Society of Japan **92**, 065002 (2023).

[5] Vladimir B Arion, Oleg Palamarciuc, Sergiu Shova, Ghenadie Novitchi, and Peter Rapta, "Iron (III) complexes with ditopic macrocycles bearing crown-ether and bis (salicylidene) isothiosemicarbazide moieties," Journal of the Serbian Chemical Society **88**, 1205 (2023).

[6] Danis I. Badrtdinov, Carlos Rodriguez-Fernandez, Magdalena Grzeszczyk, Zhizhan Qiu, Kristina Vaklinova, Pengru Huang, Alexander Hampel, Kenji Watanabe, Takashi Taniguchi, Lu Jiong, Marek Potemski, Cyrus E. Dreyer, Maciej Koperski, and Malte Rösner, "Dielectric Environment Sensitivity of Carbon Centers in Hexagonal Boron Nitride," Small **19**, 2300144 (2023).

[7] G Bovone, F Buta, F Lonardo, T Bagni, M Bonura, D LeBoeuf, S C Hopkins, T Boutboul, A Ballarino, and C Senatore, "Effects of the oxygen source configuration on the superconducting properties of internally-oxidized internal-Sn Nb_3Sn wires," Superconductor Science and Technology **36**, 095018 (2023).

[8] Fan Bu, Yiyuan Zhang, Haoxiang Liu, Jun Wang, Eric Beaugnon, Jinshan Li, and Yixuan He, "Magnetic field intensity dependent microstructure evolution and recrystallization behavior in a Co-B eutectic alloy," Journal of Materials Science & Technology **138**, 93–107 (2023).

[9] Bruno Cury Camargo, Banan El-Kerdi, Andrei Alaferdov, Shahar Zuri, Magdalena Birowska, and Walter Escoffier, "Self-doped graphite nanobelts," Carbon **207**, 240–244 (2023).

[10] Ramakanta Chapai, Maxime Leroux, Vincent Oliviero, David Vignolles, Nicolas Bruyant, M. P. Smylie, D. Y. Chung, M. G. Kanatzidis, W.-K. Kwok, J. F. Mitchell, and Ulrich Welp, "Magnetic Breakdown and Topology in the Kagome Superconductor CsV_3Sb_5 under High Magnetic Field," Physical Review Letters **130**, 126401 (2023).

[11] Sophia Chen, Nick Hauser, James Hester, Jonah Kanner, Kati Lassila-Perini, Andrea Lausi, Charles Simon, and Jon Taylor, "Opportunities and challenges in data sharing at multi-user facilities," Nature Reviews Physics **5**, 83–86 (2023).

[12] C. W. Cho, A. Pawbake, N. Aubergier, A. L. Barra, K. Mosina, Z. Sofer, M. E. Zhitomirsky, C. Faugeras, and B. A. Piot, "Microscopic parameters of the van der Waals CrSBr antiferromagnet from microwave absorption experiments," Physical Review B **107**, 094403 (2023).

[13] Nicolas Combe, Renaud Mathevet, Patrice Marchou, Charlotte Fabre, and Nabil Lamrani, "Études quantitatives des accélérations d'inertie avec un smartphone. Partie 1: accélération de Coriolis." Le Bulletin de l'Union des Professeurs de Physique et de Chimie **117**, 51 (2023).

[14] Nicolas Combe, Renaud Mathevet, Patrice Marchou, Charlotte Fabre, and Nabil Lamrani, "Études quantitatives des accélérations d'inertie avec un smartphone Partie 2 : accélération d'entraînement," Le Bulletin de l'Union des Professeurs de Physique et de Chimie **117**, 173 (2023).

[15] Nathan D. Cottam, Jonathan S. Austin, Chengxi Zhang, Amalia Patanè, Walter Escoffier, Michel Goiran, Mathieu Pierre, Camilla Coletti, Vaidotas Miseikis, Lyudmila Turyanska, and Oleg Makarovsky, "Magnetic and Electric Field Dependent Charge Transfer in Perovskite/Graphene Field Effect Transistors," Advanced Electronic Materials **9**, 2200995 (2023).

[16] Olesea Cuzan, Sergiu Shova, Ghenadie Novitchi, and Vasile Lozan, "Synthesis, characterization and magnetochemical study of cobalt, nickel and manganese coordination polymers," Inorganica Chimica Acta **553**, 121526 (2023).

[17] Kais Dhbaibi, Maxime Grasser, Haiet Douib, Vincent Dorcet, Olivier Cador, Nicolas Vanthuyne, François Riobé, Olivier Maury, Stèphan Guy, Amina Bensalah-Ledoux, Bruno Baguenard, Geert L. J. A. Rikken, Cyrille Train, Boris Le Guennic, Matteo Atzori, Fabrice Pointillart, and Jeanne Crassous, "Multifunctional Helicene-Based Ytterbium Coordination Polymer Displaying Circularly Polarized Luminescence, Slow Magnetic Relaxation and Room Temperature Magneto-Chiral Dichroism," Angewandte Chemie International Edition **62**, e202215558 (2023).

[18] Manuel Donaire, Nicolas Bruyant, and Geert L. J. A. Rikken, "Traveling Wave Enantioselective Electron Paramagnetic Resonance," J. Phys. Chem. Lett. **14**, 4504–4509 (2023).

[19] Gautier Duroux, Lucas Robin, Peizhao Liu, Emilie Dols, Matheus De Souza Lima Mendes, Sonia Buffière, Elodie Pardieu, Antoine Scalabre, Thierry Buffeteau, Sylvain Nlate, Reiko Oda, Maria Sara Raju, Matteo Atzori, Cyrille Train, Geert L. J. A. Rikken, Patrick Rosa, Elizabeth A. Hillard, and Emilie Pouget, "Induced circular dichroism from helicoidal nano substrates to porphyrins: the role of chiral self-assembly," Nanoscale **15**, 12095–12104 (2023).

[20] Mateusz Dyksik, Dorian Beret, Michal Baranowski, Herman Duim, Sébastien Moyano, Katarzyna Posmyk, Adnen Mlayah, Sampson Adjokatse, Duncan K. Maude, Maria Antonietta Loi, Pascal Puech, and Paulina Plochocka, "Polaron Vibronic Progression Shapes the Optical Response of 2D Perovskites," Advanced Science **2**, 2305182 (2023).

[21] Eduard Galstyan, Janakiram Kadiyala, Mahesh Paidpilli, Chirag Goel, Jithin Sai Sandra, Vamsi Yerraguravagari, Goran Majkic, Rohit Jain, Siwei Chen, Yi Li, Robert Schmidt, Jan Jaroszynski, Griffin Bradford, Dmytro Abraimov, Xavier Chaud, Jungbin Song, and Venkat Selvamanickam, "High critical current STAR wires with REBCO tapes by advanced MOCVD," Superconductor Science and Technology **36**, 055007 (2023).

[22] S. Gebert, C. Consejo, S. S. Krishtopenko, S. Ruffenach, M. Szola, J. Torres, C. Bray, B. Jouault, M. Orlita, X. Baudry, P. Ballet, S. V. Morozov, V. I. Gavrilenko, N. N. Mikhailov, S. A. Dvoretskii, and F. Teppe, "Terahertz cyclotron emission from two-dimensional Dirac fermions," Nature Photonics **17**, 244–249 (2023).

[23] N. Gutierrez, J. Degallaix, D. Hofman, C. Michel, L. Pinard, J. Morville, R. Battesti, and G. Cagnoli, "Optical characterization of high performance mirrors based on cavity ringdown time measurements with 6 degrees of freedom mirror positioning," Review of Scientific Instruments **94**, 105113 (2023).

[24] A. Hötger, T. Amit, J. Klein, K. Barthelmi, T. Pelini, A. Delhomme, S. Rey, M. Potemski, C. Faugeras, G. Cohen, D. Hernangómez-Pérez, T. Taniguchi, K. Watanabe, C. Kastl, J. J. Finley, S. Refaely-Abramson, A. W. Holleitner, and A. V. Stier, "Spin-defect characteristics of single sulfur vacancies in monolayer MoS_2," npj 2D Materials and Applications **7**, 30 (2023).

[25] Teresa Insinna, Euan N. Bassey, Katharina Märker, Alberto Collauto, Anne-Laure Barra, and Clare P. Grey, "Graphite Anodes for Li-Ion Batteries: An Electron Paramagnetic Resonance Investigation," Chem. Mater. **35**, 5497–5511 (2023).

[26] Robert A. Jagt, Ivona Bravić, Lissa Eyre, Krzysztof Galkowski, Joanna Borowiec, Kavya Reddy Dudipala, Michal Baranowski, Mateusz Dyksik, Tim W. J. van de Goor, Theo Kreouzis, Ming Xiao, Adrian Bevan, Paulina Plochocka, Samuel D. Stranks, Felix Deschler, Bartomeu Monserrat, Judith L. MacManus-Driscoll, and Robert L. Z. Hoye, "Layered BiOI single crystals capable of detecting low dose rates of X-rays," Nature Communications **14**, 2452 (2023).

[27] Dipankar Jana, P. Kapuscinski, I. Mohelsky, D. Vaclavkova, I. Breslavetz, M. Orlita, C. Faugeras, and M. Potemski, "Magnon gap excitations and spin-entangled optical transition in the van der Waals antiferromagnet $NiPS_3$," Physical Review B **108**, 115149 (2023).

[28] Dipankar Jana, Piotr Kapuscinski, Amit Pawbake, Anastasios Papavasileiou, Zdenek Sofer, Ivan Breslavetz, Milan Orlita, Marek Potemski, and Clement Faugeras, "In-plane anisotropy in the van der Waals antiferromagnet $FePSe_3$ probed by magneto-Raman scattering," Physical Review B **108**, 144415 (2023).

[29] Jana Jurakova, Ondrej F. Fellner, Soren Schlittenhardt, Sarka Vavreckova, Ivan Nemec, Radovan Herchel, Erik Cizmar, Vinicius Tadeu Santana, Milan Orlita, Denis Gentili, Giampiero Ruani, Massimiliano Cavallini, Petr Neugebauer, Mario Ruben, and Ivan Salitros, "Neutral cobalt(ii)-bis(benzimidazole)pyridine field-induced single-ion magnets for surface deposition," Inorg. Chem. Front. **10**, 5406–5419 (2023).

[30] T. Klein, A. Demuer, G. Seyfarth, H. Cercellier, L. Doussoulin, P. Toulemonde, A.-A. Haghighirad, F. Hardy, and C. Marcenat, "High-sensitivity specific heat study of the low-temperature–high-field corner of the $H-T$ phase diagram of FeSe," Physical Review B **107**, 224506 (2023).

[31] F. Le Mardelé, J. Wyzula, I. Mohelsky, S. Nasrallah, M. Loh, S. Ben David, O. Toledano, D. Tolj, M. Novak, G. Eguchi, S. Paschen, N. Barišić, J. Chen, A. Kimura, M. Orlita, Z. Rukelj, Ana Akrap, and D. Santos-Cottin, "Evidence for three-dimensional Dirac conical bands in TlBiSSe by optical and magneto-optical spectroscopy," Physical Review B **107**, L241101 (2023).

[32] Nikoleta Malinová, Jana Jurakova, Barbora Brachnakova, Jana Dubnicka Midlikova, Erik Cizmar, Vinicius Tadeu Santana, Radovan Herchel, Milan Orlita, Ivan Mohelsky, Jan Moncol, Petr Neugebauer, and Ivan Salitros, "Magnetization Slow Dynamics in Mononuclear Co(II) Field-Induced Single-Molecule Magnet," Crystal Growth & Design **23**, 2430–2441 (2023).

[33] Renaud Mathevet, Simon Garrigou, Arnaud Le Houelleur, Emeryk Ablonet, Charlotte Fabre, Nabil Lamrani, Patrice Marchou, and Nicolas Combe, "Bifurcation fourche et ralentissement critique." Le Bulletin de l'Union des Professeurs de Physique et de Chimie **117**, 573 (2023).

[34] Renaud Mathevet, Nabil Lamrani, Charlotte Fabre, and Patrice Marchou, "Expériences quantitatives et symétries du champ magnétique," Le Bulletin de l'Union des Professeurs de Physique et de Chimie **117**, 783 (2023).

[35] I. Mohelsky, J. Wyzula, B. A. Piot, G. D. Gu, Q. Li, A. Akrap, and M. Orlita, "Temperature dependence of the energy band gap in $ZrTe_5$: Implications for the topological phase," Physical Review B **107**, L041202 (2023).

[36] Ciaran Mullan, Sergey Slizovskiy, Jun Yin, Ziwei Wang, Qian Yang, Shuigang Xu, Yaping Yang, Benjamin A. Piot, Sheng Hu, Takashi Taniguchi, Kenji Watanabe, Kostya S. Novoselov, A. K. Geim, Vladimir I. Fal'ko, and Artem Mishchenko, "Mixing of moiré-surface and bulk states in graphite," Nature **620**, 756–761 (2023).

[37] Alicia Negre, Renaud Mathevet, Benoit Chalopin, and Sébastien Massenot, "Unexpected optimal measurement protocols in Bell's inequality violation experiments," American Journal of Physics **91**, 64–73 (2023).

[38] Swaroop Kumar Palai, Mateusz Dyksik, Nikodem Sokolowski, Mariusz Ciorga, Estrella Sánchez Viso, Yong Xie, Alina Schubert, Takashi Taniguchi, Kenji Watanabe, Duncan K. Maude, Alessandro Surrente, Michal Baranowski, Andres Castellanos-Gomez, Carmen Munuera, and Paulina Plochocka, "Approaching the Intrinsic Properties of Moiré Structures Using Atomic Force Microscopy Ironing," Nano Letters **23**, 4749–4755 (2023).

[39] Amit Pawbake, Thomas Pelini, Ivan Mohelsky, Dipankar Jana, Ivan Breslavetz, Chang-Woo Cho, Milan Orlita, Marek Potemski, Marie-Aude Measson, Nathan P. Wilson, Kseniia Mosina, Aljoscha Soll, Zdenek Sofer, Benjamin A. Piot, Mike E. Zhitomirsky, and Clement Faugeras, "Magneto-Optical Sensing of the Pressure Driven Magnetic Ground States in Bulk CrSBr," Nano Letters **23**, 9587–9593 (2023).

[40] Amit Pawbake, Thomas Pelini, Nathan P. Wilson, Kseniia Mosina, Zdenek Sofer, Rolf Heid, and Clement Faugeras, "Raman scattering signatures of strong spin-phonon coupling in the bulk magnetic van der Waals material CrSBr," Physical Review B **107**, 075421 (2023).

[41] Amit Pawbake, Sachin Rondiya, Dattatray Late, Mohit Prasad, and Sandesh Jadkar, "Hot wire-CVD grown molybdenum disulfide (MoS_2) thin films for photodetector and humidity sensing applications," Journal of Materials Science: Materials in Electronics **34**, 1354 (2023).

[42] S. Polatkan, E. Uykur, I. Mohelsky, J. Wyzula, M. Orlita, C. Shekhar, C. Felser, M. Dressel, and A. V. Pronin, "Exchange gap in GdPtBi probed by magneto-optics," Physical Review B **108**, L201201 (2023).
[43] S. Polatkan, E. Uykur, J. Wyzula, M. Orlita, C. Shekhar, C. Felser, M. Dressel, and A. V. Pronin, "Magneto-optical response of the Weyl semimetal NbAs: Experimental results and hyperbolic-band computations," Physical Review B **108**, L241201 (2023).
[44] Karolina Ewa Polczynska, Simon Le Denmat, Takashi Taniguchi, Kenji Watanabe, Marek Potemski, Piotr Kossacki, Wojciech Pacuski, and Jacek Kasprzak, "Coherent imaging and dynamics of excitons in $MoSe_2$ monolayers epitaxially grown on hexagonal boron nitride," Nanoscale **15**, 6941–6946 (2023).
[45] Oliver Portugall, "Étonnante physique," (CNRS Édition, 2023) Chap. Les champs magnétiques dialoguent avec la matière, editor Séverine Martrenchard, Edition: EAN13: 9782271148902.
[46] Katarzyna Posmyk, Mateusz Dyksik, Alessandro Surrente, Duncan K. Maude, Natalia Zawadzka, Adam Babinski, Maciej R. Molas, Watcharaphol Paritmongkol, Miroslaw Maczka, William A. Tisdale, Paulina Plochocka, and Michal Baranowski, "Exciton Fine Structure in 2D Perovskites: The Out-of-Plane Excitonic State," Advanced Optical Materials , 2300877 (2023).
[47] Katarzyna Posmyk, Mateusz Dyksik, Alessandro Surrente, Katarzyna Zalewska, Maciej Smiertka, Ewelina Cybula, Watcharaphol Paritmongkol, William A. Tisdale, Paulina Plochocka, and Michal Baranowski, "Fine Structure Splitting of Phonon-Assisted Excitonic Transition in $(PEA)_2PbI_4$ Two-Dimensional Perovskites," Nanomaterials **13**, 1119 (2023).
[48] P. Pugnat, R. Barbier, C. Berriaud, F. Debray, C. Grandclément, B. Hervieu, S. Krämer, Y. Krupko, F. Molinié, M. Pelloux, R. Pfister, L. Ronayette, and H. J. Schneider-Muntau, "Commissioning Tests of the 43+T Grenoble Hybrid Magnet," IEEE Transactions on Applied Superconductivity **34**, 1–5 (2023).
[49] Maria Sara Raju, Kais Dhbaibi, Maxime Grasser, Vincent Dorcet, Ivan Breslavetz, Kévin Paillot, Nicolas Vanthuyne, Olivier Cador, Geert L. J. A. Rikken, Boris Le Guennic, Jeanne Crassous, Fabrice Pointillart, Cyrille Train, and Matteo Atzori, "Magneto-Chiral Dichroism in a One-Dimensional Assembly of Helical Dysprosium(III) Single-Molecule Magnets," Inorg. Chem. **62**, 17583–17587 (2023).
[50] G. L. J. A. Rikken and N. Avarvari, "Comparing Electrical Magnetochiral Anisotropy and Chirality-Induced Spin Selectivity," J. Phys. Chem. Lett. **14**, 9727–9731 (2023).
[51] Aleksander Rodek, Thilo Hahn, James Howarth, Takashi Taniguchi, Kenji Watanabe, Marek Potemski, Piotr Kossacki, Daniel Wigger, and Jacek Kasprzak, "Controlled coherent-coupling and dynamics of exciton complexes in a $MoSe_2$ monolayer," 2D Materials **10**, 025027 (2023).
[52] A. Rosuel, C. Marcenat, G. Knebel, T. Klein, A. Pourret, N. Marquardt, Q. Niu, S. Rousseau, A. Demuer, G. Seyfarth, G. Lapertot, D. Aoki, D. Braithwaite, J. Flouquet, and J. P. Brison, "Field-Induced Tuning of the Pairing State in a Superconductor," Physical Review X **13**, 011022 (2023).
[53] D. Santos-Cottin, I. Mohelský, J. Wyzula, F. Le Mardelé, I. Kapon, S. Nasrallah, N. Barišić, I. Živković, J. R. Soh, F. Guo, K. Rigaux, M. Puppin, J. H. Dil, B. Gudac, Z. Rukelj, M. Novak, A. B. Kuzmenko, C. C. Homes, Tomasz Dietl, M. Orlita, and Ana Akrap, "$EuCd_2As_2$: A Magnetic Semiconductor," Physical Review Letters **131**, 186704 (2023).
[54] Mykhailo Shestopalov, Václav Dědič, Martin Rejhon, Bohdan Morzhuk, Jan Kunc, Vaisakh C. Paingad, Petr Kužel, Ivan Mohelský, Florian Le Mardelé, and Milan Orlita, "Plasmon-plasmon interaction and the role of buffer in epitaxial graphene microflakes," Physical Review B **108**, 045308 (2023).
[55] Nikodem Sokolowski, Swaroop Palai, Mateusz Dyksik, Katarzyna Posmyk, Michal Baranowski, Alessandro Surrente, Duncan Maude, Felix Carrascoso, Onur Cakiroglu, Estrella Sanchez, Alina Schubert, Carmen Munuera, Takashi Taniguchi, Kenji Watanabe, Joakim Hagel, Samuel Brem, Andres Castellanos-Gomez, Ermin Malic, and Paulina Plochocka, "Twist-angle dependent dehybridization of momentum-indirect excitons in $MoSe_2/MoS_2$ heterostructures," 2D Materials **10**, 034003 (2023).
[56] Wiktoria Solarska, Krzysztof Karpierz, Maciej Zaremba, Florian Le Mardelé, Ivan Mohelsky, Adam Siemaszko, Mikolaj Grymuza, Lucja Kipczak, Natalia Zawadzka, Maciej R. Molas, Eryk Imos, Zbigniew Adamus, Tomasz Slupinski, Tomasz Wojtowicz, Milan Orlita, Adam Babinski, and Jerzy Lusakowski, "Magnetophotoluminescence of Modulation-Doped CdTe Multiple Quantum Wells," ACS Omega **8**, 40801–40807 (2023).
[57] Alexandru-Constantin Stoica, Madalin Damoc, Sergiu Shova, Ghenadie Novitchi, Mihaela Dascalu, and Maria Cazacu, "A Manganese(II) 3D Metal-Organic Framework with Siloxane-Spaced Dicarboxylic Ligand: Synthesis, Structure, and Properties," Inorganics **11**, 21 (2023).
[58] Simon Tardieu, David Mesguich, Antoine Lonjon, Florence Lecouturier-Dupouy, Nelson Ferreira, Geoffroy Chevallier, Arnaud Proietti, Claude Estournès, and Christophe Laurent, "Influence of bimodal copper grain size distribution on electrical resistivity and tensile strength of silver - copper composite wires," Materials Today Communications , 107403 (2023).
[59] Kristupas Kazimieras Tikuišis, Adam Dubroka, Klára Uhlířová, Florian Speck, Thomas Seyller, Maria Losurdo, Milan Orlita, and Martin Veis, "Dielectric function of epitaxial quasi-freestanding monolayer graphene on Si-face 6H-SiC in a broad spectral range," Phys. Rev. Mater. **7**, 044201 (2023).
[60] Y. Tokunaga, H. Sakai, S. Kambe, P. Opletal, Y. Tokiwa, Y. Haga, S. Kitagawa, K. Ishida, D. Aoki, G. Knebel, G. Lapertot, S. Krämer, and M. Horvatić, "Longitudinal Spin Fluctuations Driving Field-Reinforced Superconductivity in UTe_2," Physical Review Letters **131**, 226503 (2023).
[61] Robert F. Tournier and Michael I. Ojovan, "$NiTi_2$, a New Liquid Glass," Materials **16**, 6681 (2023).
[62] Chen Wei, Jinshan Li, Bowen Dong, Chenglin Huang, Lin Wang, Yujie Yan, Yixuan He, Eric Beaugnon, and Jun Wang, "Tailoring the microstructure and properties of a Cu-Co immiscible alloy by high magnetic field assisted heat treatment," Materials Chemistry and Physics **302**, 127706 (2023).
[63] Chen Wei, Jun Wang, Bowen Dong, Yujie Yan, Lin Wang, Yixuan He, Eric Beaugnon, and Jinshan Li, "Properties and microstructural evolution of a ternary Cu-Co-Fe immiscible alloy solidified under high magnetic fields," Journal of Materials Research and Technology **24**, 3564–3574 (2023).

[64] Chen Wei, Jun Wang, Yixuan He, Yujie Yan, Eric Beaugnon, and Jinshan Li, "Magnetic field induced instability pattern evolution in an immiscible alloy," Applied Physics Letters **123**, 254101 (2023).

[65] Ruth Weller, Mihail Atanasov, Serhiy Demeshko, Ting-Yi Chen, Ivan Mohelsky, Eckhard Bill, Milan Orlita, Franc Meyer, Frank Neese, and C. Gunnar Werncke, "On the Single-Molecule Magnetic Behavior of Linear Iron(I) Arylsilylamides," Inorg. Chem. **62**, 3153–3161 (2023).

[66] Zhuo Yang, Benoit Fauqué, Toshihiro Nomura, Takashi Shitaokoshi, Sunghoon Kim, Debanjan Chowdhury, Zuzana Pribulová, Jozef Kacmarcik, Alexandre Pourret, Georg Knebel, Dai Aoki, Thierry Klein, Duncan K. Maude, Christophe Marcenat, and Yoshimitsu Kohama, "Unveiling the double-peak structure of quantum oscillations in the specific heat," Nature Communications **14**, 7006 (2023).

[67] W. Yao, A. Fazzini, S.N. Chen, K. Burdonov, J. Béard, M. Borghesi, A. Ciardi, M. Miceli, S. Orlando, X. Ribeyre, and et al., "Investigating particle acceleration dynamics in interpenetrating magnetized collisionless super-critical shocks," Journal of Plasma Physics **89**, 915890101 (2023).

[68] W. Yao, A. Higginson, J.-R Marquès, P. Antici, J. Béard, K. Burdonov, M. Borghesi, A. Castan, A. Ciardi, B. Coleman, S. N. Chen, E. d'Humières, T. Gangolf, L. Gremillet, B. Khiar, L. Lancia, P. Loiseau, X. Ribeyre, A. Soloviev, M. Starodubtsev, Q. Wang, and J. Fuchs, "Dynamics of Nanosecond Laser Pulse Propagation and of Associated Instabilities in a Magnetized Underdense Plasma," Physical Review Letters **130**, 265101 (2023).

Collaborating External Laboratories

Austria
Technische Universität Wien: 45

Belgium
Hasselt University, Diepenbeek: 31,32

Canada
INRS-EMT, Varennes: 73
University of Sherbrooke,: 85

China
IAPCM, Beijing: 73
Northwestern Polytechnical University, Xi'an: 78
Shanghai Superconductor Technology: 65
Shanghai University: 15
Southern University of Science and Technology, Shenzhen: 48

Croatia
University of Zagreb: 45

Czech Republic
Charles University, Prague: 14
Department of Inorganic Chemistry, University of Chemistry and Technology, Prague: 22,24,25,26
FZU Institute of Physics, Prague: 53

Denmark
Technical University of Denmark, Lyngby: 18

France
CBMN-CNRS, Universitey of Bordeaux: 59
CEA-DAM-DIF, Arpajon: 73
CEA-Grenoble: 25,50
CEA, IRIG, Pheliqs, Grenoble: 26,41
CEA-Saclay, Gif-sur-Yvette: 93,94,95
CEMES-CNRS, Toulouse: 34
Centre de Microcaractérisation Raimond Castaing, Toulouse: 99
CIRIMAT, CNRS-UPS-INP, Toulouse: 99,100
Collège de France-CNRS, Paris: 41
DACM, IRFU, CEA, Gif sur Yvette: 66
ESRF, Grenoble: 53
G2Elab, INPG-UGA-CNRS, Grenoble: 91
ICMCB-CNRS, Bordeaux: 49,59
INAC, CEA Grenoble: 51,52
Institut Néel, CNRS, University Grenoble Alpes: 25,51,52,74
ISM-CNRS, University of Bordeaux: 59
L2C-CNRS, University of Montpellier: 37
LAAS-CNRS, Toulouse: 34
LPSC, CNRS, Univiversity Grenoble Alpes: 74
LULI-CNRS, CEA, UPMC, Palaiseau: 73
ONERA, Palaiseau: 73
Plateforme Nationale CNRS de Frittage Flash, Toulouse: 99,100
Recherche Translationnelle et Innovation en Médecine et Complexité (TIMC), CNRS-UGA-INP Grenoble: 77
Safran Electronics & Defense, Montluçon: 75
SIMAP, INPG, Grenoble: 79
Sorbonne Université, Paris): 73
University of Bordeaux: 73

Singapore
National University of Singapore: 48

Slovakia
Slovak Academy of Sciences, Košice: 41

South Korea
CAPP/IBS, KAIST, Daejeon: 74

Spain
Área de Química Inorgánica-CIESOL, Almería: 53
ICMM-CSIC, Madrid: 20,21

Sweden
Chalmers University of Technology, Gothenburg: 21

Switzerland
EPFL, Lausanne: 45
Fribourg University: 35,45
University of Geneva: 69

The Netherlands
HMFL, Nijmegen: 90
University of Groningen: 34
University of Twente, AE Enschede: 67

United Kingdom
Cavendish Laboratory, University of Cambridge: 31
Coventry University: 79
Department of Physics and Astronomy and National Graphene Institute, University of Manchester: 13
Fujikura, Chessington, Surrey: 64
PEPR, Imerial College London: 16
Queen's University Belfast: 73
University of Nottingham: 15
University of Strathclyde: 68
Yusuf Hamied Department of Chemistry, University of Cambridge: 16

USA
Argonne National Laboratory, Chicago: 47
Brookhaven National Laboratory, New York: 35
Cornell University, Ithaca: 41
Hofstra University, New York: 47
Massachusetts Institute of Technology, Cambridge: 18,33
NHMFL, Los Alamos: 48
Northwestern University, Chicago: 47
University of California San Diego: 73

Author Index
(Contributors of LNCMI to this annual report)

CONTINUOUS MAGNETIC FIELDS
LNCMI-G, CNRS
25 avenue des Martyrs, B.P. 166
38042 GRENOBLE cedex 9 - France
Tel : +33 (0)4 76 88 10 48

LNCMI

PULSED MAGNETIC FIELDS
LNCMI-T, CNRS
143 avenue de Rangueil
31400 TOULOUSE - France
Tel : +33 (0)5 62 17 28 60

direction@lncmi.cnrs.fr
https://www.lncmi.cnrs.fr

LNCMI is a founding member of EMFL

EMFL
European Magnetic Field Laboratory

Création : Alexandra GASPARINI, LNCMI
Photos : Eva BEZGOUSKO, LNCMI / Julien BILLETTE, LNCMI / Frédéric MALIGNE / Vincent MONCORGE / Pierre PUGNAT, LNCMI / EMFL